UNIVERSITY OF GENOA

DOCTORAL THESIS

Transport in fluid flows unveiled by Lagrangian structures

Author:
Francesco ENRILE

Supervisors:
Prof. Giovanni BESIO
Prof. Alessandro STOCCHINO

A thesis submitted in fulfillment of the requirements
for the degree of Doctor of Philosophy

Doctoral School in Civil, Chemical and
Environmental Engineering
Curriculum in Fluid Dynamics and Environmental Engineering

May 7, 2018

Supervisors:
Prof. Giovanni Besio - DICCA, University of Genoa
Prof. Alessandro Stocchino - DICCA, University of Genoa

External Reviewers:
Prof. Annalisa Griffa - CNR-ISMAR, Pozzuolo di Lerici, Italia
Prof. Michael R. Allshouse - Department of Mechanical and Industrial Engineering, Northeastern University, USA

Examination Committee:
Prof. Nicoletta tambroni - DICCA, University of Genoa
Prof. Ilaria Gnecco - DICCA, University of Genoa
Prof. Simone Camarri - DICI, University of Pisa
Prof. Carlo Camporeale - DIATI, Polytechnic of Turin

Ph.D. program in Civil, Chemical and Environmental Engineering
Curriculum in Fluid Dynamics and Environmental Engineering
Cycle XXIX

“I have one of two choices - stay in the post office and go crazy . . . or stay out here and play at writer and starve. I have decided to starve.”

Henry Charles Bukowski

Abstract

Transport in fluid flows unveiled by Lagrangian structures

by Francesco ENRILE

The interpretation of flows in steady systems is straightforward: streamlines and trajectories coincide. Unsteady flows are much more challenging. A natural framework is the Lagrangian one since it allows the study of the flow in terms of particle trajectories. Mixing, i.e. dispersion, plays a fundamental role from this point of view. A usual approach consists in the computation of Lagrangian statistics as absolute and relative dispersion. However, a better picture is obtained if flow inhomogeneity is taken into account. As a result, Lagrangian Coherent Structures (LCS) arise as centrepieces of particle advection. These structures are not to be seen as touchable barriers. Rather, as emerging features of the velocity field that shape trajectory patterns. The methods presented here make use of finite-time Lyapunov exponent (FTLE) fields and tensorlines of the Cauchy-Green tensor in order to locate LCS. LCS are separatrices that divide the domain into regions with different dynamical behaviours. They enable the detection of directions along which transport is likely to develop, ultimately characterizing mixing. Two different datasets are deeply investigated. Surface velocity fields of the Gulf of Trieste recorded by coastal radars and surface velocity fields of compound channels recorded in laboratory experiments. Usual Lagrangian statistics such as absolute and relative dispersion are computed for the former dataset. Besides, a careful comparison and a reliability assessment of such a dataset is carried out comparing the Eulerian velocities of the field with the Lagrangian velocities of real drifter deployed in the Gulf. LCS are then computed and it is shown that they provide the directions along which transport develops. The second dataset allows a detailed investigation of two particular types of structures: shear and shearless structures. They are together detected on the surface of compound channels. They mark the transition region from the main channel to the floodplain and approximately the axis of the main channel, respectively.

Contents

List of Figures

List of Tables

Dedicated to my Sister and my Parents

Chapter 1

Introduction

Fluid flows can be analysed adopting either an Eulerian or a Lagrangian description. The choice between these two frameworks relies on the focus of the analysis. The Eulerian description takes into consideration fixed locations in space whereas the Lagrangian one is based on the motion of fluid particles. In other words, the Lagrangian description aims to provide the quantities of interest along particle paths, i.e. trajectories. This privileged point of view is adopted in this work.

Lagrangian description of fluid flows is traditionally carried out evaluating Lagrangian statistics, such as absolute and relative dispersion. These statistics describe the overall dispersion properties of the flow. However, no special attention is dedicated to the several regions the flow field is made of and the ways these interact. Many Lagrangian measures are global, as the relative and the absolute dispersion. Sometimes there is the need to take into account the local effects of transport. Indeed, especially in coastal areas, the direction of transport is crucial: offshore or inshore transport can exhibit analogue statistics. However, the effects of currents having opposite directions are extremely different. As a result, local Lagrangian measures must be adopted such as Lyapunov exponents. Therefore, global quantities do not take into special consideration the inhomogeneity of the flow. Should one be interested in this aspect, a natural step forward would be to adopt an approach that highlights whether the domain can be partitioned or not. Such subdivision can clearly emerge from particle advection, mainly marking regions of attraction and repulsion. Indeed, different regions can interact, i.e. mix, differently. A useful approach in order to interpret transport in complex flows and pursue the objective of describing such inhomogeneity is the identification of coherent structures. The basic idea consists in the detection of structures that are locally the strongest repelling or attracting material lines. Such features are commonly called Lagrangian Coherent Structures (LCS) and divide the flow field into regions with different dynamical behaviours. These material lines are to be seen as emerging patterns of particle advection, which is the

result of the underlying velocity field. Indeed, velocity fields alone do not provide the necessary information on transport properties since it is the integrated view over a finite-time interval that determines the advection process. Therefore, velocity fields are only the input of the calculations. The core is made of particle trajectories, i.e. the integration of the velocity fields. Trajectories are solution of the following equation:

$$\frac{d\boldsymbol{x}}{dt} = \boldsymbol{v}\left(\boldsymbol{x}, t\right) \tag{1.1}$$

where $\boldsymbol{v}\left(\boldsymbol{x}, t\right)$ is the time-dependent velocity field. Provided that the velocity is smooth enough, one can always compute a unique trajectory through any initial condition. This perspective seems to corroborate the fact that the Lagrangian description of transport in a fluid can always be derived from the velocity. This idea prevailed until the fundamental work by Lorenz (1963). As a result, it is now well-known that sensitivity to initial conditions dooms our expectations. Provided that we integrate the particles for long enough, each trajectory is unique and cannot resemble its neighbours. The Lagrangian description of the fluid is therefore very complex and one would need to compute and analyse millions of trajectories to characterize all the possible behaviours present in the system. Dynamical systems theory could be fruitfully implemented in order to overcome such shortcomings. The objective is to find transport barriers and a geometric description of transport in the complexity of the trajectories. The dynamical systems approach provides a few coherent structures from which the general behaviour of particles can be deduced. Figure 1.1 shows the conceptual map followed in this Thesis and summarises the ideas here introduced. The path followed focuses on mixing, i.e. dispersion of passive tracers. Mixing is studied adopting a Lagrangian framework that leads to the well-known Lagrangian statistics (LaCasce, 2008). They disregard the privileged directions along which transport may develop, i.e. possible inhomogeneities in the flow. As a result, flow inhomogeneity must be highlighted with Lagrangian structures, as already mentioned. These structures serve the ultimate purpose of describing mixing by characterizing the flow in space and time.

This thesis investigates the properties of fluid flows by analysing experimental velocity fields adopting a Lagrangian perspective. Chapter 2 is devoted to a general introduction to coherent structures in fluid flows. This introductory chapter clarifies the reasons why Lagrangian Structures must be investigated in order to better understand fluid flows. Several examples taken from the scientific literature are shown and the basis for the detailed investigations of the following Chapters are therefore introduced. Chapter 3 describes the state-of-the-art techniques adopted to detect Lagrangian Coherent Structures in geophysical flows. In particular, all these techniques stem from dynamical system theory. Chapter 4 deals with the analysis of a dataset of surface velocity fields of the Gulf of Trieste, Italy, recorded by coastal radars. The dataset also includes trajectories of drifters deployed in the Gulf. These velocity fields are employed in order to carry out usual Lagrangian analyses based on absolute and

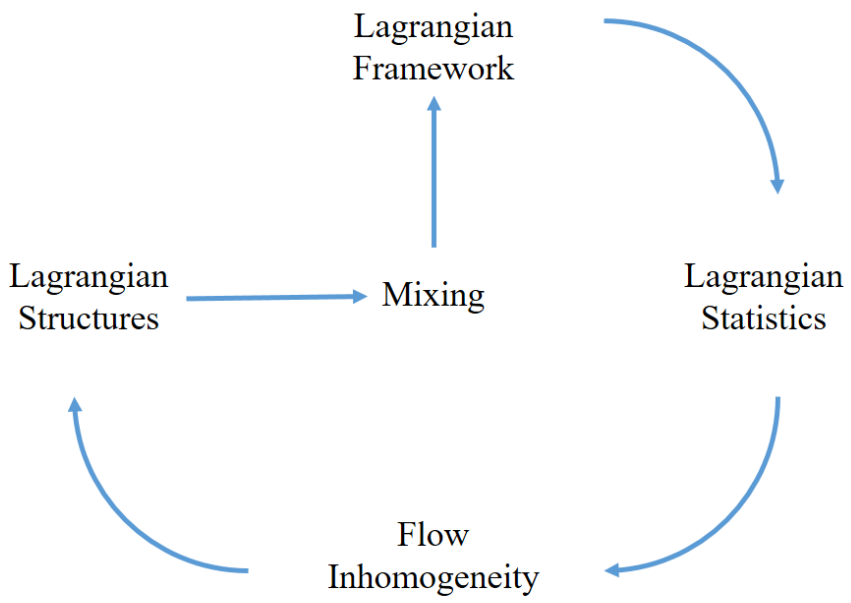

FIGURE 1.1: Conceptual map that describes the theoretical path followed in this Thesis.

relative statistics. Besides, a detailed comparison between the Lagrangian velocity of drifters and the Eulerian velocity of the measured field is carried out. Chapter 5 deals with the same dataset but focuses on the inhomogeneity of the flow. LCS are detected and also compared with drifters trajectories. In Chapter 6 LCS are detected over surface velocity fields of straight compound channels. Straight compound channels are natural or artificial channels made of a main channel and two lateral floodplains. Conclusions are eventually drawn in Chapter 7.

This work introduces several aspects in LCS analysis that sharpen previous knowledge in the field. In particular, the search approach introduced in Chapter 5 tries to join the deterministic approach based on particle trajectories to LCS detection in an innovative way. Applications to real drifter trajectories are shown. Besides, Chapter 6 deals with two particular type of structures: shear and shearless structures. Both types are the less studied in the scientific literature. Compound channels are characterized by their contemporaneous presence. This is the first time that these types of structures are detected from laboratory velocity fields.

Chapter 2

Coherent Structures in Fluid Flows

2.1 Two-dimensional coherent structures

The ubiquitous presence of coherent structures in fluid flows has been known for decades. One of the first systematic visualization of such structures in the modern era is due to Brown and Roshko (1974). They studied the mixing layer of two streams of different gases dominated by large coherent structures. In the framework of their work, coherent structures were mainly associated with vortical structures. In this thesis Lagrangian Coherent Structures refer to the root causes of transport by uncovering special material lines of fluid trajectories that organize the rest of the flow into ordered patterns. However, it is worth noting that already Reynolds in 1883 observed puffs in the transitional pipe flow later investigated by Rotta (1956). From then on, several Authors tried to define coherent structures. Hussain (1983) defined a three-dimensional coherent structure as "a connected, large-scale turbulent fluid mass with a phase-correlated vorticity over its spatial extent". A striking feature of coherent structures is the large-scale transport of mass, heat or momentum. However, the early attempts to define coherent structures relied on an Eulerian approach where high levels of coherent vorticity, Reynolds stresses and turbulent production were sought. Next to the Eulerian approach, a Lagrangian one has become very reliable. Thanks to the latter, a wealth of structures have been detected in the last decade aiming at defining barriers to transport. Such an idea can be better understood from the words of Jerrold E. Marsden[1] appeared in a 2009 New York Times article: "the structures are invisible because they often exist only as dividing lines between parts of a flow that are moving at different speeds and in different directions... They are not something you can walk up to and touch but they are not purely mathematical constructions, either... The line is not a fence or a road, but it still marks a physical

[1] Jerrold Eldon Marsden (1942 – 2010) was the Carl F. Braun Professor of Engineering and Control & Dynamical Systems at the California Institute of Technology.

barrier". Such words well describe the features that are clearly visible in fluid motion. The focus of this work is on two-dimensional coherent structures that are one of the most striking features of geophysical fluid flows. Since the majority of geophysical flows can be studied adopting a quasi-3D approximation, i.e. vertical accelerations can be neglected and the momentum equation along the vertical axis reduces to the hydrostatic approximation, considering geophysical flows as mainly shallow flows is perfectly accepted. For example, main numerical codes as Delft3D (Deltares, 2014) and ROMS (Griffies et al., 2000), broadly used in environmental and oceanographic applications, adopt such an approximation.

Coherent structures have a life cycle consisting of a generation, a growth and a decay. Jirka, 2001a and Jirka and Uijttewaal, 2004 consider the main generation mechanisms that produce coherent structures in shallow flows. The main one is a topographical forcing, i.e. the presence of obstacles in the flow or the abrupt variation of depth. Such a condition generates a flow separation that results in the detachment of the boundary layer that has formed along the body periphery. Typical cases are the wake behind a cylinder that can be considered as a prototypical example of the phenomena that often occur in geophysical flows. This is the case of Figure 2.1 that shows the wake visible in the convected cloud layer downwind from Robinson Crusoe Island, South Pacific.

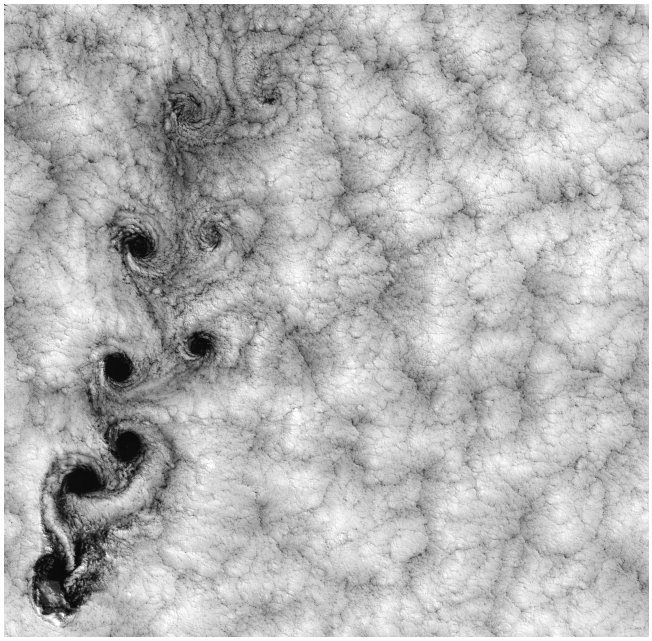

FIGURE 2.1: Satellite picture of a wake visible in the convected cloud layer downwind from Robinson Crusoe Island, South Pacific (source: NASA website).

Another example of coherent structures due to topographical forcings (at a smaller length scale) in geophysical flows are those who protrude from groin fields along rivers. Groins are structures orthogonal to the river axis that are built in order to fix the navigational channel and provide sufficient water depth in low flow periods. However, a recirculation zone is present in the groin fields and lateral momentum

and mass exchange between this zone and the main stream has a direct impact on pollutant and bottom sediment transport. Weitbrecht, Kühn, and Jirka, 2002 and Chrisohoides, Sotiropoulos, and Sturm, 2003 studied such a problem visualizing coherent structures and their developments. Figure 2.2 shows the generation of coherent structures in a laboratory experiment due to groins.

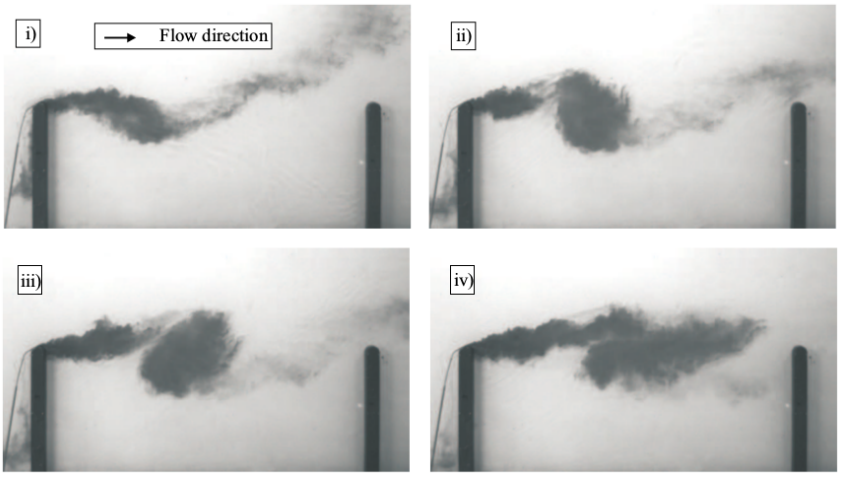

FIGURE 2.2: Mixing layer experiment in laboratory showing coherent structures protruding from groins (source: Weitbrecht, 2004).

A second generation mechanism is due to internal transverse instabilities where velocity variations in the transverse directions give rise to a gradual growth of coherent structures. Shallow jets well represent such a case. Figure 2.3 shows the generation of a meandering structure in a laboratory experiment and a tidal jet outflow from Bodega Harbor, California. In this latter case, the transverse instability is associated with an initial formation of a dipole that is characteristic of narrow channels connecting a basin and the sea (Wells and Heijst, 2004). Another source of transverse instability could be due to topographic variations. Soldini et al., 2004 showed that Eulerian macro-vortices in compound channels are fed by such a mechanism at the transition between the main channel and the floodplain. Figure 2.4 shows such coherent structures in a laboratory experiment. A Lagrangian analysis of such a flow will be presented in Chapter 6.

A third generation mechanism is due to a secondary instability of the base flow. This is the weakest instability. As an example, it is possible to think to a unidirectional flow where turbulence production and dissipation is in equilibrium. The 3D structure of turbulence, in this case, is dominated by bursts and sweeps generated by the bottom-boundary layer. Local disequilibrium can lead to a general redistribution of momentum with the consequently separation of the boundary layer and the formation of coherent structures. A triggering mechanism in such case can be an abrupt variation in bottom friction. Khatibi, Williams, and Wormleaton, 2000 adopted high friction coefficients in order to calibrate a numerical model of an estuary whose tidal

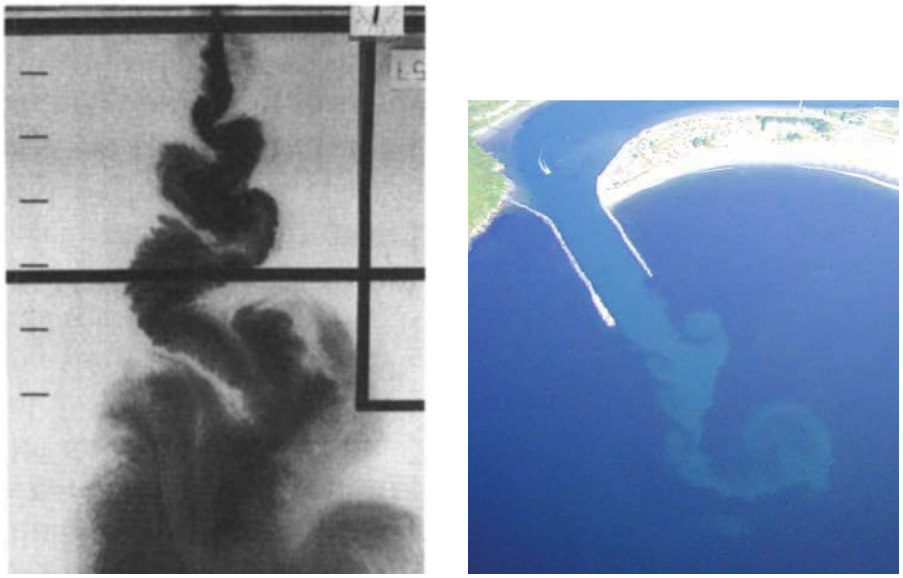

FIGURE 2.3: Shallow jet experiment in laboratory showing meandering coherent structures, on the left (source: Dracos, Giger, and Jirka, 1992). Tidal jet outflow from Bodega Harbor, California (source: Hastings and Gross, 2012), on the right.

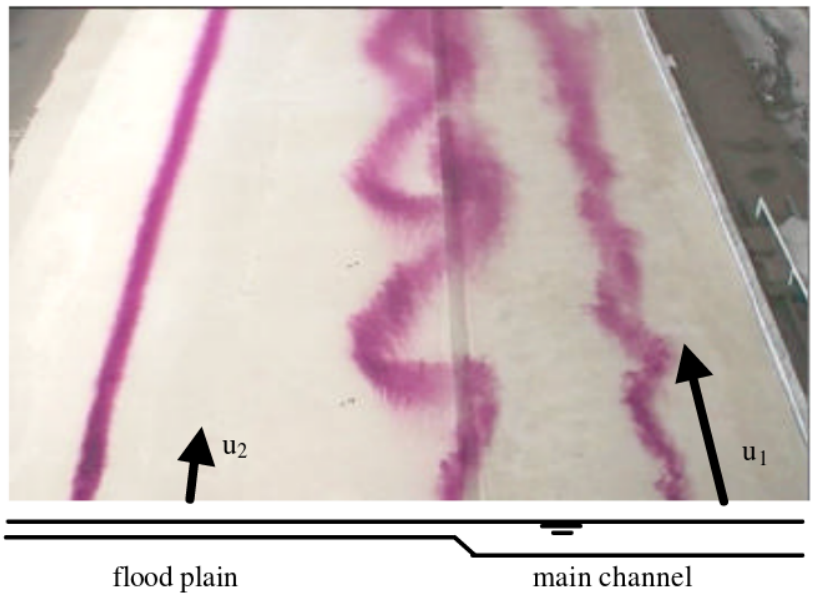

FIGURE 2.4: Large coherent structures are made visible by injecting dye in a compound channel flow. Note the meandering structures at the transition from the main channel to the floodplains (source: Van Prooijen, Booij, and Uijttewaal, 2000).

current was decelerated by high roughness zones. Another example of structures generated by this mechanism are boils in rivers, i.e. localized surface coherent structures resulting of an upwelling motion (Talke et al., 2013). Figure 2.5 shows boil structures captured by infrared images.

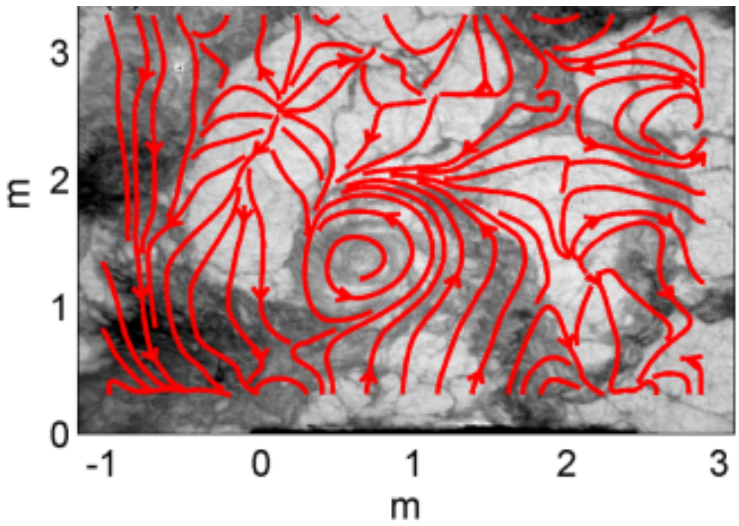

FIGURE 2.5: Infrared image of the surface of the Snohomish river, Washington, showing the anatomy of boil structures and the associated surface streamlines. Boils are marked by divergent streamlines emanating from a common source, while ambient flow is characterized by either parallel streamlines or rotational flow (source: Talke et al., 2013).

Coherent structures can undergo a growth process following their generation. This process depends on the nature of the coherent structures of interest. A dynamical system point of view to study coherent structures will be adopted in the next chapter, and it will shed some light on the topic. Here, it is worth mentioning that Lagrangian coherent vortices, for example, do not show such a behaviour because they are transport barriers trapping the inner fluid mass during their lifetime (Haller and Beron-Vera, 2013). On the contrary, shallow jets can interact and merge (Dracos, Giger, and Jirka, 1992). Another source of growth is due to the entrainment of outside fluid and to the inverse energy-cascade: in two-dimensional turbulence there is the possibility of an inverse energy cascade where energy is transferred from smaller to larger scales. As the eddies grow in size, they become increasingly immune to viscous dissipation. This would not be the case in three-dimensional turbulence in which the eddies continue to decrease in size until viscous effects drain energy out of the flow. Since geophysical flows are mainly two-dimensional, this mechanism applies well (Kraichnan, 1967; Kundu, Cohen, and Dowling, 2012).

Dissipation is due to friction. Coherent structures tend to gradually decay and die if not sustained by some forcing mechanism as, for example, the topographic forcing in compound channels. In shallow flows the main source of dissipation comes from bottom friction.

The introduction to coherent structures here presented deals mainly with the classic features of fluid flows, such as jets, wakes and eddies. This field of research has

been recently enriched by a Lagrangian perspective that will be later adopted. From the Lagrangian perspective, the attention is drawn by particle trajectories. In this case, the heterogeneity of fluid motion is strikingly contrasted by the homogeneity of the medium, i.e. the fluid. Coherent structures gain renewed meaning as boundary curves that divide different dynamical regions of the fluid motion (Samelson, 2013) in analogy to separatrices of a phase space encountered in the geometrical theory of ordinary differential equations. The interest of this approach relies on the detection of lines of large strain called Lagrangian Coherent Structures (Haller, 2015). These show a wealth of structures that go beyond the classic features of fluid motion mentioned in this chapter.

2.2 Diffusive and advective processes

A fluid is made of molecules constantly in motion and colliding with each other. In principle, the motion of a fluid could be described by the time-dependent velocities of each individual molecule. However, this is not feasible and fluids are described as a continuum. In studying fluids as a continuum, two transport properties are present: diffusion and advection. Any passive tracer, i.e. any sufficiently small particle neutrally buoyant whose dynamical behaviour is indistinguishable from that of the fluid, experiences a number of collisions per second, numbering in the billions of billions. As a consequence, a particle quickly loses the memory of its previous velocity and its motion describes a random path. Therefore, the motion of such a particle must be described statistically. The problem can be approached in two ways (Fischer et al., 1979): either by studying the statistics of motion of a single particle and generalizing, or by studying the integrated effect of random motion of a large number of particles simultaneously. The former approach consists in studying diffusion due to Brownian motion as a stochastic random walk. The latter approach consists in applying Fick's law of diffusion in order to describe the spreading of passive tracers with the advection-diffusion equation. In the following, we give a short definition of diffusion and advection in order to introduce the physical interpretation of transport phenomena.

2.2.1 The Random Walk

The easiest way to study the random walk is supposing that the motion of a particle consists of a series of one-dimensional random steps (Banerjee and Rondoni, 2015). We can imagine that the particle moves following random steps of length $\pm\Delta x$ on a line, each one taking a time Δt. Equiprobability for right and left steps is assumed. In the limit of many independent steps the central limit theorem assures that the probability of a particle being between $n\Delta x$ and $(n+1)\Delta x$ approaches the Gaussian distribution with zero mean and variance $\sigma^2 = \frac{t(\Delta x)^2}{\Delta t}$. Assuming that the ratio $\frac{(\Delta x)^2}{\Delta t}$

exists when $\Delta t \to 0$ and naming this ratio as $2D$, the probability that the particle is in position x at time t is

$$p(x,t) = \frac{1}{\sigma\sqrt{2\pi}} \exp\left(-\frac{x^2}{2\sigma^2}\right) = \frac{1}{\sqrt{4\pi D t}} \exp\left(-\frac{x^2}{4Dt}\right) \tag{2.1}$$

The Gaussian distribution obtained in equation 2.1 is the solution to the diffusion equation. It is possible to relate the diffusion equation to the random walk introducing the time evolution of the probability

$$p_{t+\Delta t}(x) = \frac{1}{2} p_t(x - \Delta x) + \frac{1}{2} p_t(x + \Delta x) \tag{2.2}$$

and recovering the discretized form of partial differentiation we obtain

$$\frac{p_{t+\Delta t}(x) - p_t(x)}{\Delta t} = \frac{(\Delta x)^2}{2\Delta t} \frac{p_t(x - \Delta x) + p_t(x + \Delta x)}{(\Delta x)^2 - 2p_t(x)} \tag{2.3}$$

In the limit of $(\Delta x,\, \Delta t) \to 0$ it is possible to obtain the diffusion equation

$$\frac{\partial p(x,t)}{\partial t} = D \frac{\partial^2 p(x,t)}{\partial x^2} \tag{2.4}$$

Equation 2.4 is written in terms of probability of observing a particle at time t in position x. Now, if a whole group of particles begins its wandering at the origin at time zero, the concentration at the position x will be proportional to the likelihood of any one being in the neighborhood of x, that is

$$C(x,t) = \frac{M}{\sqrt{4\pi D t}} \exp\left(-\frac{x^2}{4Dt}\right) \tag{2.5}$$

where M is the total mass of the particles released. Therefore, we can interpret equation 2.4 as the diffusion equation of a scalar quantity (temperature, pollutant, etc.), in which $p(x,t) = C(x,t)$ represents the concentration. A normalization is taken into account.

2.2.2 Diffusion

Diffusion is the integrated view of the result of random motion of a large number of particles at the same time. The triggering transport mechanism in diffusion processes is a concentration gradient in the fluid that generates a net flux $\boldsymbol{q}$ described by Fick's law:

$$\boldsymbol{q} = -D\nabla C \tag{2.6}$$

where D is the molecular diffusion coefficient and ∇C is the concentration gradient. For the mass conservation principle the governing equation without source terms is

$$\frac{\partial C}{\partial t} = D\nabla^2 C \tag{2.7}$$

for a constant, isotropic and homogeneous coefficient D. This equation shows that diffusive processes tend to equilibrate concentration differences finally leading to a constant concentration. The molecular diffusion coefficient in water at ambient temperature is very small with an order of magnitude of $D = 10^{-9}\mathrm{m}^2\mathrm{s}^{-1}$ and therefore can be easily neglected in geophysical applications.

2.2.3 Advection

Advection is the transport process due to a velocity field. While diffusion is a statistical description of irregular motion, advection represents the deterministic counterpart. Let $C(\boldsymbol{x}, t)$ be the concentration field of a passive conservative tracer. The concentration field evolves under a flow as

$$\frac{\partial C}{\partial t} + \boldsymbol{v} \cdot \nabla C = 0 \tag{2.8}$$

The motion of the fluid can be described in two different reference systems: the Lagrangian frame and the Eulerian frame. In the Lagrangian frame we fix our coordinate system to the moving fluid particles and evaluate the processes that act on them. In the Eulerian frame, we use a Cartesian coordinate system fixed in space, which is more convenient for the representation of fields. Differential equations in both frames are related by the material derivative

$$\frac{D}{Dt} = \frac{\partial}{\partial t} + \boldsymbol{v} \cdot \nabla \tag{2.9}$$

At a fixed point in space, a field changes due to inherent local rates of change $\frac{\partial}{\partial t}$ and because the field is advected over the fixed point, represented by the term $\boldsymbol{v} \cdot \nabla$. In the Lagrangian frame the advection equation 2.8 for a conserved tracer is simply

$$\frac{D}{Dt} C(\boldsymbol{x}, t) = 0 \tag{2.10}$$

2.2.4 Advection and diffusion

The combined effects of advection and diffusion leads to the advection-diffusion equation

$$\frac{\partial C(\boldsymbol{x}, t)}{\partial t} + \boldsymbol{v} \cdot \nabla C(\boldsymbol{x}, t) = D \nabla^2 C(\boldsymbol{x}, t) \tag{2.11}$$

This is the Eulerian description of a tracer with uniform isotropic diffusion, i.e. $\boldsymbol{D} = D\boldsymbol{I}$. The Lagrangian description of the same phenomenon can be pursued by a Langevin equation (Fyrillas and Nomura, 2007)

$$d\boldsymbol{x} = \boldsymbol{v} dt + \boldsymbol{B} \cdot d\boldsymbol{W} \tag{2.12}$$

where $\boldsymbol{W}$ are independent Wiener processes and the matrix $\boldsymbol{B}$ is related to the diffusivity tensor through $\boldsymbol{B} = \sqrt{2\boldsymbol{D}}$. As already stated in Section 2.2.2, the molecular

diffusion coefficient is very small. Thus, the advection dominates the diffusion. This is quantified by the Peclet number, which is the ratio between the strength of advection and the strength of diffusion:

$$Pe = \frac{UL}{D} \tag{2.13}$$

where U is the order of magnitude of velocity and L the length scale. Geophysical flows generally are characterized by a Peclet number much greater than unity, showing that diffusion can be neglected. Therefore, the equation for a nondiffusive tracer is

$$\frac{D}{Dt}C(\boldsymbol{x},t) = \frac{\partial C(\boldsymbol{x},t)}{\partial t} + \boldsymbol{v}\cdot\nabla C = 0 \tag{2.14}$$

Since

$$\begin{aligned}\nabla\frac{D}{Dt}C = \nabla\frac{\partial C}{\partial t} + \nabla(\boldsymbol{v}\cdot\nabla C) = \nabla\frac{\partial C}{\partial t} + \nabla\boldsymbol{v}\cdot\nabla C + \boldsymbol{v}\cdot\nabla(\nabla C) = \\ = \frac{D}{Dt}(\nabla C) + \nabla\boldsymbol{v}\cdot\nabla C\end{aligned} \tag{2.15}$$

the tracer gradient ∇C satisfies the following equation (Lapeyre, 2002)

$$\frac{D\nabla C}{Dt} = -\nabla\boldsymbol{v}\cdot\nabla C \tag{2.16}$$

If we consider a two-dimensional flow and we define $\boldsymbol{k}$ as the unit vector normal to the flow, the vector orthogonal to $\boldsymbol{k}\times\nabla C$ satisfies the evolution equation of the distance between two initial particles

$$\frac{D(\delta\boldsymbol{x})}{Dt} = \nabla\boldsymbol{v}\cdot\delta\boldsymbol{x} \tag{2.17}$$

because $\nabla C\cdot\delta\boldsymbol{x} = \delta C$ is conserved as it is a concentration difference between two particles (Városi, Jr., and Ott, 1991). Such a result will be interpreted in the next chapter in light of Lyapunov exponents. Indeed, two directions can be recovered: an unstable and a stable direction characterizing contraction and expansion of fluid elements. The magnitude of the tracer gradient ∇C will decay in time along the unstable direction (Thiffeault and Boozer, 2001).

The description of particle dispersion in terms of diffusion do not provide specific information on trajectories. The objective of this work is to focus on how fluid separate and merge. Many practical transport problems of interest are affected by this chaotic motion of fluids. Typical examples are oil spills where the main interest relies in their exact evolution rather than in the mean behaviour. Advection is the dominant process in these cases. It is therefore an appropriate approach to address the deterministic motion of objects or tracers in the ocean. The emerging patterns can be understood and predicted by analyzing the irregular advective transport as we will see in the following chapters. In this day and age such studies are much more affordable. Numerical ocean models, satellite measurements and high-frequency radar systems can now provide complete spatio-temporal velocity datasets in order to cover

wide areas. There could be an unresolved part of the velocity field at the subgrid scale. However, the obtained flow patterns are most relevant for transport even if the unresoved part is neglected. In particular, methods from dynamical systems theory have proved to be very useful to address finite time transport in such flows. Therefore the advective flow is regarded as a dynamical system, and transport is studied with tools that were originally developed to analyze the phase space of dynamical systems.

The focus of this thesis is on material transport in geophysical flows described by Lagrangian statistics and Lagrangian Coherent Structures as barriers to transport.

Chapter 3

Chaotic transport and dynamical systems

3.1 Basic mixing processes

Fluid flows are essential in many natural phenomena. Atmospheric and oceanic flows are the most striking examples of geophysical flows whose impact on human life is directly perceived on daily basis through weather conditions. Velocity is the key element of all mathematical models used to study transport phenomena in fluid flows. However, velocity is not measured directly. Instead, velocity is a derived quantity, obtained as the ratio between space travelled and time elapsed. Most importantly, we are all interested in the effects of velocity: marine scientists seek the paths of pollutants and nutrients in the ocean and coastguards seeking a drifting boat are interested in its position rather than in its current velocity. Velocity plays the central role on any analysis, but its derived quantities are the real objectives (Lekien and Coulliette, 2007). Until Lorenz, 1963 carried out its seminal work on sensitivity to initial conditions, it was thought that precise knowledge of velocity could lead to a unique trajectory given any initial condition, i.e. to the Lagrangian description of fluid flows. Now, sensitivity to initial conditions is accepted in many natural phenomena and geophysical flows are among them. Such an effect has heavy consequences on the analyses we should carry out on fluid flows and this is the reason why dynamical system theory can be of help. Therefore, even if we consider a non-diffusive tracer as described in equation 2.14, the resulting path will be strongly affected by initial conditions. The integrated view of particle paths gives rise to the mixing pattern. In the following, two examples will be considered. In order to give an idea of what mixing is, let us start from discrete maps that can be viewed as archetypal chaotic maps (Ottino, 1989). In a heuristic way, we can think of mixing as the process that takes

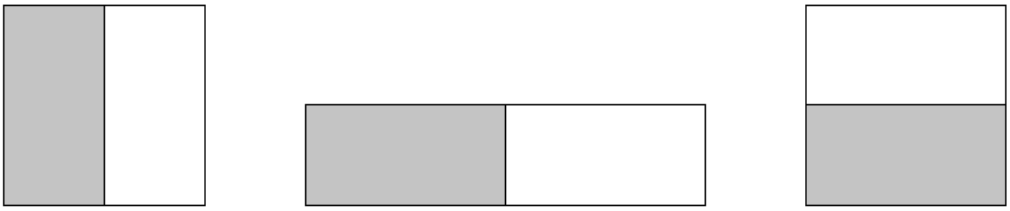

FIGURE 3.1: Pictorial representation of the baker's map. Adapted from Ottino, 1989.

particles close each other and separates them to far and distinct regions of the domain. As a result, close particles at the end of the process comes from distinct regions, i.e. they were far away at the beginning of the process. The baker's transformation is an intuitive example for such a transport configuration, so named by the analogy of rolling and cutting dough. Figure 3.1 shows how the transformation is performed. Starting from a unit square of white and grey material, it is then stretched in one direction and compressed in the orthogonal. Later, the deformed domain is cut and the two pieces are placed side by side. It must be noted that the deformation must preserve the area. This condition is reflected in a fluid flow as the incompressibility constraint, i.e. $\nabla \cdot \boldsymbol{v} = 0$. By successively applying the baker's map to the material on the domain, we obtain an efficient mixing in the sense briefly explained in the following. For simplicity, we choose two subdomains, A to be the bottom half of the unit square and B to be a fixed rectangle. Figure 3.2 shows five iterations of the map. After n iterates A consists of $2n$ strips of width $\frac{1}{2^{n+1}}$. Material in A is so mapped to positions A'. Let N be a number of mappings such that for $n > N$ mappings some material of A is in region B, i.e. A'$\cap$B$\neq \emptyset$. If this is true for almost any A and B, then the map is said to be strongly measure-theoretic mixing the material. Intuitively, this definition states that, as the number of applications is increased, for any region we would have the same proportion of grey and white material. Generally, we deal with flows that are continuous and where cuttings are not possible. Therefore, the second step of the baker's map must be replaced by a folding, obtaining the so-called horseshoe map depicted in Figure 3.3. If we fix our attention to the initial square domain we see that the horseshoe map looses some material and, after successive iterations, entrains other, therefore modelling an open flow. These two discrete maps clarify the notion of mixing. The next step consists in understanding how mixing is achieved in continuous flows. Classic dynamical system theory provides several way to study time-independent flows. A heuristic comparison between these features and patterns observed in geophysical flows will be carried out in the next paragraph. This will open the way to study Lagrangian deformation from an objective viewpoint.

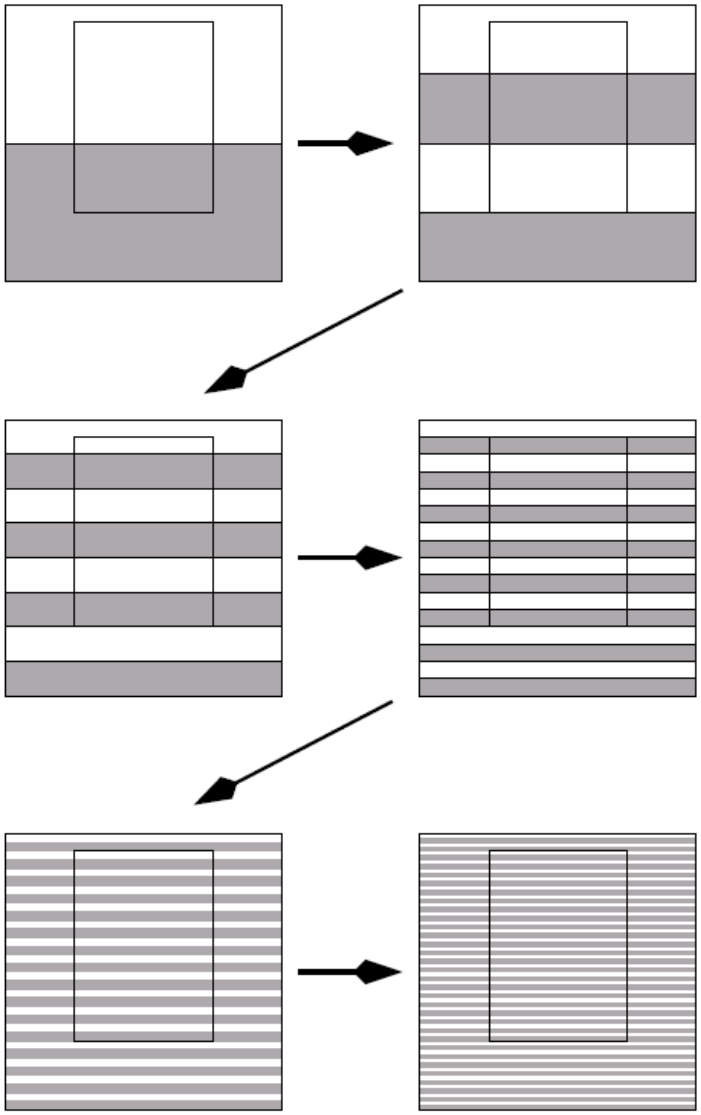

FIGURE 3.2: Successive iterations of the baker's map. The rectangle represents domain B. Adapted from Ottino, 1989.

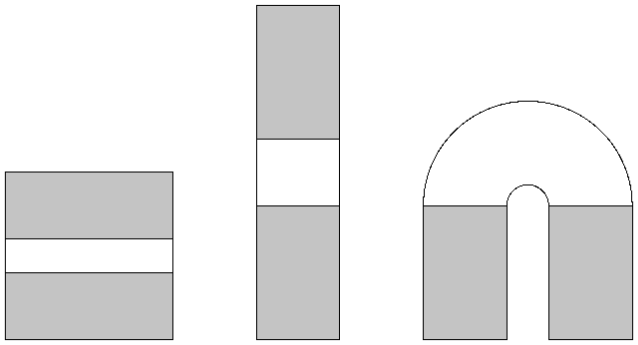

FIGURE 3.3: Pictorial representation of the horseshoe map. Adapted from Ottino, 1989.

3.2 Classic dynamical system features

Coherent structures described in the previous Chapter can be studied applying dynamical system theory. The aim consists in seeking material lines in two-dimensional flows that shape trajectory patterns. Such special lines show robustness to initial conditions and enable a systematic analysis of fluid motion. Classic dynamical system theory defines major features in autonomous systems, i.e. systems not explicitly depending on time, and in time periodic systems. Fluid flows whose particle trajectories are non-diffusive and whose velocity field is time-independent are described by these classic features of dynamical systems that consists in special trajectories. A general

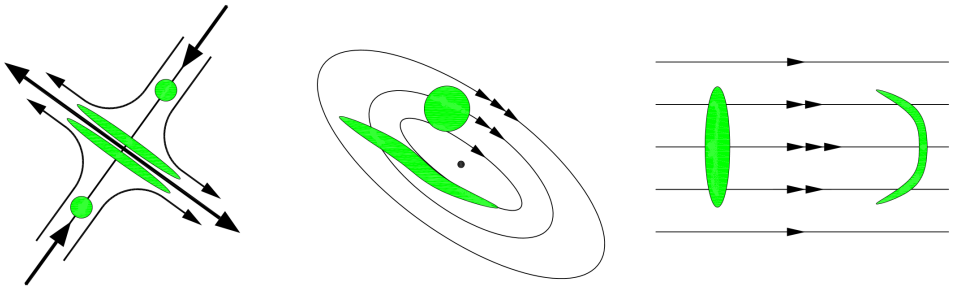

FIGURE 3.4: Classic features in autonomous dynamical systems. From left to right: stable and unstable manifolds of a saddle point, a centre fixed point and a steady shear flow.

view of such special trajectories and a direct comparison with striking fluid flows can point out the scope on analysing time-dependent systems at the light of such a theoretical background. Classic saddle points, stable and unstable manifolds, centre fixed points and steady shear flows can be directly compared to fluid flows whose nature is aperiodic. Figure 3.4 shows such idealized structures of autonomous dynamical systems that can be compared to observed patterns in real geophysical flows. Real trajectories do not exactly reproduce the patterns in Figure 3.4. However, the comparison can be truly inspiring (Haller, 2015). Figure 3.5 shows a nine-mile long oil slick in the Gulf of Mexico resulting from the Deepwater Horizon oil spill and a rip current on Haeundae Beach, South Korea. Both cases compare well with stable and unstable manifolds of autonomous dynamical systems. In the latter, swimmers can be viewed as tracers of the seaward current.

Centre fixed points can be associated with eddies. Figure 3.6 shows a satellite image captured by the Moderate Resolution Imaging Spectroradiometer (MODIS). It shows a natural-colour picture of a deep-ocean eddy on December 26, 2011. The structure of the eddy with its 150-kilometre filamentous inward swirling is traced in light blue by plankton blooming. The picture is taken about 800 kilometres south of South Africa. Such anti-cyclonic eddy likely peeled off from the Agulhas Current, which flows along the south-eastern coast of Africa and around the tip of South Africa. Agulhas eddies tend to be among the largest in the world, transporting warm, salty water from the Indian Ocean to the South Atlantic.

FIGURE 3.5: A nine-mile long oil slick in the Gulf of Mexico resulting from the Deepwater Horizon oil spill, on the left (source: EPA). Rip current on Haeundae Beach, South Korea, on the right. Swimmers can be viewed as tracers of the rip current (source: Bae, Yoon, and Choi, 2013).

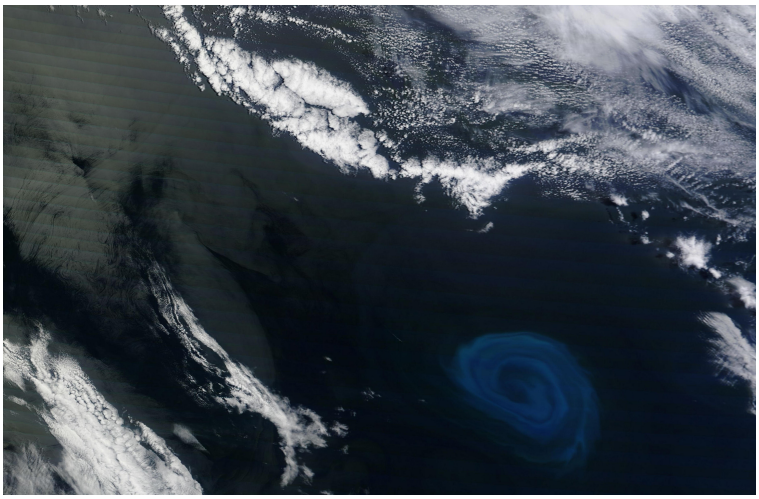

FIGURE 3.6: Eddy traced in light blue by plankton blooming in a 150-kilometer wide swirl (source: NASA website).

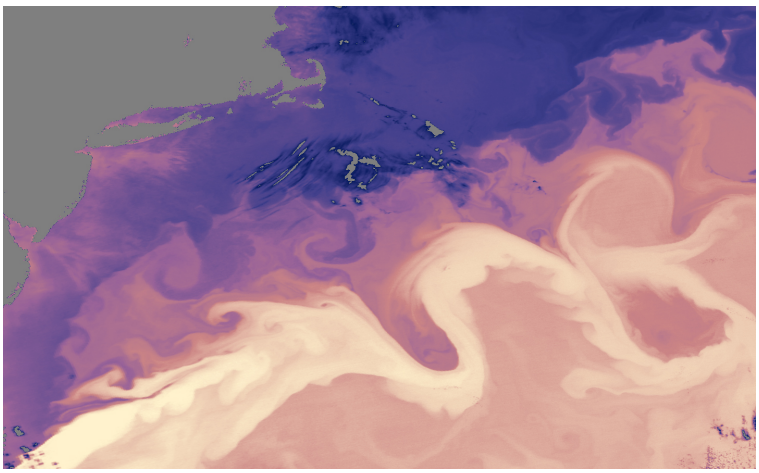

FIGURE 3.7: Sea surface temperature of the Gulf Stream on April 18, 2005 (source: NASA website).

Another interesting comparison can be carried out between the steady shear flow of time-independent systems and Figure 3.7. This image shows the sea surface temperature of the Gulf Stream on April 18, 2005. Warm waters depicted in yellow meandering from bottom left to top right recall a typical pattern of coherent structures mentioned in the previous chapter.

Several authors tried to detect such patterns starting from velocity fields. Two main approaches have been developed: Eulerian and Lagrangian. The former dates back to the seminal work of Okubo, 1970 whereas the latter is much more recent and able to overcome several shortcomings (Haller, 2001; Samelson, 2013; Haller, 2015). In the next section, the objective description of Lagrangian deformation will be introduced.

3.3 Objective description of Lagrangian deformation

A fluid is usually studied applying the well-known results of continuum mechanics (Truesdell and Noll, 2004) and this approach is here adopted. A fluid body $\mathscr{B}$ is made of elements called particles ξ. In order to describe the position of these particles we establish a one-to-one correspondence between the particles and the coordinates of a reference system, i.e. a triple of real numbers. We introduce Lagrangian coordinates $\boldsymbol{\xi} = \left(\xi^1, \xi^2, \xi^3\right)$ as a material coordinate system that label fluid particles. Since any two systems of coordinates are related by a continuously differentiable transformation we can introduce Eulerian coordinates as

$$\boldsymbol{x} = \boldsymbol{\Phi}\left(t; t_0, \boldsymbol{\xi}\right) \tag{3.1}$$

where $\boldsymbol{\Phi}$ is the flow map. The Eulerian coordinates denote the position of a point fixed in what can be called the laboratory frame (Thiffeault and Boozer, 2001). The transformation showed in equation (3.1) can be inverted in the neighbourhood of a point provided that the Jacobian exists and does not vanish (Aris, 1962).

The study of fluid flows cannot be carried out disregarding velocity fields. Indeed, velocity fields are the core of fluid mechanics and time-dependent velocity fields are generally written as $\boldsymbol{v}\left(\boldsymbol{x}, t\right)$. The trajectory of particles are curves solutions of

$$\frac{d\boldsymbol{x}}{dt} = \boldsymbol{v}\left(\boldsymbol{x}, t\right) \tag{3.2}$$

with initial conditions $\boldsymbol{x}\left(t_0, \boldsymbol{\xi}\right) = \boldsymbol{\xi}$.

We can regard equation (3.2) as a set of ordinary differential equations and evaluate on a finite time interval of duration $T = (t_1 - t_0)$ the distance that two initial close particles can experience. Therefore, if we consider as initial conditions $\boldsymbol{\xi}_0$ and $\boldsymbol{\xi}_0 + \boldsymbol{\epsilon}$ we can evaluate the final distance between the two particles applying a linearisation (Allshouse and Peacock, 2015b):

$$\delta\boldsymbol{x}\left(t_1\right) = \boldsymbol{\Phi}\left(t_1; t_0, \boldsymbol{\xi}_0\right) - \boldsymbol{\Phi}\left(t_1; t_0, \boldsymbol{\xi}_0 + \boldsymbol{\epsilon}\right) \approx \nabla\boldsymbol{\Phi}\left(t_1; t_0, \boldsymbol{\xi}_0\right)\boldsymbol{\epsilon} \tag{3.3}$$

where $\nabla\mathbf{\Phi}\left(t_1;t_0,\boldsymbol{\xi}_0\right)$ is called the flow map gradient and it is a tensor represented by a matrix the entries of which are $\nabla\Phi^i_j = {}^{\partial x^i}/_{\partial \xi^j}$. We impose two restrictions on $\nabla\mathbf{\Phi}$. Firstly, an infinitesimal material element $d\boldsymbol{x}$ must not split along its evolution and coalescence of two material elements is not allowed. This is the physical interpretation of the condition on the Jacobian of equation (3.1). The second restriction imposes that the deformation must preserve orientation, i.e. three right-handed material elements $d\boldsymbol{x}$, $d\boldsymbol{y}$ and $d\boldsymbol{z}$ satisfying $d\boldsymbol{x}\wedge d\boldsymbol{y}\cdot d\boldsymbol{z} > 0$ are transformed into three material elements satisfying $d\boldsymbol{x}(t)\wedge d\boldsymbol{y}(t)\cdot d\boldsymbol{z}(t) = (\nabla\mathbf{\Phi}d\boldsymbol{x})\wedge(\nabla\mathbf{\Phi}d\boldsymbol{y})\cdot(\nabla\mathbf{\Phi}d\boldsymbol{z}) = \det(\nabla\mathbf{\Phi})d\boldsymbol{x}\wedge d\boldsymbol{y}\cdot d\boldsymbol{z} > 0$. By writing $\nabla\mathbf{\Phi}d\boldsymbol{x}$ we denote the product between the matrix $\nabla\mathbf{\Phi}$ and the vector $d\boldsymbol{x}$. Scalar product between vectors is indicated as $(\cdot)$. The second restriction implies that the Jacobian of equation (3.1) must satisfy the following condition:

$$J = \det(\nabla\mathbf{\Phi}) > 0 \tag{3.4}$$

The magnitude of the final distance can be evaluated as (Shadden, Lekien, and Marsden, 2005):

$$\begin{aligned} |\delta\boldsymbol{x}\left(t_1\right)| &= \sqrt{\delta\boldsymbol{x}\left(t_1\right)\cdot\delta\boldsymbol{x}\left(t_1\right)} = \sqrt{\left[\nabla\mathbf{\Phi}\delta\boldsymbol{x}\left(t_0\right)\right]\cdot\left[\nabla\mathbf{\Phi}\delta\boldsymbol{x}\left(t_0\right)\right]} = \\ &= \sqrt{\delta\boldsymbol{x}\left(t_0\right)\cdot\left[\boldsymbol{C}\delta\boldsymbol{x}\left(t_0\right)\right]} = \sqrt{\boldsymbol{\epsilon}\cdot\left(\boldsymbol{C}\boldsymbol{\epsilon}\right)} \end{aligned} \tag{3.5}$$

where $\boldsymbol{C}$ is the Cauchy-Green tensor evaluated as $\boldsymbol{C} = \left(\nabla\mathbf{\Phi}\right)^T\nabla\mathbf{\Phi}$ where $(\cdot)^T$ denotes the transpose. It is possible to prove that matrix $\boldsymbol{C}$ is positive definite and symmetric. Since we analyse 2D velocity fields, $\boldsymbol{C}$ has two eigenvectors $\boldsymbol{e}_1$ and $\boldsymbol{e}_2$ associated with two eigenvalues $0 < \lambda_1 \leq \lambda_2$, respectively.

Maximum stretching occurs when $\delta\boldsymbol{x}\left(t_0\right)$ is chosen such that it is aligned with the eigenvector associated with the maximum eigenvalue of $\boldsymbol{C}$, i.e.:

$$\max|\delta\boldsymbol{x}\left(t_1\right)| = \sqrt{\lambda_2}\left|\overline{\delta\boldsymbol{x}}\left(t_0\right)\right| \tag{3.6}$$

where $\overline{(\cdot)}$ indicates alignment with the eigenvector associated with the maximum eigenvalue λ_2 of the Cauchy-Green tensor. Since $\delta\boldsymbol{x}\left(t_0\right) = \boldsymbol{\epsilon}$, equation (3.6) can be recast to obtain

$$\max|\delta\boldsymbol{x}\left(t_1\right)| = \mathrm{e}^{\sigma^{t_1}_{t_0}|T|}\left|\overline{\boldsymbol{\epsilon}}\right| \tag{3.7}$$

where

$$\sigma^{t_1}_{t_0} = \frac{1}{|T|}\log\sqrt{\lambda_2} \tag{3.8}$$

represents the (maximum) Finite-Time Lyapunov Exponent (FTLE) calculated on a finite integration time T. LCS are usually associated with ridges and trenches of FTLE (Shadden, Lekien, and Marsden, 2005; Beron-Vera et al., 2010). Ridges will be studied throughout the whole Thesis whereas trenches will be deeply studied in Chapter 6.

A quantity is called objective if it is invariant under a transformation of the type:

$$\boldsymbol{y} = \boldsymbol{Q}(t)\boldsymbol{x} + \boldsymbol{b}(t) \tag{3.9}$$

where $\boldsymbol{Q}(t)$ is an isometry. If this transformation is applied to equation 3.3, then it is obtained:

$$\delta\boldsymbol{y}(t) = \boldsymbol{Q}(t)\boldsymbol{\Phi}\left(t; t_0\boldsymbol{\xi}_0\right) - \boldsymbol{Q}(t)\boldsymbol{\Phi}\left(t; t_0\boldsymbol{\xi}_0 + \boldsymbol{\epsilon}\right) = \boldsymbol{Q}(t)\delta\boldsymbol{x}(t) \tag{3.10}$$

Since $\boldsymbol{Q}(t)$ is an isometry, the magnitude of $\delta\boldsymbol{y}(t)$ is identical to $\delta\boldsymbol{x}(t)$. Therefore, equation 3.7 is objective under a coordinate transformation and the FTLE is objective. It is worth noting that Eulerian diagnostics for coherent structures are not objective. For example, Okubo-Weiss criterion relies on the spin tensor $\boldsymbol{W} = \frac{1}{2}\left[\nabla\boldsymbol{v} - (\nabla\boldsymbol{v})^T\right]$ that transforms as $\boldsymbol{W'} = \boldsymbol{Q}^T\boldsymbol{S}\boldsymbol{Q} - \boldsymbol{Q}^T\dot{\boldsymbol{Q}}$, where $\boldsymbol{S} = \frac{1}{2}\left[\nabla\boldsymbol{v} + (\nabla\boldsymbol{v})^T\right]$. Therefore, the spin tensor is not objective and so is the Okubo-Weiss criterion. Since Newton's equation for particle motion and the Navier-Stokes equations for fluid motion are well known to be frame-dependent, it might first seem counter-intuitive to require frame-invariance for FTLE and Lagrangian strucutres in general, which are composed of solutions of these frame-dependent equations. However, Newton and Navier-Stokes equations represent objective physical principles for material particle trajectories. Therefore, the transformation from one frame to another yields new terms to the equations: inertial forces. These new terms are introduced in order to ensure that the physical trajectories are the same both in the original reference frame and in the new reference frame.

The Cauchy-Green tensor can be interpreted as the metric tensor. Since we are interested in particle separations, the square distance ds^2 between two infinitesimally separated particles $\boldsymbol{x}(\boldsymbol{\xi}, t)$ and $\boldsymbol{x}(\boldsymbol{\xi} + d\boldsymbol{\xi}, t) = \boldsymbol{x}(\boldsymbol{\xi}, t) + d\boldsymbol{x}(\boldsymbol{\xi}, t)$ is

$$ds^2 = \sum_{l=1}^{n} dx^l dx^l = g_{ij} d\xi^i d\xi^j \tag{3.11}$$

where

$$g_{ij} = \sum_{l=1}^{n} \frac{\partial x^l}{\partial \xi^i}\frac{\partial x^l}{\partial \xi^j} \tag{3.12}$$

is the metric tensor. This point of view leads to the definition on LCS as geodesics of the Cauchy-Green metric (Haller and Beron-Vera, 2012). Further details are introduced in paragraph 3.5.

Since the Cauchy-Green tensor is symmetric and positive-definite, it has n positive real eigenvalues λ_i with corresponding orthonormal eigenvectors $\boldsymbol{e}_i$ (Boozer, 1992). From now on, we will restrict our analysis to two dimensional flows, i.e. $n = 2$. The eigenvectors $\boldsymbol{e}$ define directions of initial separations for which neighbouring particles are converging or diverging. Since we are interested in the more active regions of the fluid flow from a kinematic point of view, we defined the FTLE in

equation 3.8 as a function of the maximum eigenvalue. Thus, two main directions can be recognized, tangent to the eigenvectors associated with the maximum and minimum eigenvalues and called unstable and stable directions, respectively. The magnitude of a tracer gradient ∇C (Equation 2.16) will decay in time along the unstable direction (Thiffeault and Boozer, 2001).

Eckmann and Ruelle, 1985 showed how λ_2 tends asymptotically to a single value λ_∞ as time tends to infinity (Osseledec theorem, valid for autonomous systems):

$$\lambda_\infty = \lim_{T\to\infty} \frac{\log(\lambda_2)}{2T} \tag{3.13}$$

The metric tensor is closely related to the Lyapunov exponents. By imposing the vanishing of the Riemann-Christoffel tensor in flat space, Tang and Boozer, 1996 showed that at times $T \gg \frac{1}{\lambda_\infty}$ the averaged FTLE has the form:

$$\langle\lambda\rangle = \frac{A}{T} + \frac{B}{\sqrt{T}} + \lambda_\infty \tag{3.14}$$

where A and B are constants. Analogously, the standard deviation behaves as:

$$\sigma_\lambda \propto \sqrt{\frac{1}{T}} \tag{3.15}$$

where Δ is a third constant. The probability density function must behave in agreement with the previous theoretical results. As the integration time increases the pdf must narrow, converging to a delta function. Abraham and Bowen, 2002 showed the consistency of these last theoretical results in an analysis carried out on the basis of surface velocity fields of a region of the East-Australian Current. Lapeyre, 2002 finds narrowing pdfs as T increases, due to the decrease of the standard deviation, and a shift of the peaks towards smaller values due to the decaying turbulent field in time he analysed.

3.4 The perturbed pendulum

FTLE have been largely adopted both in idealized and real cases. Several Authors adopted analytical models as benchmarks to validate the dynamical system approach to fluid mechanics. In particular, a double gyre model was much investigated (Allshouse and Peacock, 2015a; Farazmand and Haller, 2012). Here, the perturbed pendulum is presented in order to show how FTLE detect separatrices in the phase space. Such an example has been carefully studied in the past and it is obtained by adding a periodic force to the equation of a simple pendulum that can be found in any textbook in Physics. Therefore, the flow generated by the following coupled differential

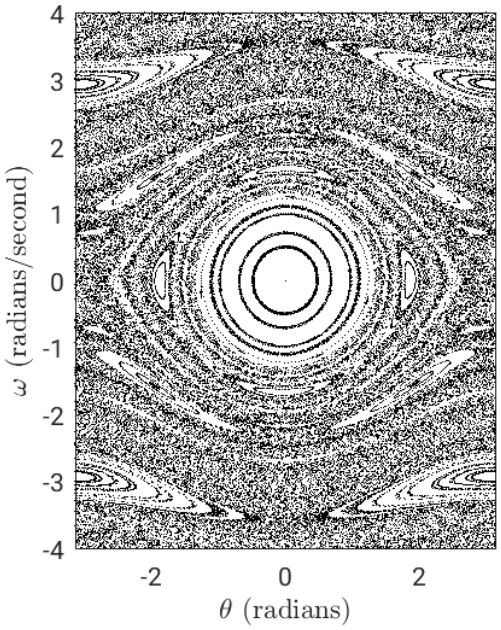

FIGURE 3.8: Poicaré section of the perturbed pendulum of Equation 3.16. Resonance islands and the chaotic sea are revealed.

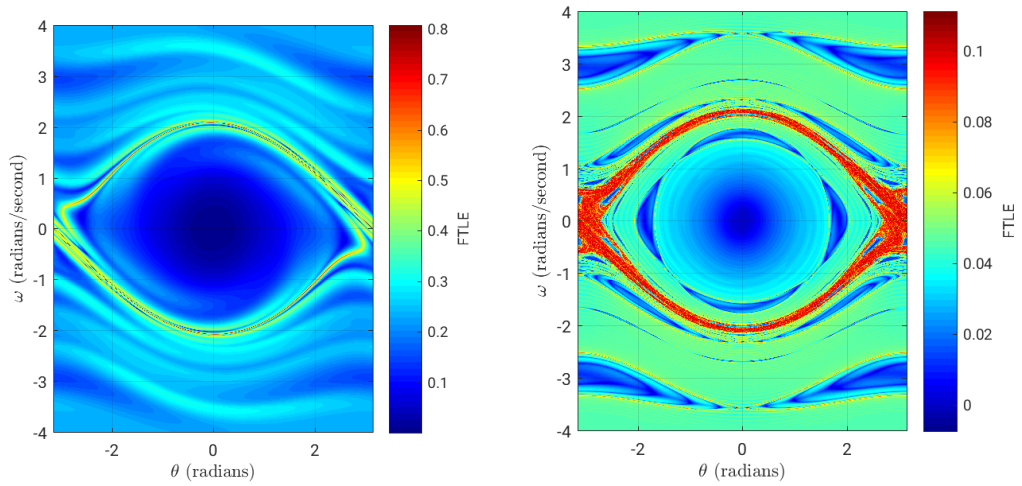

FIGURE 3.9: FTLE forward fields for the perturbed pendulum of system 3.16 calculated with an integration time of T=10 s, on the left, and T=100 s, on the right.

equations is considered:

$$\begin{aligned} \dot{\theta}(t) &= \omega(t) \\ \dot{\omega}(t) &= -\sin\left[\omega(t)\right] - 0.1\omega(t)\sin(\pi t) \end{aligned} \tag{3.16}$$

The system here analysed has a term proportional to a periodic sine. This property allows the analysis of such system through Poincaré sections. Figure 3.8 shows the Poincaré section where resonance islands that persist under the perturbation and

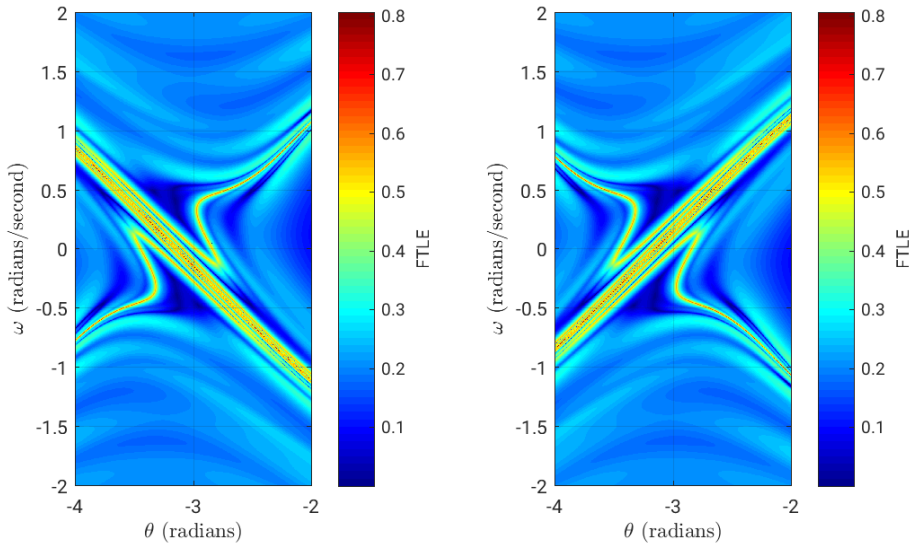

FIGURE 3.10: FTLE forward and backward fields for the perturbed pendulum of system 3.16 calculated with an integration time of T=12 s showing the homoclinic tangle.

the chaotic sea corresponding to chaotic trajectories are clearly detectable. The analysis of system 3.16 adopting FTLE reveals a pattern similar to the one obtained using Poincaré sections. Figure 3.9 shows FTLE forwards fields calculated with an integration time of T=10 s and T=100 s. The choice of the integration time dramatically influences the ridges that can be detected even if the underlying pattern does not change. In particular, at the increase of the integration time the resonance islands are better captured. By properly calibrating the integration time it is possible to disclose a homoclinic tangle (Ottino, 1989) whose presence leads to the emergence of chaotic trajectories. Figure 3.10 shows the homoclinic tangle as a zoom of the FTLE field of Figure 3.9. Forward and backward fields reveal the analogues of stable and unstable manifolds of autonomous dynamical system. The integration time adopted is $T = 12$ s.

3.5 Lagrangian Coherent Structures

LCS detected as ridges of FTLE fields are doomed by several issues. FTLE approach to hyperbolic LCS detection ignores the direction of $\boldsymbol{e}_2$ which may well be along or close to directions tangent to the ridge itself. Indeed, Haller, 2011 gives examples of FTLE ridges along lines of shear. An FTLE ridge should identify the dominant material line on a finite-time interval. However, such identification can be a false one. Besides, in case FTLE ridges remain in place when shifting the time-interval of analysis, such ridges do not behave as material lines. Indeed, there should not be any flux across ridges if they are true material lines. Therefore, a consistent theory of transport barriers was recently developed (Haller and Beron-Vera, 2012; Haller, 2011).

The local theory of LCS is based on the search for the pointwise strongest repelling, attracting, or shearing material lines in the flow over a time interval of interest, the duration of which is the integration time T. At any initial point $\boldsymbol{x_0}$, let $\boldsymbol{n_0}$ denote a unit normal to an initial material line γ_0. While the tangent vector of the line is mapped into a tangent vector of the deformed line by the linearized flow map $\nabla\boldsymbol{\Phi}$, the advected normal generally does not remain normal to the advected line. In addition to a normal component of length ρ, the advected normal also has a tangential component of length σ, as shown in Figure 3.11. If $\rho > 1$, then the evolving material line exerts net normal repulsion on nearby fluid elements. Similarly, $\rho < 1$ signals that the material line attracts fluid elements along its normal direction. In contrast, $\sigma > 0$ indicates shear exerted by the material line on nearby fluid elements. These geometric concepts enable a precise definition of LCS. Specifically, a repelling (attracting) LCS over the interval $[t_0, t_0 + T]$ is a material line whose net repulsion (attraction) is maximal or minimal.

Repelling and attracting LCSs are collectively named as hyperbolic LCS. Similarly, a shear LCS over a finite-time interval is a material line whose net shear is pointwise maximal. Chapter 6 will deal in detail the detection of shear LCS and the Reader is referred to that Chapter for a comprehensive analysis.

Hyperbolic LCS are located as solutions of ODEs. Indeed, the trajectories of $\boldsymbol{r'} = \boldsymbol{e_1}$ (referred either as shrinklines or squeezelines) and those of $\boldsymbol{r'} = \boldsymbol{e_2}$ (stretchlines) decompose the full material deformation into attracting and repelling components. Therefore, a skeleton of the most influential hyperbolic LCS is obtained by finding the locally most repelling shrinklines and the locally most attracting stretchlines. In general, curves tangents to the eigenvectors of the Cauchy-Green tensor are called tensorlines. For the detailed derivation of hyperbolic LCS the Reader is referred to Appendix A.

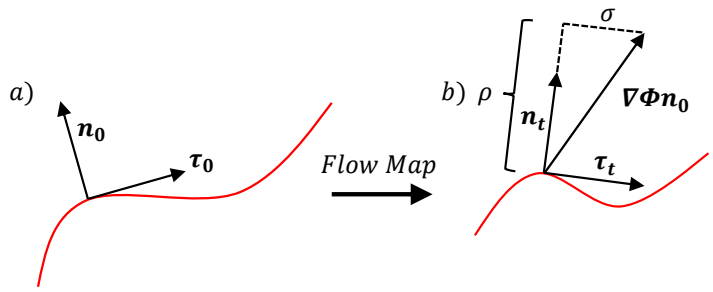

FIGURE 3.11: Advection of a material line. Normal and tangential componentsof $\nabla\boldsymbol{\Phi}\boldsymbol{n_0}$ are named as ρ and σ.

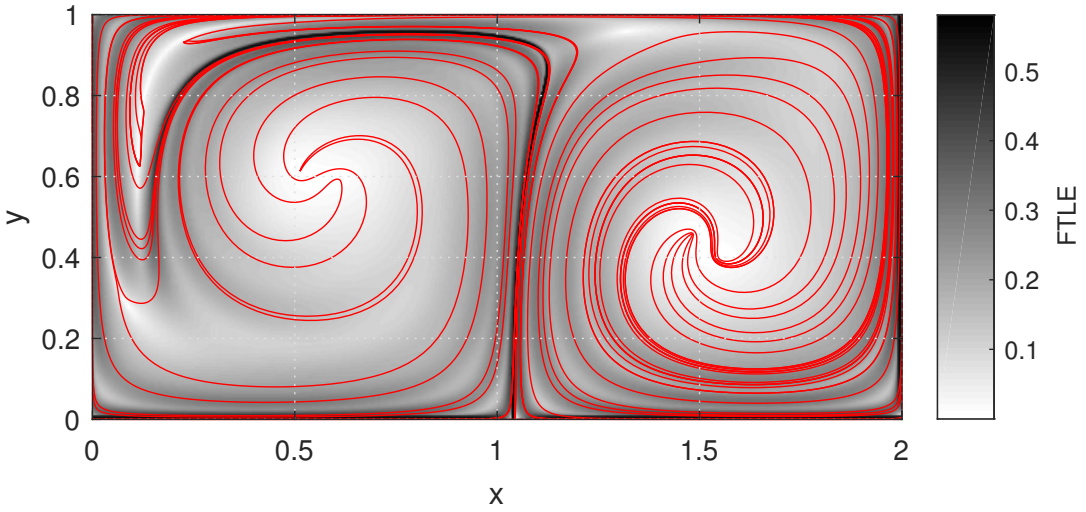

FIGURE 3.12: Double gyre flow: commonly used benchmark to test Lagrangian measures. FTLE field is depicted in grey and repelling structures are depicted in red.

3.5.1 Double gyre

A benchmark analytical case that was deeply studied consists in a double gyre whose velocity field is expressed by analytical expressions. This case is here reproduced in order to let the Reader be introduced to LCS calculated as tensorlines of the Cauchy-Green tensor. This approach will be pursed in the following Chapters and applied to the case of the Gulf of Trieste and in a similar fashion to the case of the compound channel flow. Here, we introduce repelling structures and we superimpose them on FTLE fields.

The analytical velocity field is obtained from the stream function:

$$\Psi(x, y, t) = A \sin(\pi f(x, t)) \sin(\pi y) \tag{3.17}$$

where

$$f(x, t) = a(t)x^2 + b(t)x \tag{3.18}$$

$$a(t) = \epsilon \sin(\omega t) \tag{3.19}$$

$$b(t) = 1 - 2\epsilon \sin(\omega t) \tag{3.20}$$

As a result, the velocity can be estimated analytically as:

$$u = -\frac{\partial \Psi}{\partial y} = -\pi A \sin(\pi f(x)) \cos(\pi y) \tag{3.21}$$

$$v = \frac{\partial \Psi}{\partial x} = \pi A \cos(\pi f(x)) \sin(\pi y) \frac{df}{dx} \tag{3.22}$$

Figure 3.12 shows FTLE field in gray and repelling LCS in red. These are calculated as tensorlines of the Cauchy-Green tensor by solving $\boldsymbol{r'} = \boldsymbol{e_1}$ (Farazmand and Haller, 2012). Calculations are carried out in agreement with Onu, Huhn, and Haller,

2015. These Authors made publicly available a MATLAB Toolbox that represents the basis over which the codes for Chapters 5 and 6 are developed.

These concepts will be applied in the analyses of the datasets of the Gulf of Trieste and of compound channels. Further theoretical results will be introduced when needed along the Thesis.

Chapter 4

Lagrangian Statistics in the Gulf of Trieste

This Chapter focuses on the analysis of a dataset recorded in April 2012 in the Gulf of Trieste (GoT). In particular, a detailed presentation of the dataset composed of surface velocity fields opens the Chapter. Classic Lagrangian statistics from numerical trajectories are calculated (LaCasce, 2008). Therefore, absolute and relative dispersion alongside with their respective diffusivity are evaluated. Besides, the dispersion regimes of the GoT are also evaluated adopting Finite-Size Lyapunov Exponents (FSLE) curves. The assessment of the reliability of velocity fields upon CODE drifter trajectories is eventually carried out.

Studies of the circulation in coastal areas have recently benefited from the use of high-frequency (HF) radars, whose number is rapidly increasing due to their better resolution and reliability with respect to the past. HF radars provide maps of surface velocity with ranges up to 100 km, horizontal resolution of the order 1.5-3 km, and temporal resolution of the order of 0.25-1 h (Gurgel et al., 1999; Harlan et al., 2010; Paduan and Washburn, 2013). Comparisons with Lagrangian drifter measurements near the Californian coasts show mean velocity differences mostly within the range 3-5 cm/s, while differences as large as 20 cm/s indicate that the unresolved spatial variability of velocity fields at subgrid scale may be significant (Ohlmann et al., 2007). Radar coverage depends also on the geometry of the coastline considered and the presence of obstacles of different nature. Furthermore, in severe weather conditions, insufficient signal-to-noise ratios can be registered within some radar cells when strong winds and large waves are present. As a result, holes and gaps can appear in the HF radar velocity maps and the reliability of the transport estimates based on these measures can be questionable. This can be particularly true in small scale embayments or coastal gulfs where radar resolution plays a critical role and local processes and forcings may be important.

In the previous chapther FTLE were defined in order to detect Lagrangian structures in fluid flows. However, another common diagnostic can also be applied: the finite-size Lyapunov exponent (FSLE). Analogously to FTLEs, FSLEs provide a measure of the dispersion as a function of the spatial resolution (Boffetta et al., 2001). The aim is to evaluate the time needed for a pair of particles to reach a defined final separation δ_f. The definition of FSLE reads as:

$$\Lambda\left(\boldsymbol{x}, \delta_0, \delta_f\right) = \frac{1}{|\tau|} \log\left(\frac{\delta_f}{\delta_0}\right) \tag{4.1}$$

where δ_0 is the initial separation between the pairs of particles and δ_f is the target final separation between the same pair of particles reached after a generic time interval τ.

Results achieved by FSLEs and FTLEs are conceptually different, even if their common aim is the search for a rate of a separation. FSLEs operate at fixed length scales: the ratio $\alpha = \delta_f/\delta_0$ is fixed whereas τ, which is the time needed to reach the final separation, is free to vary. On the contrary, FTLEs operate with a fixed time-scale T and detect a separation rate that changes from point to point.

High-resolution velocity inputs for FSLE calculations generally come from numerical models (Haza et al., 2007; Haza et al., 2008) and, contrary to the Atlantic and Pacific oceans, only a few applications using HF-radar velocities can be counted in the Mediterranean Sea (Haza et al., 2010; Berta et al., 2014). This scarcity of applications has two important effects. First, more validations in the Mediterranean Sea of FSLE results vs observed trajectories are needed. A direct comparison of FSLE ridges with drifter data in the Mediterranean Sea can be found only in Haza et al., 2010. Second, the small number of FSLE values registered in the Mediterranean Sea seem to suggest different strengths of the exponential regime, which may depend on the dynamics of the areas considered. Berta et al. (2014) showed the influence of local wind forcing in the FSLE evolution using HF radar measurements in the North Adriatic Sea, finding maximum absolute FSLE values in the order of $\Lambda \approx 1$ day^{-1}. Haza et al., 2010 considered radar velocity outputs in the Gulf of La Spezia (Ligurian Sea) and found FSLE values one order of magnitude ($\Lambda \approx 10$ day^{-1}) larger than in the Adriatic. Most importantly, the values in the Gulf of La Spezia are also an order of magnitude larger than the FSLE values calculated from: i) different realistic ocean models as in Poje et al., 2010; ii) the larger scale drifter measurements in the Liguro-Provençal basin (Schroeder et al., 2011); and iii) the near-surface drifting buoy observations in the Gulf of Mexico (LaCasce and Ohlmann, 2003). This must be seen as a manifestation of a stronger mixing in the Tyrrhenian sea than in the Adriatic Sea since the latter is a closed sea.

Here, the focus is upon a small (~ 20 km $\times$ 20 km) Mediterranean gulf, namely the Gulf of Trieste, located in the upper Northeastern Adriatic Sea. The GoT area was targeted by the EU-MED project TOSCA (Tracking Oil Spills and Coastal Awareness

network, http://www.tosca-med.eu) to investigate and test science-based methodologies, best practices, and response plans in case of accidents at sea (Bellomo et al., 2015). A coastal monitoring network based on HF-radars has been established under the framework of TOSCA with a special emphasis on oil spill pollution and on Search And Rescue (SaR) operations. Thus, the results of the present work have practical applications and are useful to indicate the reliability of Lagrangian transport estimates based on HF-radars velocity fields in case of accidents at sea.

4.1 TOSCA project: the Trieste Gulf area

The GoT is a shallow semi-enclosed basin in the NE Adriatic Sea (see Figure 4.1) with a maximum depth of 25 m. Circulation is generally cyclonic, forced by the incoming Istrian coastal current at the southern border, but intense and frequent wind conditions from the northeastern quadrant produce an east to west current at the surface layer (Malačič and Petelin, 2009). Its oceanographic properties are variable due to pronounced seasonal cycles resulting in thermal stratification during summer and the formation of strong salinity gradients originated by the contrasting effects of fresh water runoffs and seawater exchange at the open boundary (Malačič and Petelin, 2001).

4.1.1 High-frequency radar

HF-radar operation principle is based on the "Bragg scattering" of electromagnetic waves over a rough sea (Crombie, 1955). Radar signals scattered off ocean waves that are exactly half of the transmitted signal wavelength, add coherently and result in a strong return of energy at a very precise wavelength. The Doppler-frequency shift of this return provides information about the velocity of the scattering ocean waves, telling apart speed contributions due to both ocean currents and wave motions (Gurgel et al., 1999).

A network of HF-radars has been installed in the GoT area as part of the TOSCA project in order to provide a full coverage of the gulf area and its closest surroundings. The network consists of three monostatic CODAR SeaSonde systems (Figure 4.1), namely installed at: Aurisina (3° 40' 8.5" E; 45° 44' 28.9" N; Italy), Piran (13° 33' 45.8" E; 45° 31' 42.8" N; Slovenia) and Barcola (13° 45' 15.0" E; 45° 40' 43.0" N; Italy). The working frequency for all three systems has been set to 25 MHz, bandwidth to 150 kHz, for a radial resolution of 1 km. The network configuration ensures an operating range up to 30 km, with an angular resolution of 5° and employs the MUSIC (MUltiple SIgnal Classification) direction finding algorithm (Schmidt, 1986) to derive radial currents on a hourly basis. The standard proprietary SeaSonde Software (Radial Suite and Combine Suite 10R5) is used to geometrically combine the radial information from the HF radar systems and produce total vectorial maps of surface current on a 1.5 km $\times$ 1.5 km Cartesian grid. The SeaSonde Software uses a

least-square fitting method (Lipa and Barrick, 1983; Barrick and Lipa, 1986) to interpolate radials within a local circle with a radius of 2 km. The SeaSonde Software also performs standard quality control checks on both radial and total vectors, removing spikes and grid points with large geometrical dilution of precision (GDOP), i.e. points where radial velocities within the local circle are too close to parallel (stability angles lower than 15° and larger than 165°).

All the computations rely over the surface current information measured by the HF radar network during the period of the TOSCA 2012 experiment, i.e. during April 23 - 30, 2012. During this period, data gaps have been partially filled through a linear interpolation both in space and in time, trying to avoid more complex operations available in literature, like for example the DINEOF analysis (Alvera-Azcárate et al., 2009; Alvera-Azcárate et al., 2011). The motivation for this choice is twofold: on one hand, there is the intention to mimic the operational procedures employed in case of maritime accidents causing spills, when timing is critical and fast computation is a priority, in lieu of employing more accurate and time consuming techniques; on the other hand, the aim is to test the robustness of the Lagrangian analysis even in case of data gaps or with simple and quick filling procedures.

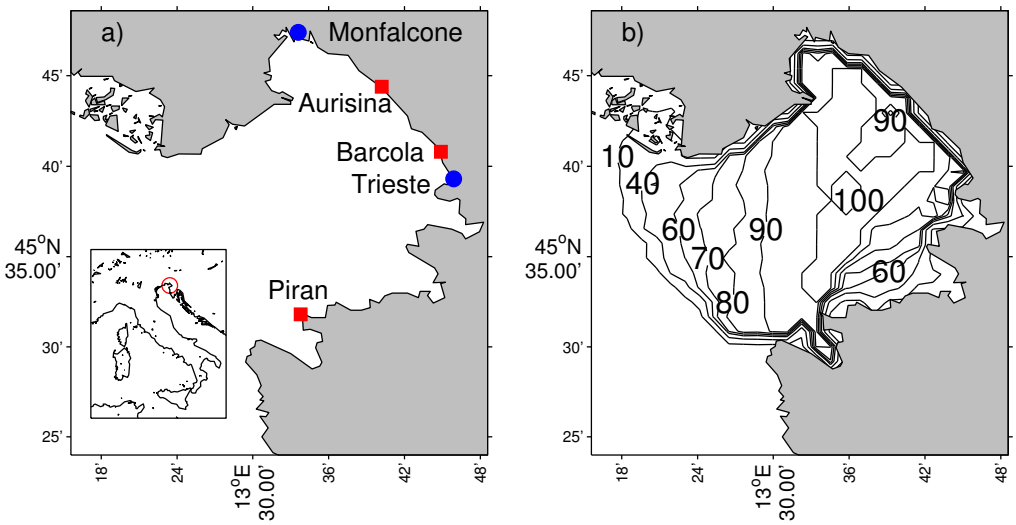

FIGURE 4.1: Radar network locations in the Gulf of Trieste, red squares of Panel a), and percent coverage of the velocity field data derived from HF-radar measurements for April 23 to April 30, 2012, Panel b).

4.2 Absolute dispersion

The description of the mixing properties of a basin is usually carried out by evaluating absolute and relative dispersion. This Section is devoted to the calculation of absolute dispersion. The fundamental theory derived by Taylor (1921) is based on the assumption of homogeneous and stationary turbulence without a mean flow. The presence of a mean flow can alter the results since it causes the absolute dispersion to

increase quadratically in time. Evaluation of absolute dispersion is carried out by applying three different methodologies. The starting point is the calculation of particle trajectories upon surface velocity fields by solving

$$\dot{\boldsymbol{x}} = \boldsymbol{v}\left(\boldsymbol{x}, t\right) \tag{4.2}$$

The numerical trajectories will be employed in the evaluation of absolute dispersion. There is one important feature that highlights the importance of the dispersion problem in the GoT. This is a semi-enclosed basin with an open boundary. Several studies took into consideration basins without lateral walls. Open boundaries and lateral walls strongly influence the Lagrangian time scale and FSLE curves, which show a subdiffusive regime.

4.2.1 Absolute dispersion with respect to initial conditions

This paragraph is devoted to the evaluation of absolute dispersion only with respect to initial conditions, i.e. the movement of the centre of mass is present in the computations. The next paragraph will take into consideration its influence on the results. The absolute dispersion tensor is calculated from particle trajectories (Provenzale, 1999; Mariano et al., 2016)

$$A_{ij}^2(t) = \frac{1}{M}\sum_{m=1}^{M}\left\{\left[x_i^m(t) - x_i^m(t_0)\right]\left[x_j^m(t) - x_j^m(t_0)\right]\right\} \tag{4.3}$$

where M is the number of particles and $\boldsymbol{x}^m(t)$ is the position of the m-th particle at time t and $\boldsymbol{x}^m(t_0)$ is the initial position. The mean-square displacement is given by the trace of $\boldsymbol{A}^2$, usually referred to as the total absolute dispersion:

$$a^2(t) = \text{Tr}\left[\boldsymbol{A}^2(t)\right] \tag{4.4}$$

The total absolute diffusivity is defined as the derivative of the total absolute dispersion:

$$K^{(1)}(t) = \frac{1}{2}\frac{d}{dt}\left\{\text{Tr}\left[\boldsymbol{A}^2(t)\right]\right\} \tag{4.5}$$

Typical dispersion regimes are identified from the time-dependence of A^2. Two regimes are usually detected. For times smaller than the Lagrangian time scale T_{L_i} an absolute dispersion quadratic function of time is recovered, whereas for times greater than the Lagrangian time scale T_{L_i} a linear dependence on time is obtained:

$$A_{ii}^2(t) = \rho_{L_{ii}}(0)t^2 \qquad t < T_{L_i} \tag{4.6}$$

$$A_{ii}^2(t) = 2\rho_{L_{ii}}(0)T_{L_i}t + \text{const.} \qquad t > T_{L_i} \tag{4.7}$$

where T_{L_i} is calculated as the integral of the Lagrangian autocorrelation function. The Lagrangian autocorrelation function of the i-th velocity component is (Guala et

al., 2007)

$$\mathscr{R}_{ii}(\tau) = \frac{\frac{1}{M}\sum_M \rho_{L_{ii}}(\tau)}{\sqrt{\rho_{L_{ii}}(0)\rho_{L_{ii}}(0)}} \tag{4.8}$$

where

$$\rho_{L_{ii}}(\tau) = \langle u'_{L_i}(t) u'_{L_i}(t+\tau) \rangle \tag{4.9}$$

The brackets indicates an average over the entire duration of each trajectory and u'_{L_i} is the i-th Lagrangian component of the residual velocity. In the field of Oceanography, a common way to evaluate residual velocities consists in subtracting from the Lagrangian velocity of a particle an Eulerian mean velocity $\boldsymbol{U}(x, y)$ (LaCasce, 2008; Veneziani et al., 2004). In the present case, the Eulerian mean velocity is easily recovered by averaging the time-signal of the RADAR recorded velocity for each node of the velocity grid. Then, a spatial nearest-neighbour interpolation is employed in order to associate to the velocity of the particle at each time-instance the corresponding mean Eulerian velocity of the nearest node. Therefore, the residual velocities are calculated as $\boldsymbol{u'_L}(x, y, t) = \boldsymbol{u_L}(x, y, t) - \boldsymbol{U}(x, y)$.

The Lagrangian time scale is then defined as

$$T_{L_i} = \int_0^{+\infty} \mathscr{R}_{ii} dt \tag{4.10}$$

Such quantities are computed over the numerical trajectories solution of equation 4.2. However, an initial time must be set in order to carry out the computations. Typically, the initial time is set to coincide with the starting time of the available dataset. In the framework of the present work, such computations are carried out recursively by changing the initial time. The initial conditions of the computations are therefore changed and a different result is obtained at every iteration. This procedure is adopted in order to assess whether the field observed is statistically stationary or not. Figure 4.2 shows Lagrangian autocorrelation function for both x and y components, i.e. in the west-east and south-north directions respectively. Grey curves are evaluated at the different initial conditions whereas the black curve represents the average. Auto-correlations do not vanish for long times and show a persistent correlation even after 90 hours. Figure 4.3 shows the x and y Lagrangian time scales plotted against the initial condition. The Lagrangian time scale can be generalized as $T_L = \frac{1}{2}(T_{L_x} + T_{L_y})$. The average over all the initial conditions is almost 2h. T_{L_x} is persistently higher than T_{L_y} due to the open boundary of the Gulf of Trieste on the Adriatic Sea whose orientation form an angle greater than 60° with the x-axis (West to East direction).

Panel a) of Figure 4.4 shows the total absolute dispersion $a^2(t)$ as a function of time. Grey curves are evaluated at the different initial conditions and the black curve represents the average. Red curves represent theoretical behaviours. Such behaviours are almost followed by the average. While the Lagrangian time scale is quite robust at the varying of the initial conditions, the absolute total dispersion shows at least one order of magnitude of difference between the curves, suggesting that the results

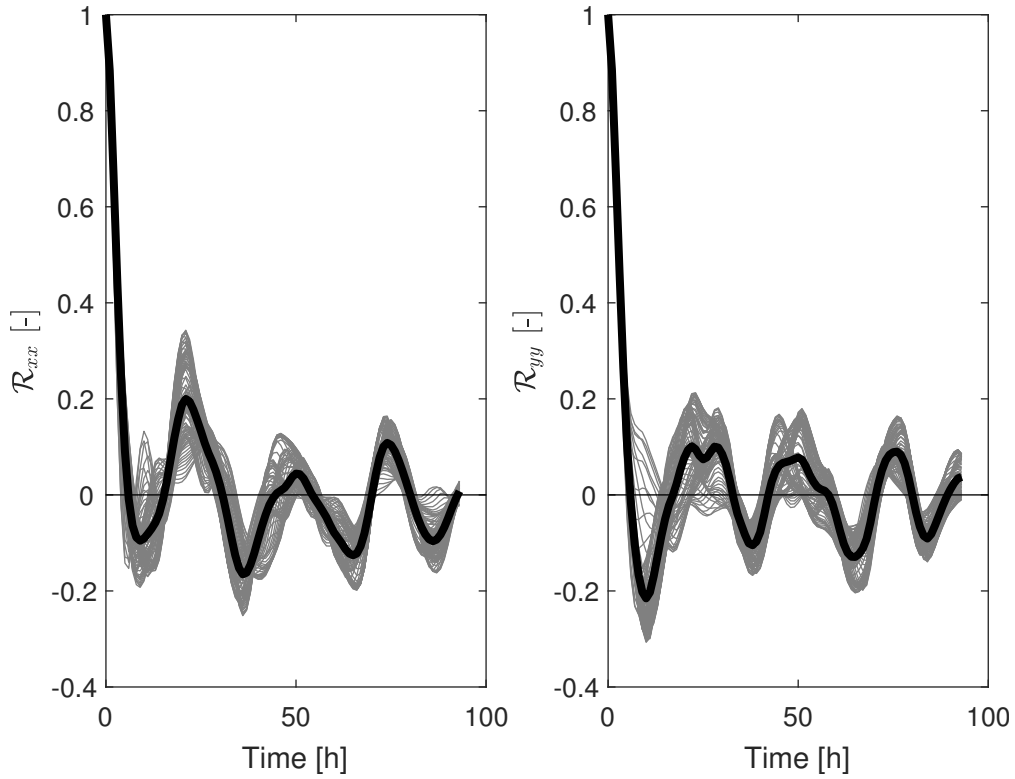

FIGURE 4.2: Lagrangian autocorrelation functions $\mathscr{R}_{xx}(\tau)$ and $\mathscr{R}_{yy}(\tau)$.

are not independent from the initial time. The thin black vertical line of panel a) shows the section along which the values of total absolute dispersion are plotted on panel b). The x-axis of Panel b) represents the initial condition at which the value of a^2 refers to and must not be confused with the x-axis of panel a). Panel b) shows an oscillating curve having a period whose order of magnitude is 24h. It can be heuristically associated with the diurnal tide.

A further observation on panel a) shows that the grey curves tend to overlap one over each other as time elapses. However, note that panel a) is plotted on a log-log scale and therefore the absolute difference of two values belonging to different grey curves evaluated at the same time instance have several order of magnitude of difference. For this reason, it is possible to quantify if the curves tend to narrow by adopting a normalization. Then, it is possible to evaluate the standard deviation of the normalized values for each time:

$$F(t) = \frac{\text{sdt}[a^2(t)]}{\text{mean}[a^2(t)]} \tag{4.11}$$

Figure 4.5 shows the decreasing behaviour of $F(t)$ even if a strong oscillating signal is present. As a result, the bunch of grey curves actually tend to overlap relatively

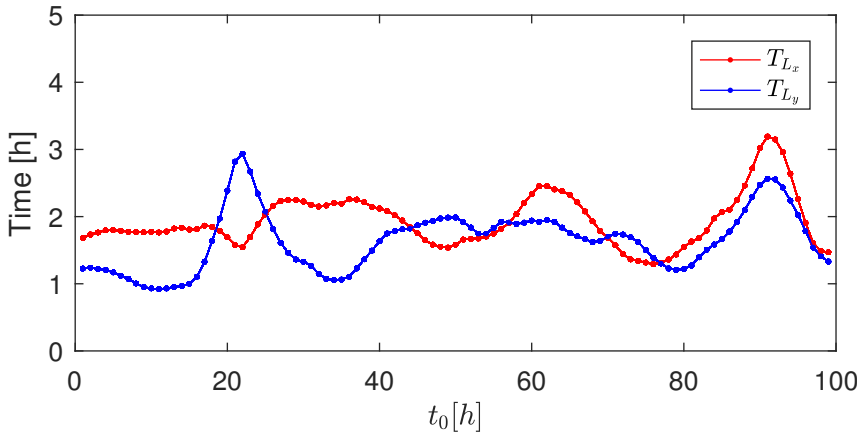

FIGURE 4.3: Lagrangian time scales T_{L_x} and T_{L_y}.

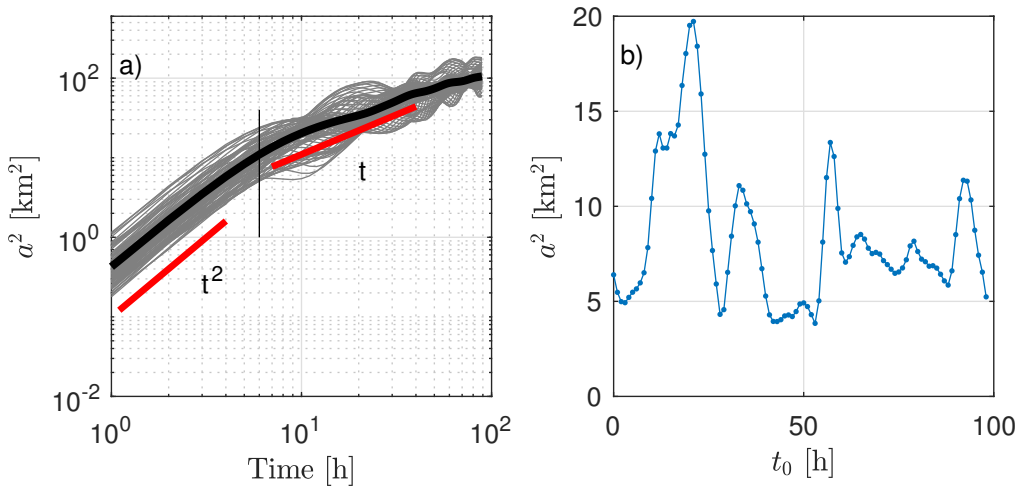

FIGURE 4.4: Panel a) shows total absolute dispersion $a^2(t)$. Panel b) shows total absolute dispersion along the section represented as a thin black line in Panel a).

to the average. Such a result suggest that the relative importance of the initial condition decreases as time elapses. As the Lagrangian time scale T_L shows after how much time from the deployment of particles a change of regime occurs (dependence from time t on the plot of the total absolute dispersion), the function $F(t)$ evaluates the influence of the initial conditions on the strength of the absolute total dispersion after a time t. In case the function $F(t)$ would not decrease, the influence of the initial conditions would persist even for long times. The periodicity is analogue to panel b) of Figure 4.4.

Given the trends of equations 4.6 and 4.7, the behaviour of $K^{(1)}(t)$ should be linear and constant in time respectively. Figure 4.6 shows such behaviours. The constant plateau is reached for times slightly longer than the Lagrangian integral scale computed.

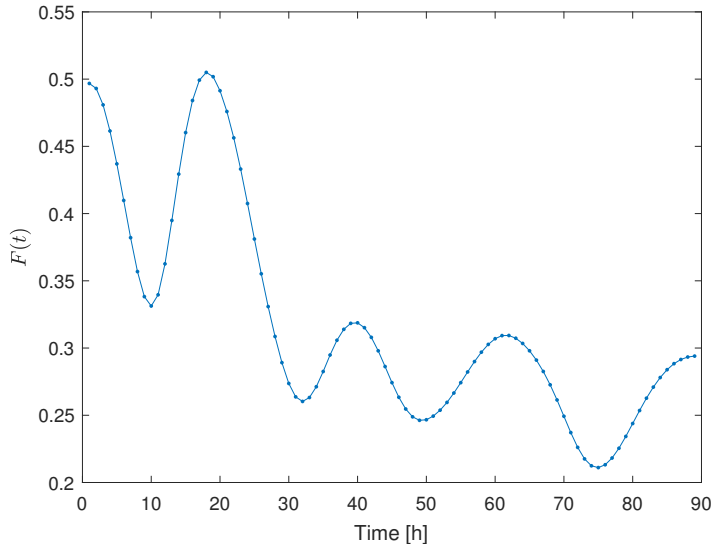

FIGURE 4.5: Function $F(t)$ describing the variance of the normalized total absolute dispersion.

4.2.2 Absolute dispersion about the centre of mass

While autocorrelations and Lagrangian integral time scales are calculated once for all, the evaluation of absolute dispersion can be pursued taking into consideration the mean drift (LaCasce, 2008; LaCasce, 2000). The mean drift can be calculated as

$$L_i(t) = \frac{1}{M} \sum_{m=1}^{M} [x_i(t) - x_i(t_0)] \tag{4.12}$$

The spread about the center of mass can be measured as

$$D_i^2(t) = \frac{1}{M-1} \sum_{m=1}^{M} [x_i(t) - x_i(t_0) - L_i(t)]^2 \tag{4.13}$$

The total absolute dispersion about the center of mass can be evaluated as

$$d^2(t) = D_x^2(t) + D_y^2(t) \tag{4.14}$$

Figure 4.7 shows $d^2(t)$ as a function of time. Compared with Figure 4.4, the solution is smoother and the bunch of grey curves tend to oscillate less. By adopting the definition of equation 4.13 it is possible to avoid the influence of the mean drift from the computations and take into consideration directly the cloud size. This is reflected into the fact that the average curve depicted in black in panel a) of Figure 4.7 tends to a horizontal plateau for long times. On the contrary, the average curve of panel a) of Figure 4.4 shows a persistently increasing total absolute dispersion.

Panel b) of Figure 4.7 shows the presence of a periodicity analogously to the previous paragraph. However, the total absolute dispersion does not reach values as high as before since the mean drift is disregarded by the calculations.

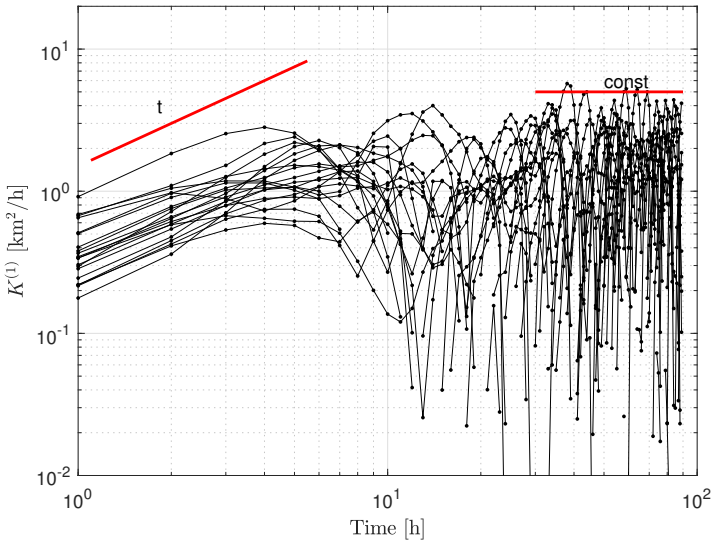

FIGURE 4.6: Total absolute diffusivity $K^{(1)}(t)$. Both linear and constant behaviours are present.

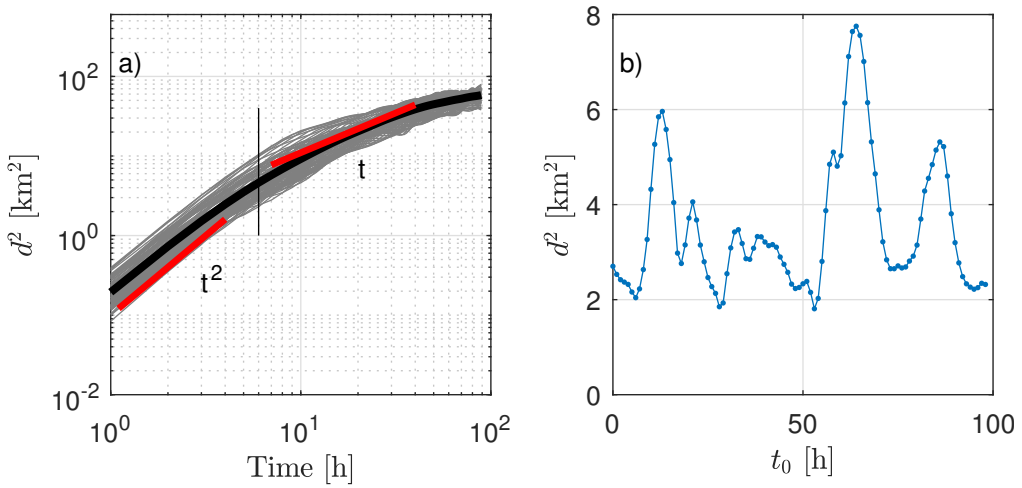

FIGURE 4.7: Panel a) shows total absolute dispersion $d^2(t)$. Panel b) shows total absolute dispersion along the section represented as a thin black line in Panel a).

Figure 4.8 shows the function $F(t)$ calculated as in the previous paragraph. The periodicity is damped due to the absence of mean drift.

The total absolute diffusivity is defined analogously to the previous Section as

$$K_d^{(1)}(t) = \frac{1}{2}\frac{d}{dt}\left[d^2(t)\right] \tag{4.15}$$

Figure 4.9 shows the behaviour of the diffusivity: both the linear and constant trends are recovered.

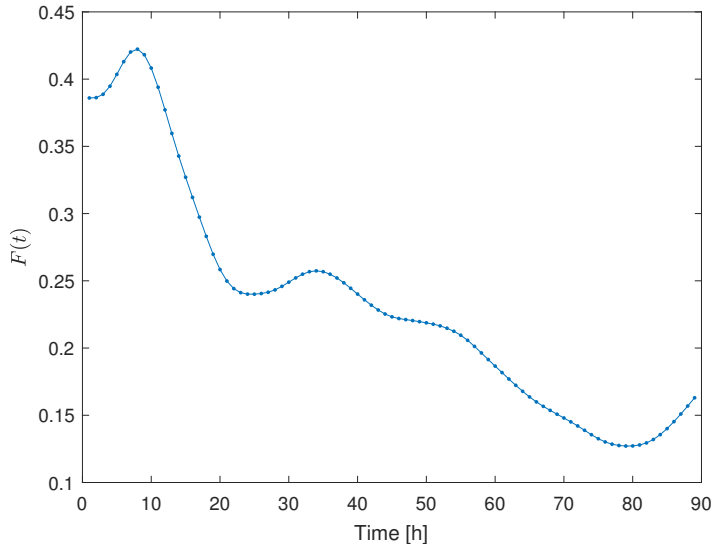

FIGURE 4.8: Function $F(t)$ describing the variance of the normalized total absolute dispersion d^2.

4.2.3 Absolute Dispersion with respect to residual

Another possible way to calculate absolute dispersion is to take into consideration residuals (Zavala Sansón, 2015). Residuals are defined as

$$x_i'(t) = x_i(t) - \frac{t}{T}\int_{t_0}^{T} u_{L_i} dt \tag{4.16}$$

where T is the duration of the numerical trajectory and u_{L_i} is the Lagrangian velocity of the particle. Total absolute dispersion $a'(t)$ is directly calculated employing equation 4.3 with residuals. Panel a) of Figure 4.10 shows a trend that resembles the one obtained disregarding the mean drift (cf. Figure 4.7) since for long times $a'(t)$ tends to a plateau. However, in this case the residuals are obtained subtracting a quantity that can be directly associated to an average and therefore the function $F(t)$ depicted in Figure 4.11 shows the presence of a periodic signal. Diffusivity $K_r^{(1)}(t)$ plotted in Figure 4.12 shows both linear and constant trends.

Absolute dispersion is here calculated with three different methods. The most reliable is the one that considers the centre of mass. In this way, a mean drift is not considered in the total dispersion. Another important statistics is the relative dispersion that will be analysed in the following.

4.3 Relative dispersion

Relative dispersion is defined as the mean-square distance at time t between a pair of particles that at time t_0 have a distance equal to r_0:

$$R_{ij}^2(t) = \frac{1}{M-1}\sum_{m=1}^{M-1}\left\{\left[x_i^m(t) - x_i^{m+1}(t)\right]\left[x_j^m(t) - x_j^{m+1}(t)\right]\right\} \tag{4.17}$$

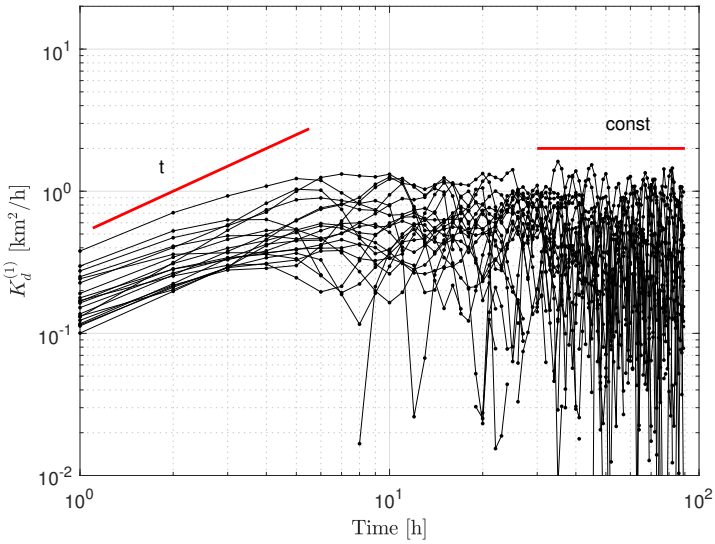

FIGURE 4.9: Total absolute diffusivity $K_d^{(1)}(t)$. Both linear and constant behaviours are present.

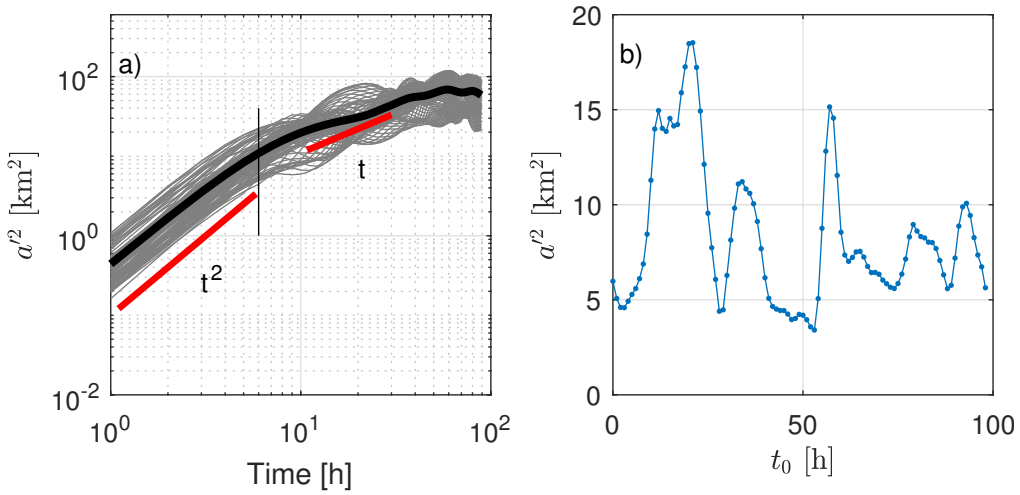

FIGURE 4.10: Panel a) shows total absolute dispersion $a'^2(t)$. Panel b) shows total absolute dispersion along the section represented as a thin black line in Panel a).

where $M-1$ is the total number of particle pairs. The total relative dispersion can be defined as:

$$r^2(t) = \text{Tr}\left[\boldsymbol{R}^2(t)\right] \tag{4.18}$$

The time derivative of relative dispersion is the relative diffusivity:

$$K^{(2)}(t) = \frac{1}{2}\frac{d}{dt}\left\{\text{Tr}\left[\boldsymbol{R}^2(t)\right]\right\} \tag{4.19}$$

Relative dispersion regimes typically depend on the initial separation r_0 and on the forcing injection scale in the flow r_I. In particular it is possible to recollect the following:

$$K^{(2)} \propto r^2 \qquad \text{for} \quad r_0 < r_I \tag{4.20}$$

$$K^{(2)} \propto \left(r^2\right)^{2/3} \qquad \text{for} \quad r_0 \geq r_I \tag{4.21}$$

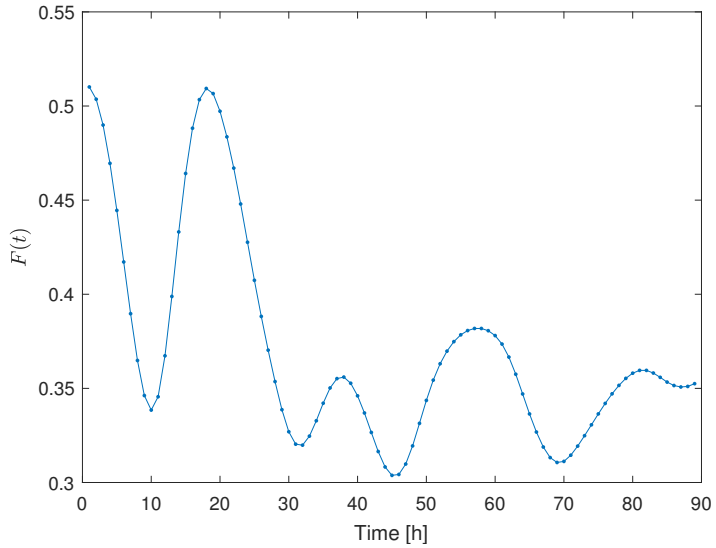

FIGURE 4.11: Function $F(t)$ describing the variance of the normalized total absolute dispersion $a'^2(t)$.

$$K^{(2)} = const. \qquad \text{for} \quad r_0 \gg r_I \tag{4.22}$$

and r_I can be regarded as the Rossby radius of deformation. The first regime belongs to the enstrophy cascade in two-dimensional turbulence and corresponds to non-local dispersion where the particles are advected by structures greater than the initial separation. The second regime belongs to the energy cascade where the celebrated Richardson law is recovered. Particles disperse randomly in the third regime since they belong to different flow structures. Therefore, relative dispersion should behave as

$$r^2 \propto \exp(\alpha\chi^{1/3}t) \qquad \text{for} \quad r_0 < r_I \tag{4.23}$$

$$r^2 \propto t^3 \qquad \text{for} \quad r_0 \geq r_I \tag{4.24}$$

where α is of order one and χ is the rate at which enstrophy is transferred to scales shorter than r_I. Malačič and Petelin, 2009 evaluated the Rossby radius of deformation from numerical models in the GoT to be 2.16±0.5km during spring. This length is considered as the injection scale in the present work.

Figure 4.13 shows the total relative dispersion r in a logarithmic scale in order to visualize a linear relation of the type

$$\ln r_i = \ln r_0 + c_i t \tag{4.25}$$

where $c_i = \alpha\chi^{1/3}$. The procedure of changing recursively the initial condition is employed and the black curves represent the average trends. The other curves are omitted in favour of readability. Red curves are the best fit over the first 20h with values of c_i ranging from 0.098 to 0.157 h^{-1}. The theoretical cubic trend is shown in green.

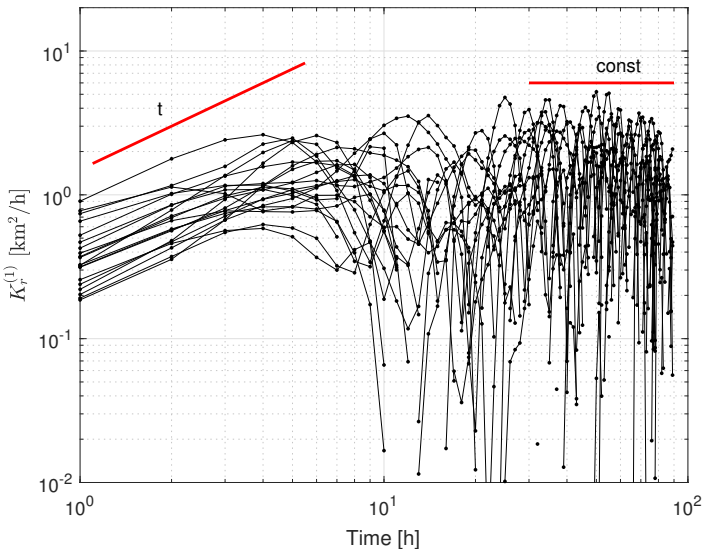

FIGURE 4.12: Total absolute diffusivity $K_r^{(1)}(t)$. Both linear and constant behaviours are present.

Relative diffusivity is plotted in Figure 4.14 with the theoretical trends. Additional information on dispersion can be gathered from pdfs of particles' displacement shown if Figure 4.15. At the increase of the initial separation the kurtosis tend to decrease. Separations smaller than r_I show large values of kurtosis, whereas at larger separations the kurtosis tend to gaussianity (kurtosis equal to 3).

4.3.1 Vortex Merging

Particle pairs initially separated by a distance smaller than r_I will experience relative dispersion that grows exponentially and cubically in time. On the contrary, particles pairs initially separated by a distance greater than r_I will directly experience a cubic growth. It is possible to argue that the first case is a direct consequence of vortex merging (Stocchino et al., 2011). Vortex identification can be pursued adopting the swirling strength. Swirling strength is defined as the imaginary portion of the complex eigenvalue of the local velocity gradient tensor (Adrian, Christensen, and Liu, 2000). The idea of analysing eigenvalues of the velocity gradient tensor $\nabla \boldsymbol{v}$ is described by Okubo, 1970. The eigenvalues of the velocity gradient tensor are:

$$\lambda_{\pm} = \frac{1}{2}\left(\partial_x u + \partial_y v\right) \pm \left[\frac{1}{4}(\partial_x u - \partial_y v)^2 + \partial_x v \partial_y v\right]^{1/2} \tag{4.26}$$

Introducing the well-known differential properties it is possible to characterize the eigenvalues. The differential properties are:

- divercence: $\nabla \cdot \boldsymbol{v}$;
- normal strain rate: $s_n = \partial_x u - \partial_y v$;
- shear strain rate: $s_s = \partial_x v + \partial_y u$;

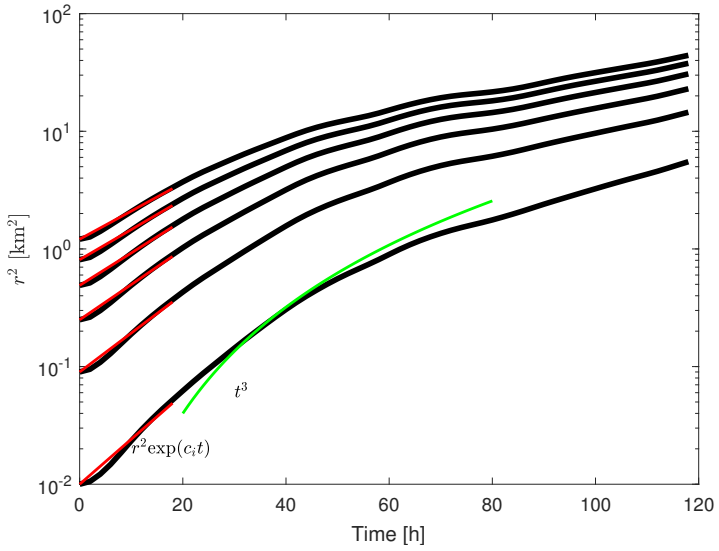

FIGURE 4.13: Total relative dispersion r. Red curves are best fit of the exponential growth. The green curve is the theoretical cubic growth.

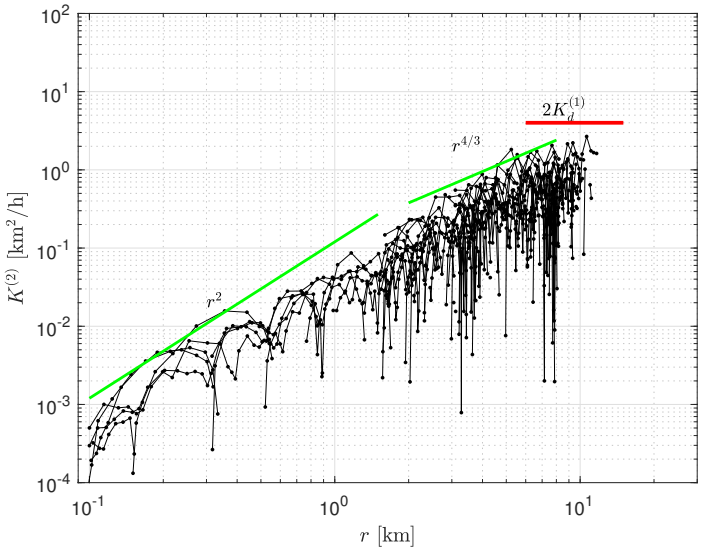

FIGURE 4.14: Relative diffusivity.

- vorticity: $\omega = \partial_x v - \partial_y u$.

Therefore the eigenvalues can be rewritten as

$$2\lambda_{\pm} = \nabla \cdot \boldsymbol{v} \pm (s_n^2 + s_s^2 - \omega^2))^{1/2} \tag{4.27}$$

The sign of the Okubo-Weiss parameter $OW = s_n^2 + s_s^2 - \omega^2$ determines whether the eigenvalues are real or imaginary. A negative Okubo-Weiss parameter is associated to a rotational movement in an elliptic region of the domain.

The presence of vortex merging can be assessed from Figure 4.16 where two vortices merge together in following time-steps. This can explain the presence of an exponential regime, at least partially.

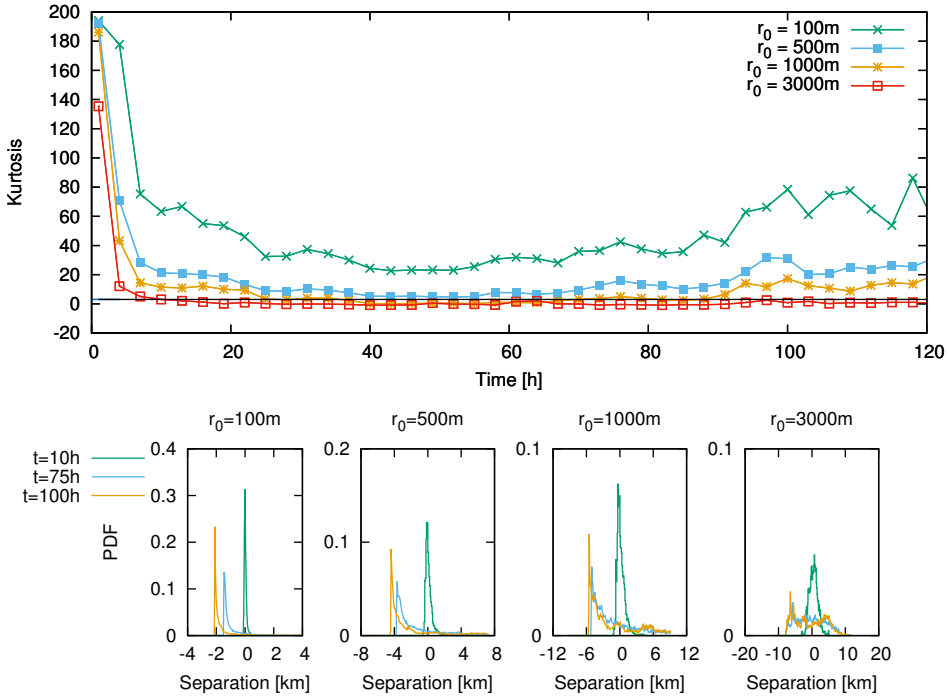

FIGURE 4.15: pdfs & kurtosis.

4.3.2 Dispersion regimes from FSLE curves

The approach pursued in the previous paragraphs sometimes presents a shortcoming: particle pairs with the largest separations can dominate such statistics. In order to address this issue Artale et al., 1997 investigated the relative dispersion of passive tracers introducing a typical inverse time FSLE $\Lambda(\delta)$ that characterizes the dispersion process at fixed scales δ. Such an approach provides useful information on the different dispersion regime at increasing scales. Schroeder et al., 2011 recalls the existence of three different regimes with respect to the deformation radius. For the submesoscale range, i.e. for lengths smaller than the deformation radius the dispersion is expected to be exponential. For lengths larger than the deformation radius the Richardson law is expected to rule. For even greater distances, the dispersion is expected to be linear. This means that FSLE $\Lambda(\delta)$ curves show different behaviours at the increase of δ: firstly a constant plateau followed by a trend proportional to $\delta^{-\frac{2}{3}}$ and δ^{-2}, respectively. Subdiffusive regimes proportional to a power law $\delta^{-\beta}$ with $\beta > 2$ can be associated with particles trapped in eddies or boundary constraints.

Haza et al., 2008 calculated FSLE $\Lambda(\delta)$ curves from synthetic data generated by a model of the Adriatic Sea and tested how the FSLE $\Lambda(\delta)$ curves change if the model velocity fields were filtered temporally or spatially. They evaluated an exponential growth of the order of 0.6 days^{-1} for $\delta < 10$ km. Haza et al., 2010 calculated FSLE $\Lambda(\delta)$ curves in the Gulf of La Spezia from original pairs adopting a ratio $\alpha = 1.2$. They obtained a quite important variability for ten different realizations even if each realization presented a quite constant behaviour, ranging from a $\Lambda(\delta) \approx 4$ day^{-1} to

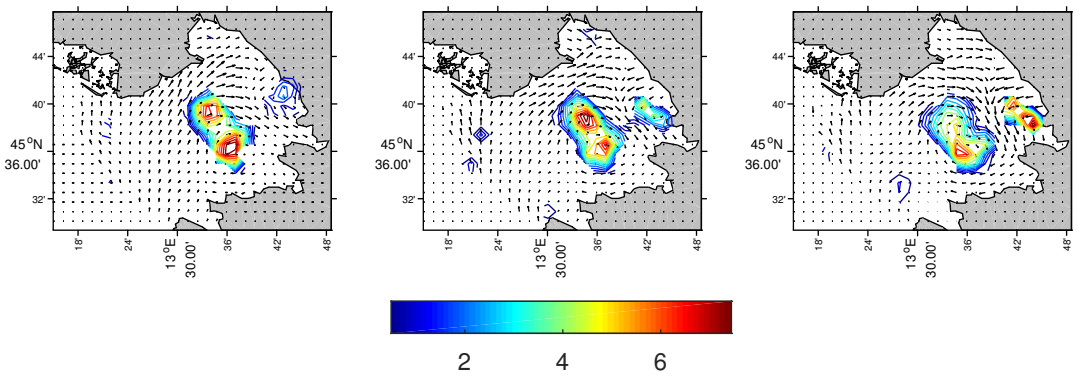

FIGURE 4.16: Swirling strength detects vortex merging. Values are to be multiplied by 10^{-10}.

$\Lambda(\delta) \approx 10$ day^{-1}. Poje et al., 2010, who studied an idealized buoyant coastal current modelled using ROMS and the Gulf Stream region with a realistic HYCOM simulation, indicated an exponential growth for $\delta < 50$ km with a value approximately equal to 0.4 day^{-1}. Schroeder et al., 2011 studied the Liguro-Provençal basin finding values of the exponential regime varying between 0.7 day^{-1} to 1 day^{-1} for δ in the range 1-10 km. At smaller scales, for 0.1-1 km $\Lambda(\delta)$ values tended to increase to a value of 2 day^{-1}.

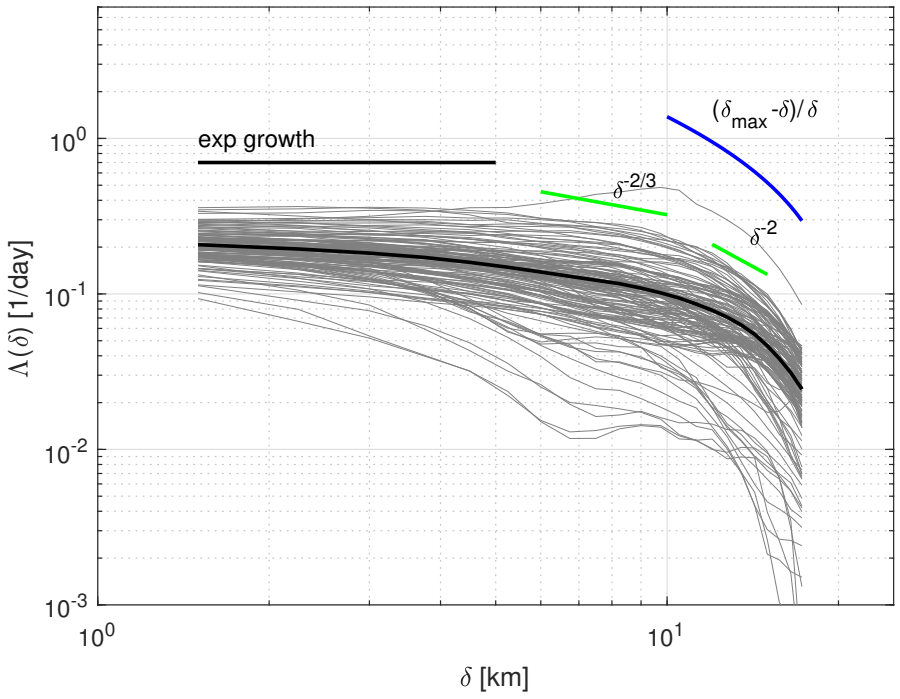

FIGURE 4.17: FSLE values as a function of separation δ. Thin gray lines are evaluated for different initial conditions (starting time), while the thick black line represents the averaged value over all the simulations.

FSLE $\Lambda(\delta)$ curves are here evaluated through original pairs. Since the measured

velocity fields have a 1.5 km resolution in space, smaller scales will not be considered. Following Haza et al., 2008 curves for several different initial conditions are evaluated (i.e., date of simulation start, showed in gray thin lines in Figure 4.17) and estimated their mean value (black solid line in Figure 4.17). Following Haza et al., 2008, FSLE curves are calculated setting separations that increase recursively as:

$$\delta_n = \alpha\delta_{n-1} \tag{4.28}$$

where α is equal to 1.2. The trends show the existence of an exponential regime with values ranging between 0.12 and 0.37 day^{-1}. The average strength is approximately 0.22 day^{-1}, whose order of magnitude is in agreement with the findings of Haza et al., 2008 and Schroeder et al., 2011 on analogous length scales. Furthermore, as the separation δ increases, the FSLE slope suggests the presence of both the Richardson regime ($\sim 6 < \delta <\sim 10$ km) and the linear regime ($\sim 10 < \delta <\sim 13$ km).

For the bigger spatial scales, as pointed out by Artale et al., 1997, the behaviour of FSLE curves should follow the theoretical one $\Lambda(\delta) \propto \frac{\delta_{max}-\delta}{\delta}$ when approaching length scales of the maximum dimension of the basin δ_{max}. Such a behaviour is shown in Figure 4.17 with a blue curve where the spurious subdiffusive regime is a result of the boundary constraints.

4.4 CODE drifters

During the 2012 TOSCA April experiment in the GoT, a total number of 41 CODE (Coastal Ocean Dynamics Experiment) drifters (Davis, 1985; Poulain, 1999) have been launched. This number includes the cases where drifters were caught and relaunched in order to maintain coverage of the HF radar area. CODE drifters are undrogued and suited for the first meter below the surface and for a direct comparison with the HF radar velocities. They are designed to minimize slippage due to the direct action of wind and waves, whose errors are estimated to be within 1-3 cm/s for wind up to 10 m/s (Poulain et al., 2009). CODE positions are retrieved every 15 minutes via Global Positioning System (GPS) receivers with an accuracy of approximately 5-10 m. Drifter raw data have been edited to remove outliers and spikes and interpolated at uniform 1-h intervals (Hansen and Poulain, 1996). Drifter velocities have been computed by central finite differences.

It is important to note that HF-radar and drifter-based velocities may differ because of the nature of their samplings, both in the vertical and horizontal dimensions. In the vertical, HF-radar velocities are the exponentially-weighted averages of the upper ocean velocity profile. As a result, they depend on the vertical shear of the horizontal current and on the HF-radar frequency (Stewart and Joy, 1974; Ivonin et al., 2004). For the working radar frequency of 25 MHz used in GoT and under the assumption of a linear vertical shear, the radar measurement corresponds to an average over an effective depth of about 50 cm which is half the vertical dimension

of the CODE drogue. The mismatch between the two types of measurements is even more evident in the horizontal dimension: HF radar velocities are quantities averaged over grid cells whose sizes are in order of kilometers. Drifters, on the contrary, are affected by scales of motions comparable to their physical horizontal size, i.e. of the order of 1 m for the CODE-type used here. In this study, 26 of the above CODE drifter trajectories are considered, discarding those lasting less than 12 hours because considered not reliable.

4.4.1 Reliability of drifter simulations and HF-radar velocity fields

Availability of recorded velocity-fields and drifters trajectories enables to perform comparisons between:

- drifter and HF-radar velocities;
- observed drifter trajectories and simulated trajectories based on HF-radar velocity fields.

Bellomo et al., 2015 carried out an overall comparison of the previous quantities for all the TOSCA sites. Their considerations on HF-radar and drifter-based velocities concerning sampling methods for the former and scales affected by the latter are the same in the framework of the work. In the next paragraphs such comparisons will be exploited for the GoT.

4.4.2 Comparison between drifters and HF-radar velocities

This Section presents a comparison between the Eulerian velocity fields derived from the HF-radar measurements and the Lagrangian velocity calculated from the registered positions of the drifters.

Similar analysis have been previously discussed by several Authors and it is worth mentioning among others Bellomo et al., 2015, Rohrs et al., 2015 and Ohlmann et al., 2007. In order to compare the present results with the cited works, it is essential to define the quantities one desires to test. In fact, Bellomo et al., 2015 as well as Rohrs et al., 2015 adopted the radial velocities, i.e the projection of current velocities along the line of sight of radars. Note that radial velocities are the first output of the HF-radar. Ohlmann et al., 2007 together with a comparison between HF-radar radials presented a specific analysis using the Eulerian velocities, derived from the radial measurements, in terms of single cartesian components. All Authors provided a measure of agreement between HF-radar velocities and drifters velocities in term of time-averaged root mean square of the differences.

As far as the present study is concerned, the interest relies in evaluating the reliability of the Eulerian velocity fields, being the velocity datasets used for the Lagrangian analysis presented in the next Chapter, and, whenever it is possible, to test the present results against previous estimates.

Furthermore, the role of data gaps in the HF-radar velocity measurements on the estimate of Eulerian and Lagrangian quantities, with a particular attention to the prediction of numerical trajectories is evaluated. It is not unlikely that HF-radar radial or total velocity fields might experience the presence of data gaps for a particular time frame, for the reasons already discussed. An example is shown in Figure 4.18, where quite a significant part of the GoT basin is not covered by the velocity data. In this case, interpolation/extrapolation algorithms are implemented in order to overcome this problem. The question now being asked is what influence might have velocity gaps on the estimation of different Eulerian and Lagrangian properties of the surface circulation.

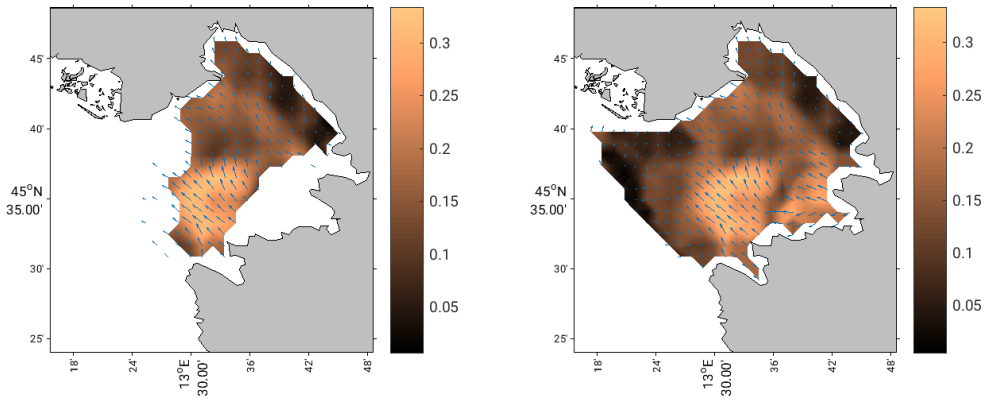

FIGURE 4.18: Example of extrapolation velocity field for 27^{th} April 2012 at 03:00 UTC . Velocity expressed in [m/s]. Left: original measurements. Right: reconstructed velocity field.

The time-averaged root mean squared velocity U_{rms}^{mod} is defined for each drifter as:

$$U_{rms}^{mod} = \sqrt{\frac{1}{N}\sum_{i=1}^{N}(|\boldsymbol{u}_{Eul_i}| - |\boldsymbol{u}_{Lag_i}|)^2} \tag{4.29}$$

where N is the number of positions, $|\boldsymbol{u}_{Lag_i}|$ is the drifter velocity module at the i-th position and $|\boldsymbol{u}_{Eul_i}|$ is the HF-radar velocity module interpolated on the same position. The HF-radar is reconstructed using a bicubic spatial interpolation of the surrounding velocities around the single drifter position in order to test a more accurate algorithm. The rms defined by Equation (4.29) should play the role of radial velocities when the eulerian velocity fields are considered.

The computation of the time-averaged root mean square of the difference has been repeated for three cases: using the complete data set, including the data gaps, excluding the data gaps from the data and, finally, considering only the data gaps. The comparison among the three cases will help in highlighting the influence of the data gaps in the HF-radar measurements.

The results of the computation of U_{rms}^{mod} for the ensemble of 26 drifters are shown in Figure 4.19, where the horizontal axis represents the drifters label. On the same plot, the averaged value over all data has been reported as a red line, whereas the

grey area above represents a range of plus one standard deviation. The overall averaged rms value is very close to 10.0 cm/s, which is perfectly in line with previous studies where an averaged rms in a range 5-15 cm/s has been observed and considered acceptable (Paduan and Rosenfeld, 1996; Chapman et al., 1997; Ohlmann et al., 2007; Molcard et al., 2009; Huhn et al., 2012; Bellomo et al., 2015). Indeed, the comparison between radial velocities carried out by Bellomo et al., 2015 led to a root mean square of 9.6 cm/s for the GoT site, which is very close to the present result. Morever, both the present results and the ones obtaned by Bellomo et al., 2015 are comparable with previous observations in the surroungings of the GoT described in Cosoli et al., 2013, where averaged rms velocities in a range from 7.5 cm/s to 9.9 cm/s are reported. Starting from the case where the whole data are considered, red dots and line, the results suggest that the data gaps generally tends to decrease the accuracy of the velocity estimation, leading to higher U_{rms}^{mod} (blue dots and line). On the other hand, excluding the data gaps decrease the averaged value of the time-averaged root mean square of the difference (black dots and line). With respect to the general trend described above, there are some exceptions. In fact, quite a few drifters do not encounter any HF-radar data gaps, e.g. drifters 6, 20 and 24. Moreover, the expected improvement derived from excluding the data gaps does not occur in several cases, see Drifter 8, 16, 29, 33 and 53, or it is not detectable, e.g. Drifter 32 and 13. The latter behavior is related to a very low number of gaps, which results in minor differences.

However, the estimated value of the average U_{rms}^{mod} considering only the data gaps remains contained within the interval of one standard deviation with respect to the averaged value computed with the whole data, suggesting that, from an Eulerian point of view, they do not influence considerably the quality of the total velocity fields. Note that the estimated values are consistent with the analysis performed by Bellomo et al., 2015 with the radial velocities and are in line with the usual expectations of difference of the order of 5-15 cm/s.

By inspecting Figure 4.19, few drifters fall outside the varibility of one standard deviation, namely Drifter 5, 8 and 20 where their U_{rms}^{mod} reach value between 13 and 17 cm/s. A detailed investigation of the behaviour of the latter drifter trajectories is carried out with the goal to explain the higher rms velocities. In particular, their trajectories, shown in Figure 4.20, leave the center of the Gulf heading for the boundaries where HF-radar velocities are known with low accuracy owing to a lower coverage. This fact, together with the transformation of the radial velocity fields, might be responsible for a lower accuracy of the reconstructed velocity.

Moving to the analysis of the single eulerian components, the root mean square velocities is defined as:

$$\mathrm{RMSE_x} = \sqrt{\frac{1}{N}\sum_{i=1}^{N}(u_{Eul_i} - u_{Lag_i})^2} \tag{4.30}$$

$$\mathrm{RMSE_y} = \sqrt{\frac{1}{N}\sum_{i=1}^{N}(v_{Eul_i} - v_{Lag_i})^2} \tag{4.31}$$

where u_{Eul_i} and v_{Eul_i} are the x-component and y-component of the Eulerian fields, respectively. The values obtained for the present dataset are shown in Figure 4.21, together with the standard deviations, represented with error bars, for each drifter. Note that the behaviours of $\mathrm{RMSE_x}$ and $\mathrm{RMSE_y}$ is randomly distributed within the drifters ensemble. On the contrary, the results presented by Ohlmann et al., 2007, relatively to a similar analysis, seem to be affected to some systematic effect. As a result, the rms of the x-component of the velocity is consistently higher than the y-component for all drifters in one site and an opposite behaviour has been observed on the other site.

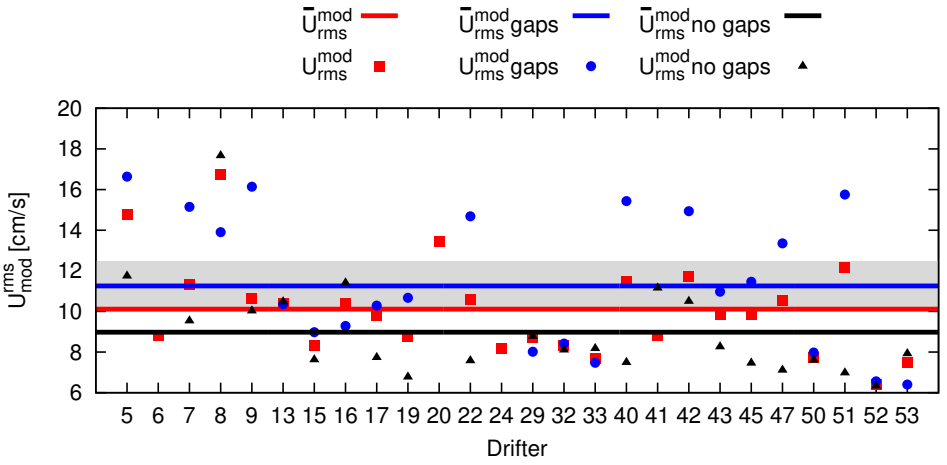

FIGURE 4.19: U^{mod}_{rms} evaluated for the three cases described in the text: the results obtained with entire dataset in red, results obtained considering the data gaps in blue and, finally, results excluding the data gaps in black. Shaded region indicates the interval of averaged rms plus a standard deviation for the case of the whole dataset.

Another measure in order to evaluate the agreement between Lagrangian and Eulerian velocities that can be taken into account is the overall $\mathrm{U_{rms}}$ defined as:

$$\mathrm{U_{rms}} = \sqrt{\frac{1}{2N}\sum_{i=1}^{N}(u_{Eul_i} - u_{Lag_i})^2 + (v_{Eul_i} - v_{Lag_i})^2} \tag{4.32}$$

The associated average can be evaluated as follows

$$\bar{\mathrm{U}}_{\mathrm{rms}} = \sqrt{\frac{\sum_{i=1}^{N_{tot}}(N_i U_{rms_i})}{\sum_{i=1}^{N_{tot}} N_i}} \tag{4.33}$$

where N_i is the the total number of time steps of the i-th trajectory and N_{tot} is the

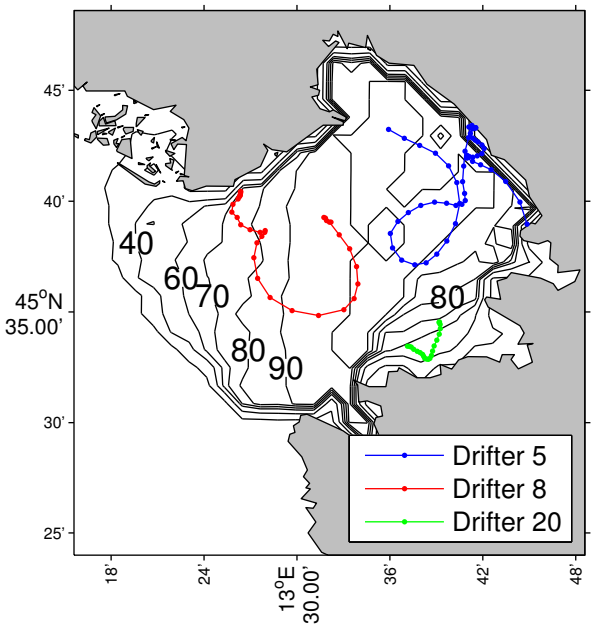

FIGURE 4.20: Trajectories of Drifter 5, 8 and 20 superimposed to the percent coverage of the velocity field data derived from HF-radar measurements.

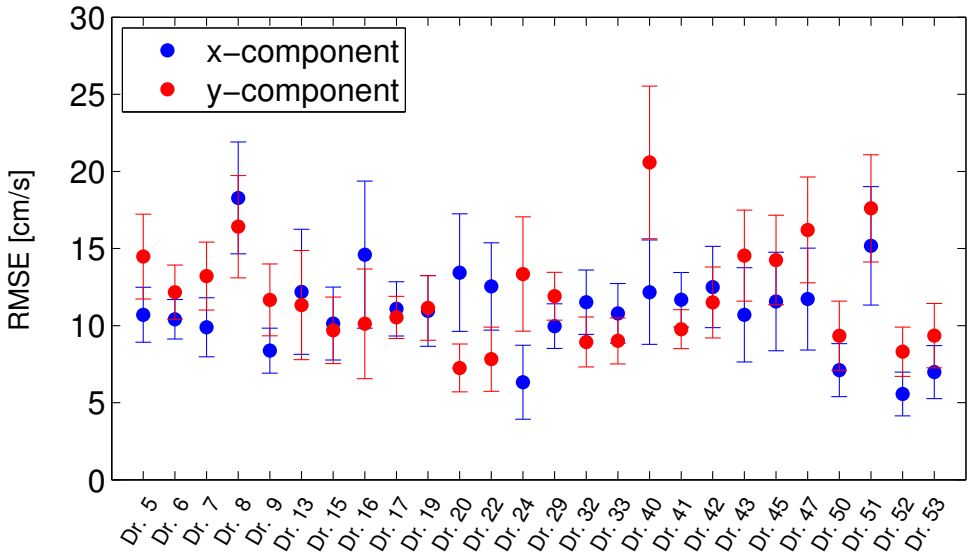

FIGURE 4.21: Distribution of the root mean square velocity components for all drifters.

number of trajectories, i.e. the number of drifters. This measure treats each trajectory considered as a time-series whose duration is double than the elapsed time of each trajectory since both u and v components are considered simultaneously. The results are presented in Figure 4.22 where the green line shows the average that is approximately 12 cm/s.

The different strengths between the average of Figure 4.19 and Figure 4.22 is due to the fact that the former takes into account the vector magnitude that tends to smooth high differences that can arouse considering the single components of the

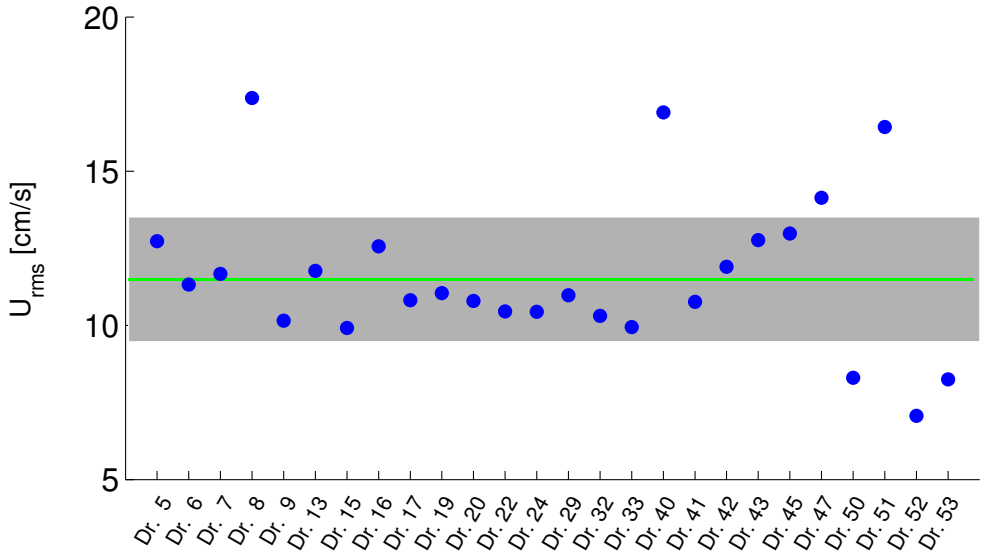

FIGURE 4.22: Overall U_{rms} for each drifter and its average (green line).

velocity. Such differences are evident if the single components of each drifter are taken into account. Figure B.1 shows such comparison for all the Drifters analysed (see Appendix).

4.4.3 Comparison between drifter trajectories and simulated trajectories based on HF-radar velocities

In this section, a direct comparison between the observed trajectories of the drifters against the numerical trajectories integrated is presented starting from the deployment positions of the drifters. The numerical trajectories have been computed solving equation (4.2).

Once the numerical trajectories of the simulated drifters have been calculated,the time behaviour of the separation $s(t)$ is tracked. This is defined as:

$$s(t) = |\boldsymbol{r}(t)_{drifter} - \boldsymbol{r}(t)_{radar}| \tag{4.34}$$

where $\boldsymbol{r}(t)_{drifter}$ and $\boldsymbol{r}(t)_{radar}$ are the vectorial positions of the observed and simulated drifters, respectively. The quantity expressed by equation (4.34) can be assumed as a measure of the accuracy of the numerical integration with respect to the observation and, thus, an indirect measure of the level of reliability of the implementation of the HF-radar velocity fields. The results obtained with the 26 drifters used for the analysis in the GoT are shown in Figure 4.23, where $s(t)$ is plotted against the lifetime of each drifter, represented by a single line. The general trend is not unexpected, indeed, an increase with time of the separation between simulations and observations has been discussed in several previous studies, see Falco et al., 2000; Molcard et al., 2009; Huhn et al., 2012 among others. However, valuable information can be gathered by inspecting Figure 4.23, for instance: the maximum separation attains values

of approximately 19 km and a remarkable increase in the separation occurs between 20 and 30 hours. This might suggests that the numerical simulation, at least following the approach described so far, should not exceed an integration time of the order of 20-30 hours. For longer times, simulated drifters follow a completly different dynamics.

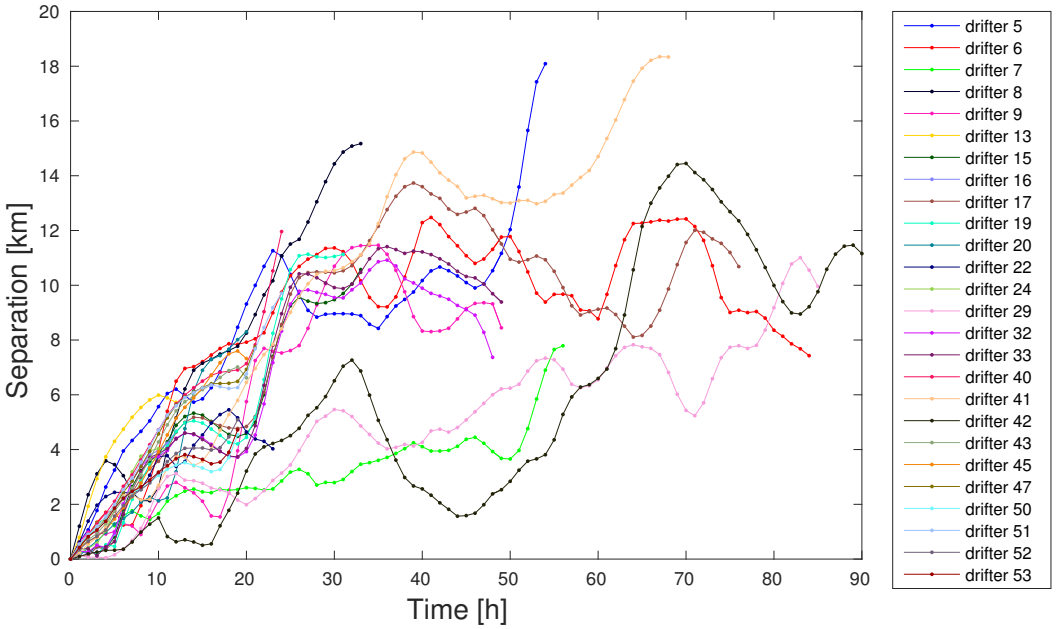

FIGURE 4.23: Separation between simulated and real drifters.

Possible explanations of this behaviour could be found in the nature of equation (4.2). In fact, the trajectory equation is strongly non linear and a small uncertainty in the initial conditions, i.e. the deployment position of the drifter, might lead to larger errors in the time prediction. Moreover, the spatial resolution of the Eulerian HF-radar velocity fields, right hand side of the equation, although it is fairly good compared to other field observations, yet it is insufficient to described the flow features at the drifter scale. Based on the above reasons, it is convenient to carry out simulations by initializing simulated trajectories at the same launch time and location as the drifters, and then re-initialize the trajectories every 12 or 24 hours at the corresponding drifter positions in order to assess the reliability of simulations upon these time windows.

To investigate the influence of the reseeding strategy, the approach discussed by Molcard et al., 2009 is followed. They used the following statistics: the mean separation distance

$$d(t) = \langle |\boldsymbol{r}(t)_{drifter} - \boldsymbol{r}(t)_{radar}| \rangle \tag{4.35}$$

and the mean displacement

$$D(t) = \langle |\boldsymbol{r}(t)_{drifter} - \boldsymbol{r}(t_0)_{drifter}| \rangle \tag{4.36}$$

where t_0 refers to the starting time of the trajectory evolution. Molcard et al., 2009 associated $D(t)$ to the prediction error assuming the drifter stays where it is deployed,

which is the case where no information is available, the so-called *no information strategy*, while $d(t)$ provides the error of the prediction based on the radar velocity field through equation (4.2). The ratio d/D provides an estimate of the reduction of the error committed in the *no information strategy* owing to the radar measurements.

As reference values for the ratio d/D, Molcard et al., 2009 reported a ratio always smaller than 1/2 (and up to 1/8) on 12-hour simulations, Ullman et al., 2006 found values of 1/2 or more on 24-hour simulations and Huhn et al., 2012 showed values in the order of 1 on 24-hour simulations in the presence of several returning points in the drifter trajectories due to a strong tidal environment. Such a typical behaviour is depicted in Figure 4.24 for drifters 6, 7 29, 33, 41 and 42. The results of Bellomo et al., 2015 who find a ratio of d/D equal to 0.63 after 12 hours for the GoT confirm the difficulties in carrying out long and reliable simulations under such conditions. Their analysis was carried out considering all CODE drifters independently of their lifetime. Here, it will be considered only those that last at least 12 hours. The results of the reseeding process every 12 or 24 hours are depicted in Figure 4.25, where the quantities d and D are shown with the corresponding errorbar (root mean square). By inspecting Figure 4.25, it is worth noting that the difference encountered in the first twelve hours of computation between the two reseedings is a symptom that the statistics suffer of the limited number of drifters. The overall 26 drifter trajectories clearly do not represent enough realizations of the local dynamic. However, the fact that d is smaller than D for almost all the time in both cases suggests that the use of HF-radar measurements reduces the error of the *no information strategy* in estimating the position, at least in a time window of a day. The chaotic process here under examination is the the dispersion of passive tracers. It is worth noting that by changing the reseeding time-window the resulting D changes.

On the contrary, the mean separation d is not much affected by the choice of the time-window for the reseeding process suggesting that such a separation is inherent to the resolution of the HF-radar velocity field. However, the fact that d is smaller than D for almost all the time in both cases suggests that the use of HF-radar measurements reduces the error of the *no information strategy* in estimating the position of passive tracers.

4.5 Concluding remarks of the Chapter

This Chapter takes into consideration Lagrangian statistics from synthetic trajectories evaluated over surface velocity fields recorded in the Gulf of Trieste. Besides, assessment of the reliability of drifter simulations is carried out by comparing velocities and trajectories of real drifters deployed in the GoT and numerical simulations.

Absolute dispersion is computed taking into account three different formulations that are commonly applied in the scientific literature. Since the presence of a mean drift can alter significantly the spread of a cloud of tracers, the results obtained in paragraph 4.2.2 are to be regarded as the most reliable. Relative dispersion and

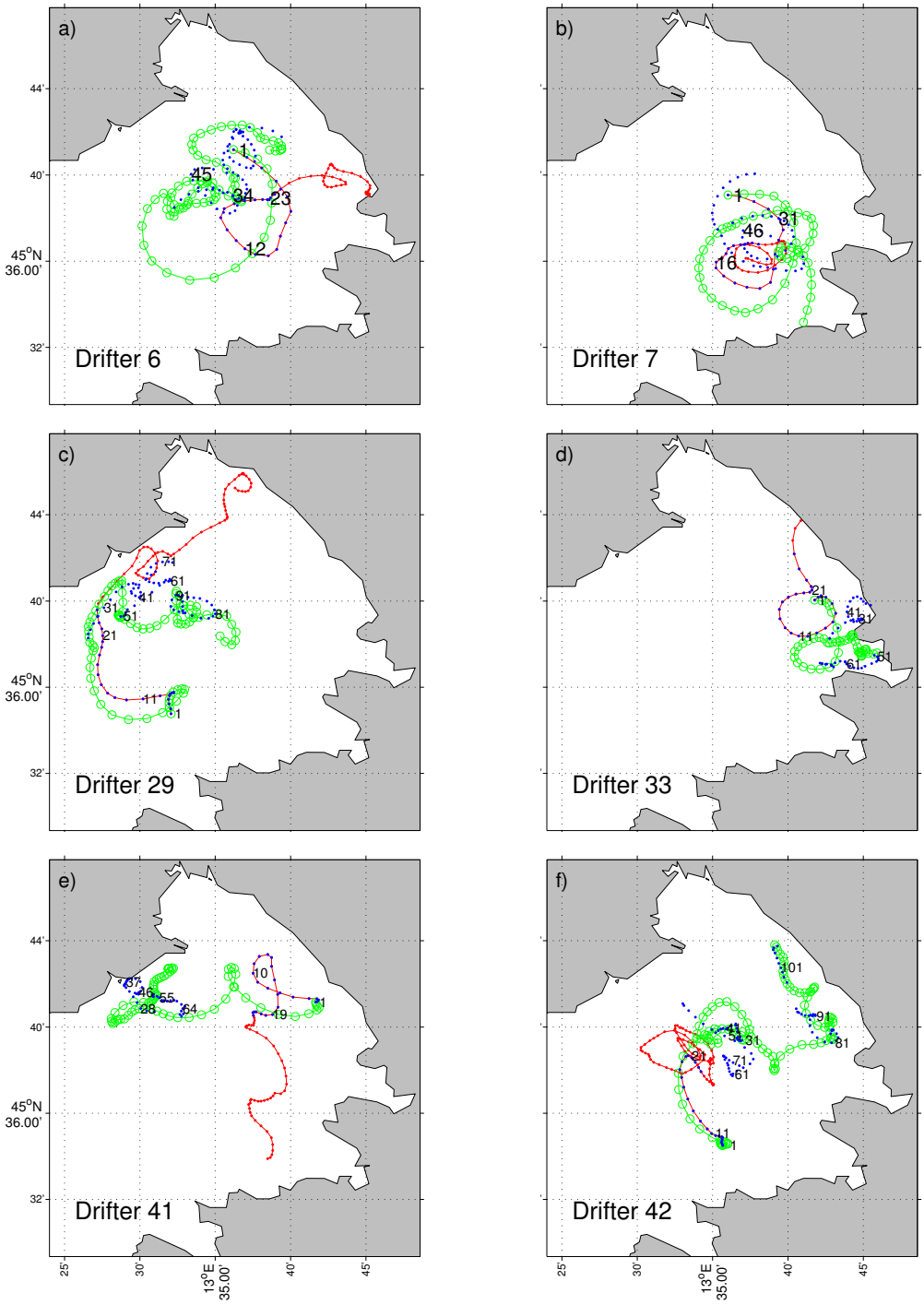

FIGURE 4.24: Trajectories of real drifters in green, simulated in red and reseeded every 24 h in blue. The numbers along the path on each map show the evolution in time (hours) of the reseed drifter (blue). The initial position $\boldsymbol{x}(t_0)$ is the same for all the drifters of the same panel.

relative diffusivity seem to recover the theoretical trends even if some caution must be taken since the exponential regime is obtained over a fit carried out over few hours. A direct comparison of these measures was needed since the evaluation of such statistics have a direct impact in the evaluation of the strength of dispersion processes. Therefore, the choice of the formulation adopted is quite relevant as this

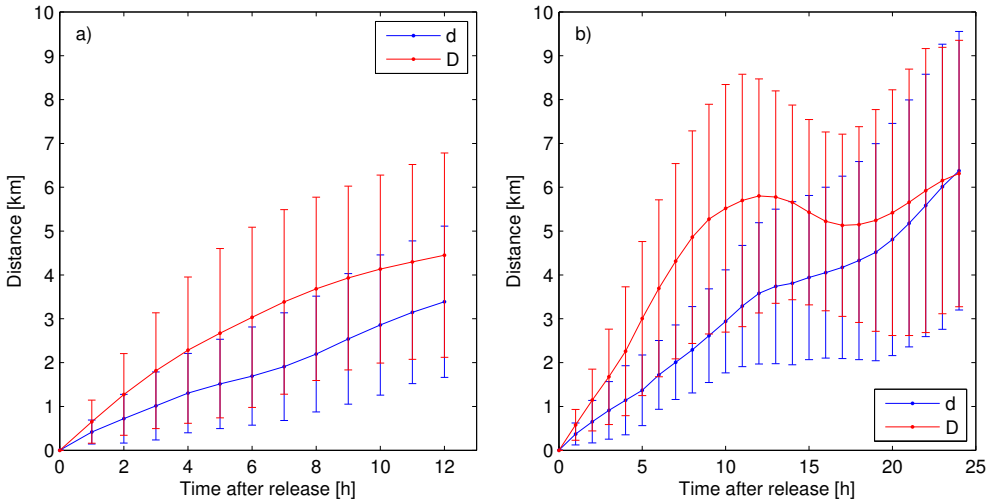

FIGURE 4.25: Separation distance $d(t)$ and mean displacement $D(t)$ for the reseeding process of 12 hours, panel a), and 24 hours, panel b).

study demonstrates. A careful choice of the formulation must take into consideration the existence of a possible mean drift that can have a strong effect on dispersion processes. Should this be the case, such dispersion generated by the mean drift must be neglected. Besides, the evaluation of absolute and relative dispersion has an important role in the description of pollutant transport through the Eulerian approach, i.e. the advection-diffusion equation written in terms of a mean velocity following Reynolds decomposition. Such an equation relies on a dispersion coefficient whose estimation comes from the analysis carried out in this chapter (Fischer et al., 1979).

Assessment of the reliability of drifter simulations is carried out firstly by comparing Eulerian velocity of the measured field and Lagrangian velocity of the real drifters. Secondly, by comparing real drifter trajectories and numerical trajectories. Both cases give as a result values that are in agreement with the errors commonly accepted in literature even if the fairly limited number of drifters available leads to results affected by a quite large standard deviation as far as trajectory comparisons are taken into account.

Chapter 5

Lagrangian Coherent Structures in the Gulf of Trieste

This Chapter takes into account the inhomogeneity of the flow inside the GoT, whereas the previous Chapter was devoted to a detailed account of Lagrangian statistics and comparisons of drifter simulations and trajectories. Chapters 1 and 2 accurately described the importance of such inhomogeneity that gives rise to Lagrangian Structures. Here, the concepts introduced in Chapter 2 are applied to the dataset of the GoT. The theory behind Lagrangian structures was already detailed formerly. However, some aspects were disregarded and will be introduced whenever needed in the following. In order to distinguish between ridges of FTLE fields and tensorlines, the former will be referred as heuristic LCS whereas the latter as rigorous LCS.

Lagrangian barriers can be divided into two broad classes: repelling, calculated in forward time, and attracting, calculated in backward time. Equation (4.2) can be solved in forward time, i.e. from the start time t_0 to the end of the time interval, to locate repelling structures and in reverse time, i.e. from the end of the time interval to the start t_0, to detect attracting structures (Shadden, Lekien, and Marsden, 2005; Hernández-Carrasco et al., 2011; Huhn et al., 2012; Allshouse and Peacock, 2015a). These structures can be viewed as finite-time stable and unstable manifolds locating, respectively, regions of expansion and contraction of fluid particles.

The implementations of FTLEs and FSLEs are usually distinct and their contemporaneous application is scarce. Only few exceptions can be found in literature providing somewhat contrasting indications (Karrasch and Haller, 2013). Boffetta et al., 2001 show that FTLEs are limited to small-scale properties of dispersion while FSLEs are the most efficient method for detecting large-scale cross-stream barriers. On the contrary, FTLEs have been shown to better capture recirculation regions than FSLEs in a water turbine (Sadlo and Peikert, 2007). In a recent paper, Peikert et al., 2014 show that, if properly calibrated by similarity measures, both FTLEs and FSLEs may

produce comparable results which can be interchangeably used for most purposes in flow visualizations. The comparison of both FTLE and FSLE techniques and their contemporaneous application may thus benefit from further investigations, especially in turbulent realistic scenarios characterized by high Reynolds numbers, Re.

Oceanic coastal circulations may represent a challenging task along this direction. For coastal characteristic velocity scales of $U \sim 10^{-1}$ m/s, length scales of $L \sim 10^{3}$ m and viscosity of $\nu = 10^{-6}$ m^2/s, Reynolds numbers as high as $Re = UL/\nu \sim 10^{8}$ may be achieved. Nevertheless, Lyapunov-exponent-based tools are widely used in coastal oceanography to predict the spreading of pollutants and biological quantities (Lekien et al., 2005; Peng and Dabiri, 2009; Shadden et al., 2009). Their correct application requires full knowledge of the oceanic velocity field. This requirement is only partially fulfilled when either satellite altimeter data (Harrison and Glatzmaier, 2012), numerical models (Haza et al., 2007; Haza et al., 2008), or coastal observations (Haza et al., 2010; Berta et al., 2014) are employed. All these datasets present different spatial resolutions that, given the turbulent nature of the flow and the high Reynolds numbers achieved, may not resolve all the important scales for the motion and cause significant uncertainties.

Regarding the LCS detection and application the aim is to detect both heuristic LCSs, through FTLEs, FSLEs and LCSs, applying the geodesic theory of transport barriers (Haller and Beron-Vera, 2012). Besides, it is intended to assess whether, starting from the same high Reynolds number turbulent fields, FTLE and FSLE techniques lead to similar heuristic LCSs and how accurately the latter compare with drifter observations in a Mediterranean small scale area. Moreover, the aim is to test the robustness of these Lagrangian analysis when applied to HF-radar fields. In fact, quite often the HF-radar velocity fields show several spatial gaps, mostly owing to signal problems, and the objective is to show that FTLE-FSLE-LCS based methods are less sensitive to these data gaps with respect to standard Lagrangian approaches, e.g. absolute dispersion. The importance of this aspect could easily be appreciated having in mind the possible application of risk monitoring and Search and Rescue (SaR) operations based on HF-radar information.

5.1 Parameters choice for FTLE and FSLE fields detection

A key parameter in order to highlight Lagrangian barriers in FTLE fields is the integration time T. In analogous coastal application, Shadden, Lekien, and Marsden, 2005; Shadden et al., 2009 and Huhn et al., 2012 used integration times with an order of magnitude of hours. In the present study, a sensitivity analysis depending on the integration time is performed, which has been changed in a range between five and fifty hours.

Figure 5.1 shows different FTLE fields evaluated at the increase of the integration time T. As T increases the ridges, i.e. the Lagrangian structures, clearly emerge. Integration times tending to either zero or infinity lead to, respectively, fields dominated

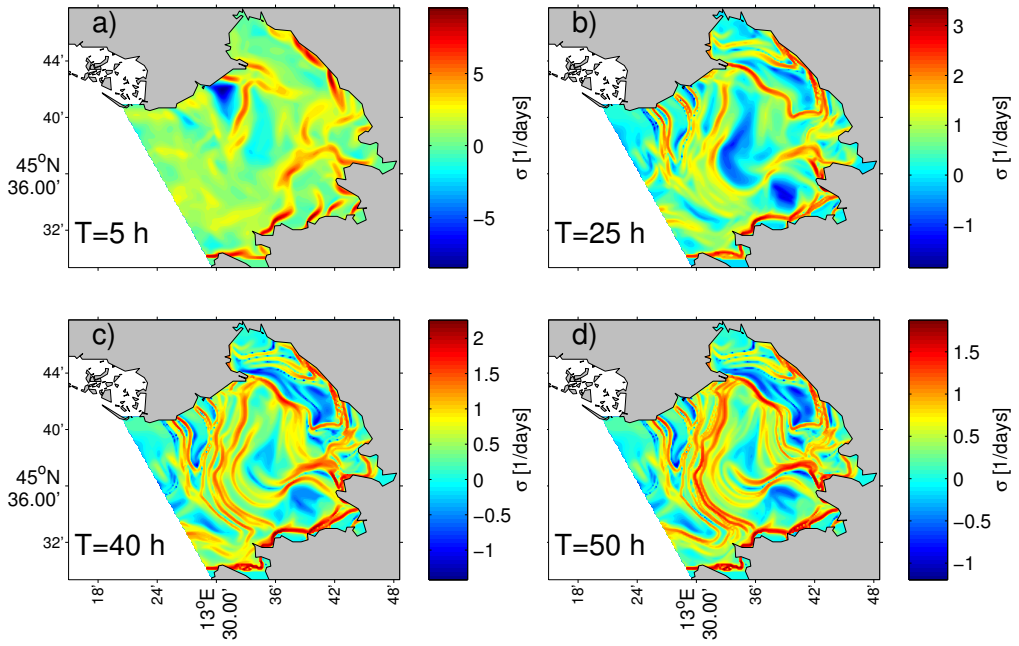

FIGURE 5.1: FTLE fields at the increase of the integration time T.

by local strain without fully developed barriers on the domain (Panel a) of Figure 5.1) or uniform fields (Panel d) of Figure 5.1). This behaviour has been investigated by (Abraham and Bowen, 2002) computing the mean value of the Lyapunov coefficient and their standard deviation depending on the integration time. These statistics tend to decrease as the integration time increases. Based on this observation, a value of 25 hours is adopted. This is high enough to let Lagrangian structures appear clearly and showing the highest correlation with analogous FSLE fields, as described in the next Section. In addition, since in Section 5.2 simulations of drifters with a 24 h reseeding will be performed, such a choice of the integration time allows to look for FTLE fields whose information is evaluated on the same time scale of the reseeding process.

In analogy to the computations of FTLE fields, it is possible to evaluate different FSLE fields varying the initial separation δ_0 and the target final separation δ_f. Haza et al., 2008 suggested that the minimum ratio between final and initial separation $\alpha = \delta_f/\delta_0$ must be chosen so that the time required for particle pairs to separate from δ_0 to δ_f is longer than the time resolution Δt of the velocity dataset, equal to 1 hour in the present case study. In order to ensure such a condition a value of $\alpha = 7$, as already used by Haza et al., 2008, is adopted. Figure 5.2 shows FSLE fields at the varying of the ratio α. White regions represent areas where particles do not reach the expected maximum separation because they recirculate confined in such white sub-domains.

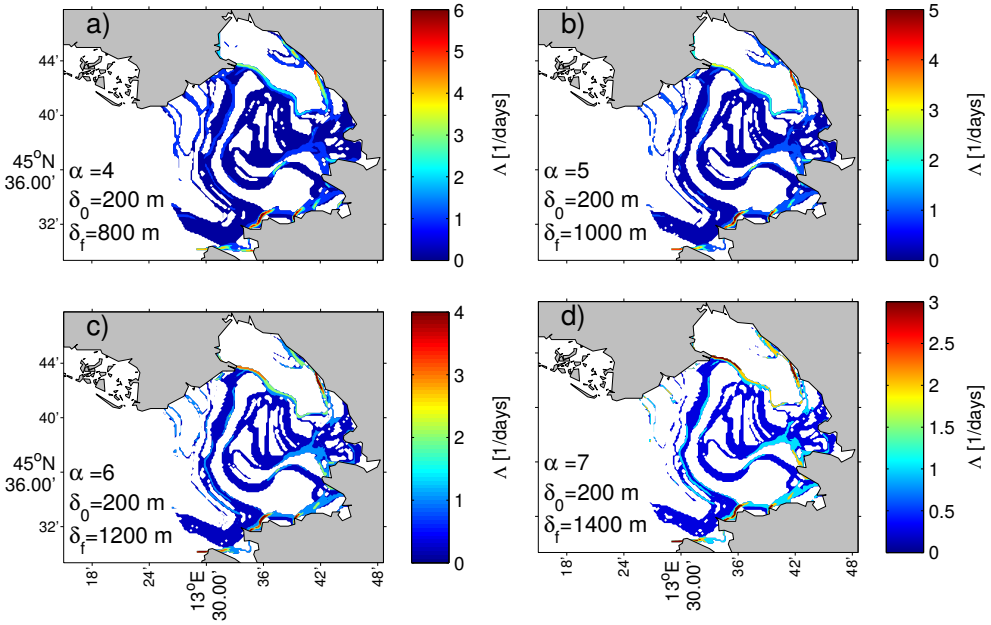

FIGURE 5.2: FSLE fields calculated with $\delta_0 = 200$ m and $\delta_f = 800$, 1000, 1200 and 1400 m.

5.1.1 FTLE and FSLE comparisons

Following Peikert et al., 2014, a comparison between FTLE and FSLE maps is carried out by calculating their correlation coefficient. FTLE and FSLE fields adopted for the analysis are obtained by seeding of an initial grid with a regular spacing of 200 m. The resulting FSLE fields might present some gaps, where the computed separation does not reach the target separation δ_f. Hence, the correlation coefficient evaluation is carried out taking into account only the corresponding values of FTLE fields to actual values of FSLE fields, while FTLE regions where FSLEs are not defined are disregarded by this analysis.

The correlation coefficient is defined as

$$\text{corr}(f,g) = \frac{\text{cov}(f,g)}{\sqrt{\text{var}(f)\ \text{var}(g)}} \tag{5.1}$$

where f and g are the FSLE/FTLE fields and its results are reported in Table 5.1 as a function of integration time T and final separation δ_f.

The present results shows that the correlation coefficient reaches values higher than 0.8 for integration time greater or equal to about a day, i.e. 25 hours, regardless the final separation. Moreover, the combination of $T = 25$ h and $\delta_f = 1400$m presents the highest value, i.e. around 0.88. The maximum reached for the integration time of about a day it is probably related to the correlation time scale typical in coastal regions, which has been often estimated in 24 hours (Bauer, Swenson, and Griffa, 2002). This time frame of 25 hours will also be used in the next sections where the detected LCSs will be discussed in details.

High correlation occurs when the integration time T is chosen in agreement with

δ_f / T	800 m α=4	1000 m α=5	1200 m α=6	1400 m α=7
5 h	0.6596	0.7813	0.7742	0.7657
25 h	0.8240	0.8695	0.8776	0.8790
40 h	0.8074	0.8450	0.8570	0.8645
50 h	0.8047	0.8368	0.8511	0.8608

TABLE 5.1: Correlation coefficient between FTLE and FSLE fields calculated for different values of the integration time T and of the final separation δ_f. The highest correlation is highlighted.

the final separation δ_f, i.e. when the integration time is small, the highest correlation occurs with small δ_f and vice-versa. This is due to the fact that in order to reach a certain fixed separation δ_f in FSLE fields, a related integration time T is needed for FTLE fields.

As far as FTLE fields are considered, the trend of mean and standard deviation forecast by equations 3.14 and 3.15 at the increase of the integration time is shown in Figure 6.7. The oscillating behaviour of the curves obtained at the varying of the initial conditions (grey ones) could be due to the tidal signal. With increasing

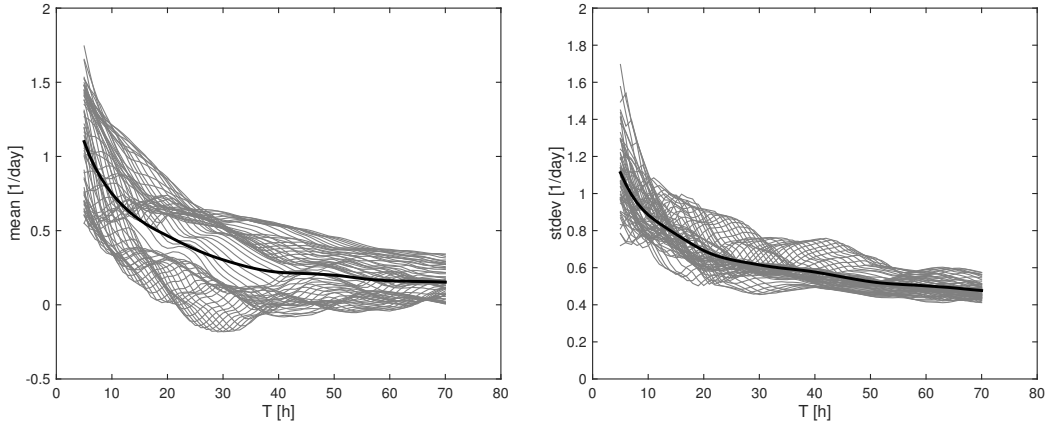

FIGURE 5.3: Trend of mean and standard deviation of FTLE values. Grey lines are evaluated for different initial conditions, whereas the black line is the average of the grey ones.

T the standard deviation of FTLE values decreases as well as the mean. For closed ergodic flows all Lyapunov exponents converge to the same value the variance vanishes, however, the flow in the GoT is an open flow and the infinite time limit is thus only hypothetical. These Figure were obtained by filling the interior of the GoT with particles but staying away form the influence of the boundaries.

5.2 Heuristic LCSs detection vs drifter observations

Robustness of Lagrangian structures detected by Lyapunov-exponent diagnostic tools to velocity errors and scaling is well-known (Haller, 2002; Hernández-Carrasco et al.,

2011). Such a property allows the joint analysis of Lagrangian structures and drifter trajectories despite the coarseness of velocity fields and the presence of missing data.

Shadden et al., 2009 and Huhn et al., 2012 already showed that drifter trajectories are tied to Lagrangian structures. Furthermore, Prants, 2015 reviewed the applicability of Lagrangian structures computed in backward-time to study several transport problems in the ocean. Comparisons of drifter trajectories with attracting heuristic LCSs computed in backward-time are here carried out with the same aim.

Evaluation of the most influential heuristic LCSs in FTLE fields, i.e. ridges, is pursued considering the dynamical properties of these features (Mathur et al., 2007; Green, Rowley, and Haller, 2007). Ridges behave as attractors of trajectories solution of the dynamical system

$$\frac{d\boldsymbol{x}}{ds} = \nabla \sigma_{t_0}^{t_0 \pm T}(\boldsymbol{x}) \tag{5.2}$$

where s is the arclength along the gradient lines of $\sigma_{t_0}^{t_0 \pm T}(\boldsymbol{x})$ and the right-hand side represents the spatial gradient of FTLE scalar fields. This property is at the base of the extraction algorithm proposed by Mathur et al., 2007 and here adopted.

The analysis is started focusing the attention on three reseeding time-windows of Drifters 6, 29 and 42. For the sake of clarity, the same colour coding will be adopted in all Figures of this section, namely observed drifters position will be coloured in green, simulated drifters without reseeding in red and simulated drifters with reseeding in blue. Then, the objective is to compare the prediction of the drifters position that can be performed using both the heuristic LCSs and a more traditional approach based on the simple computation of a single trajectory, which should represent the path of the drifter. At the end of this section, an overall comparison among the above predictions will be presented for the entire data sets.

Figure 5.4 shows four snapshots of the trajectory of Drifter 6 superimposed to FTLE backward fields (attracting heuristic LCSs). Panel a) refers to the second time-step of the reseeding time-window and shows that the simulated drifter without reseeding has already headed towards the eastern part of the GoT, see red dot, separating from the real drifter. On the contrary, the observed and the simulated trajectories with reseeding are tied to the structures present at the center of the GoT in all four Panels.

Moving to the analysis of Drifter 29, see Figure 5.5, it is interesting to note that the deployment of the drifter occurs in a position initially quite distant from any relevant attracting heuristic LCSs, see Figure 5.5 panel a). However, as time elapses the drifter tends to move towards the closest attracting structure. Moreover, even in this case, the simulated drifter without reseeding significantly separates from the observed one. However, the reseeded drifter and the simulated one show different dynamics. The real one tends to move towards the center of the GoT, whereas the reseeded drifter is confined in the north-western part of the GoT. In order to understand the reasons behind this difference, forward FTLE fields, i.e. repelling structures, are analysed.

Panels a) to d) of Figure 5.6 are the corresponding forward FTLE fields of the backward FTLE fields of panels a) to d) of Figure 5.5. Panel a) of Figure 5.6 shows that observed and reseeded drifters are in the proximity of a repelling structure at the beginning of the reseeding time-window. In the following time steps a small separation between the two trajectories will result afterwards in greater separation: observed and simulated drifters are divided by such structure during the whole time-window under consideration. This justifies the greater separation observed for Drifter 29 compared to Drifter 6. It is also possible to argue that sensitivity to initial conditions and unresolved subgrid dynamics play a role that is not modelled integrating equation 4.2 on the base of the velocity fields at our disposal.

Drifter 6 - attracting structures

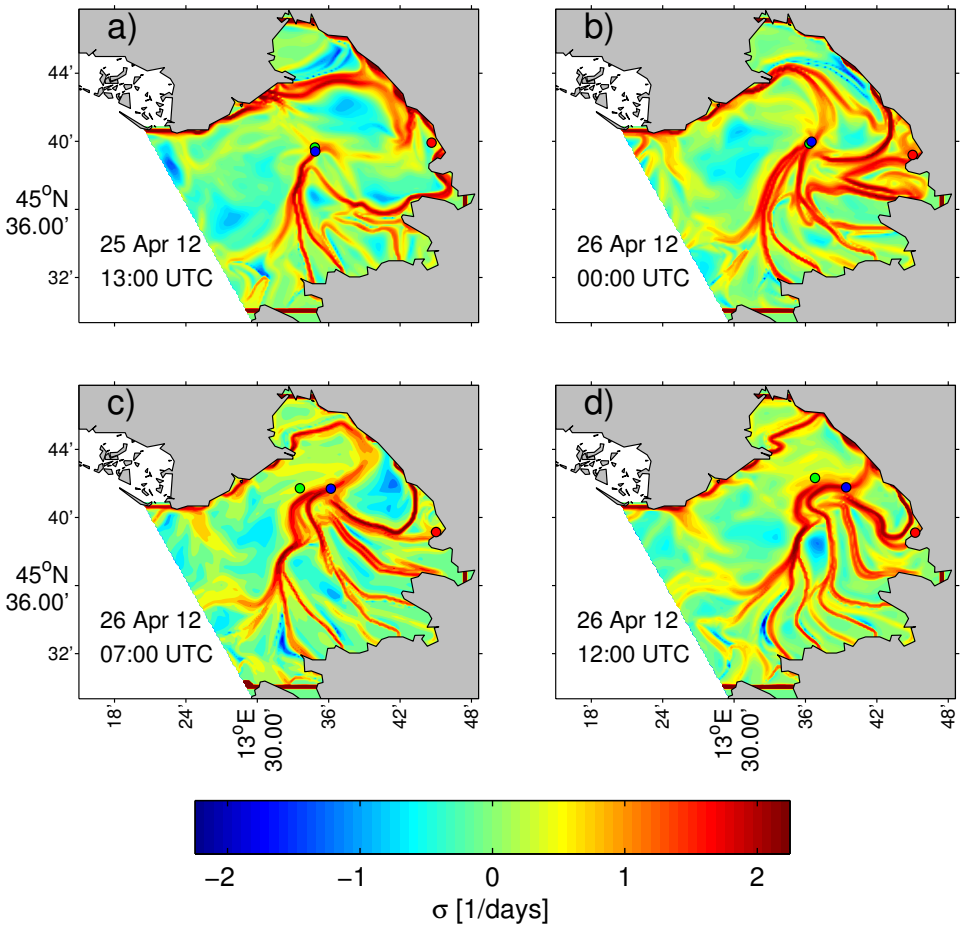

FIGURE 5.4: Drifter 6 and backward FTLE fields (attracting structures) for 25^{th} April 2012 13:00 UTC, Panel a), 26^{th} April 2012 00:00, 07:00 and 12:00 UTC, Panel b), c) and d), respectively. Green drifter: field surveyed during TOSCA campaign; red drifter: numerical simulated without reseeding; blue drifter: numerical simulated with reseeding every 24 hours.

Considering Drifter 42, Figure 5.7 shows the superposition of trajectories of Drifter 42 on backward-time FTLE fields, i.e. attracting structures. The results reveal that the observed drifter and the simulated ones move along local maxima of FTLE fields

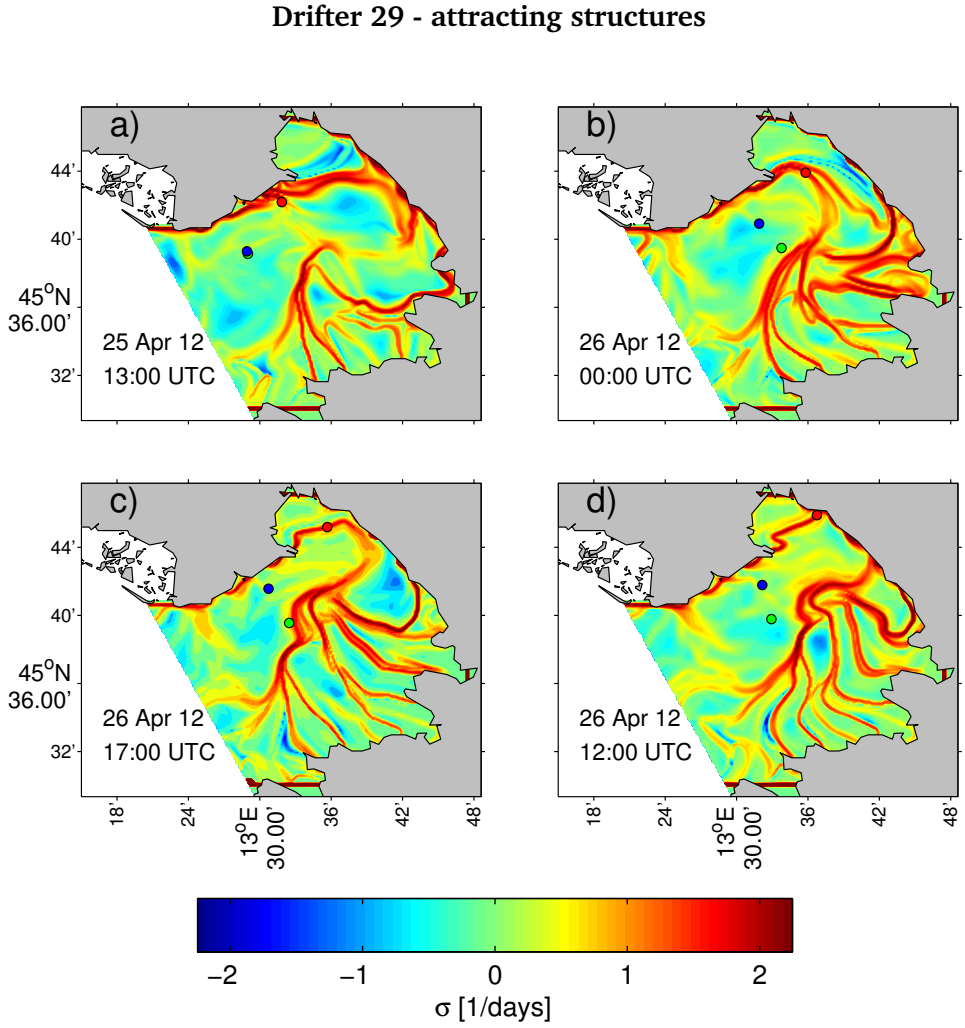

FIGURE 5.5: Drifter 29 and backward FTLE (attracting structures) fields for 25^{th} April 2012 13:00 UTC, Panel a), 26^{th} April 2012 00:00, 07:00 and 12:00 UTC, Panel b), c) and d), respectively. Green drifter: field surveyed during TOSCA campaign; red drifter: numerical simulated without reseeding; blue drifter: numerical simulated with reseeding every 24 hours.

and head to the opposite sides of the GoT (the real drifter heads towards west, the simulated one heads toward the eastern side and the reseeded simulated stays at the center of the GoT). Such local maxima belong to ridges of FTLE fields detected in agreement with Mathur et al., 2007.

Figure 5.8 shows such ridges detected on the FTLE field of Panel a) of Figure 5.7. In particular, the simulated drifter without reseeding is bound to a structure identified as ST1, while the observed and the reseeded simulated are attracted by a structure identified as ST2. The structure ST2 develops from a prevailing north-west to south-east direction to a prevailing east to west direction. Analogously to the case of Drifter 29, subgrid dynamics influences the path of the drifter and FTLEs prove to be able to capture direction along which transport develops.

Two types of distances are computed. Firstly, between the observed position of

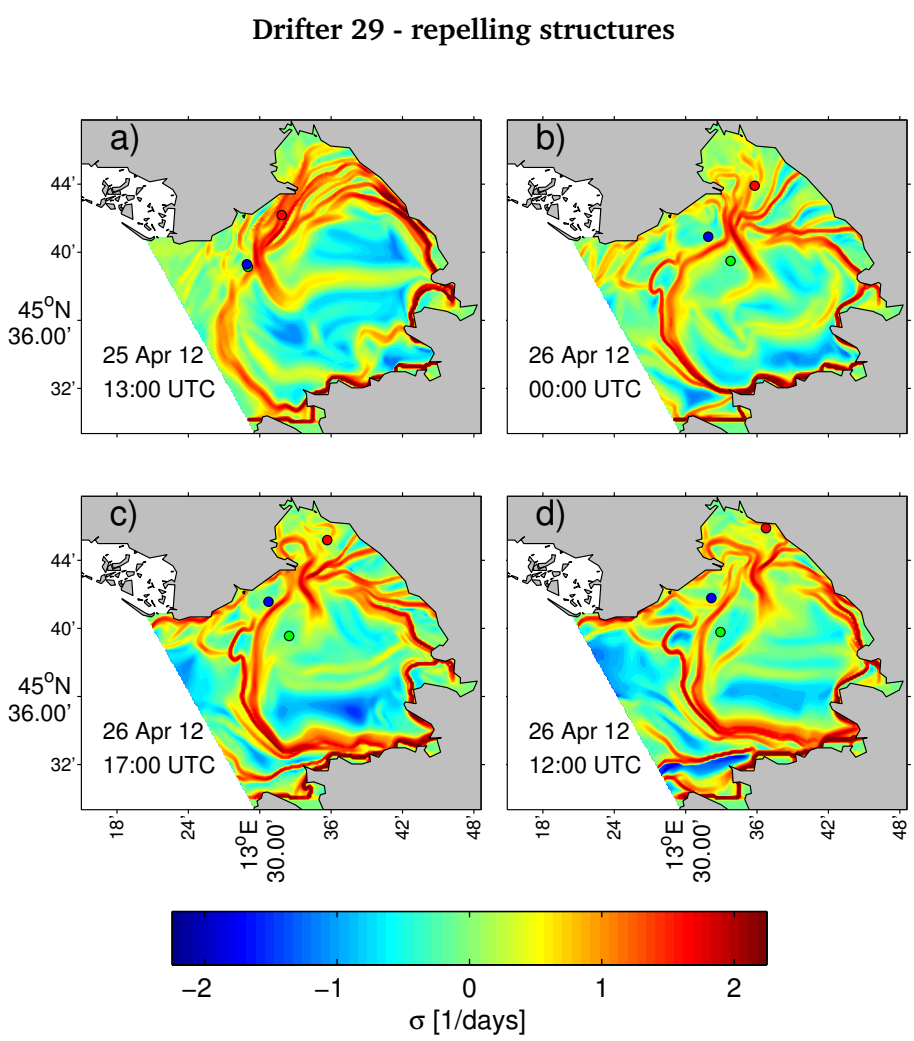

FIGURE 5.6: Drifter 29 and forward FTLE fields (repelling structures) for 25^{th} April 2012 13:00 UTC, Panel a), and 26^{th} April 2012 00:00 UTC, Panel b). Green drifter: field surveyed during TOSCA campaign; red drifter: numerical simulated without reseeding; blue drifter: numerical simulated with reseeding every 24 hours.

the drifter and the numerical trajectories and, secondly, between the observed position of the drifter and the attracting heuristic LCSs for a time interval of 24 hours for the three drifters discussed above. The resulting distances are reported in Figure 5.9. The ridges taken into account are those at the center of the GoT for Drifter 6 and 29, whereas for Drifter 42 the ridge ST2 is considered. The separation between observed and reseeded drifters tends to increase in time from zero to several kilometers (dotted lines in Figure 5.9). On the contrary, the initial separation between attracting structures and drifters can be significant at the beginning of the time-window and decreases as the trajectory evolves, owing to the attracting nature of the LCSs, see for instance Drifter 29. In all cases analyzed, at the end of the time-window, separations between observations and simulated drifters is greater than distances between drifters and ridges (below 2.5 km). Repeating this procedure with the entire drifters data sets, we finally obtain the results shown in Figure 5.10, where the same

quantities have been calculated for each drifter for the same 24 hours time frame. On average, the distance of real drifters from the nearest FTLE-backward-ridge is 1.42 ± 1.05 km whilst the separation between observations and reseeded simulated drifters is on average 7.80 ± 2.87 km, thus, more than five times larger.

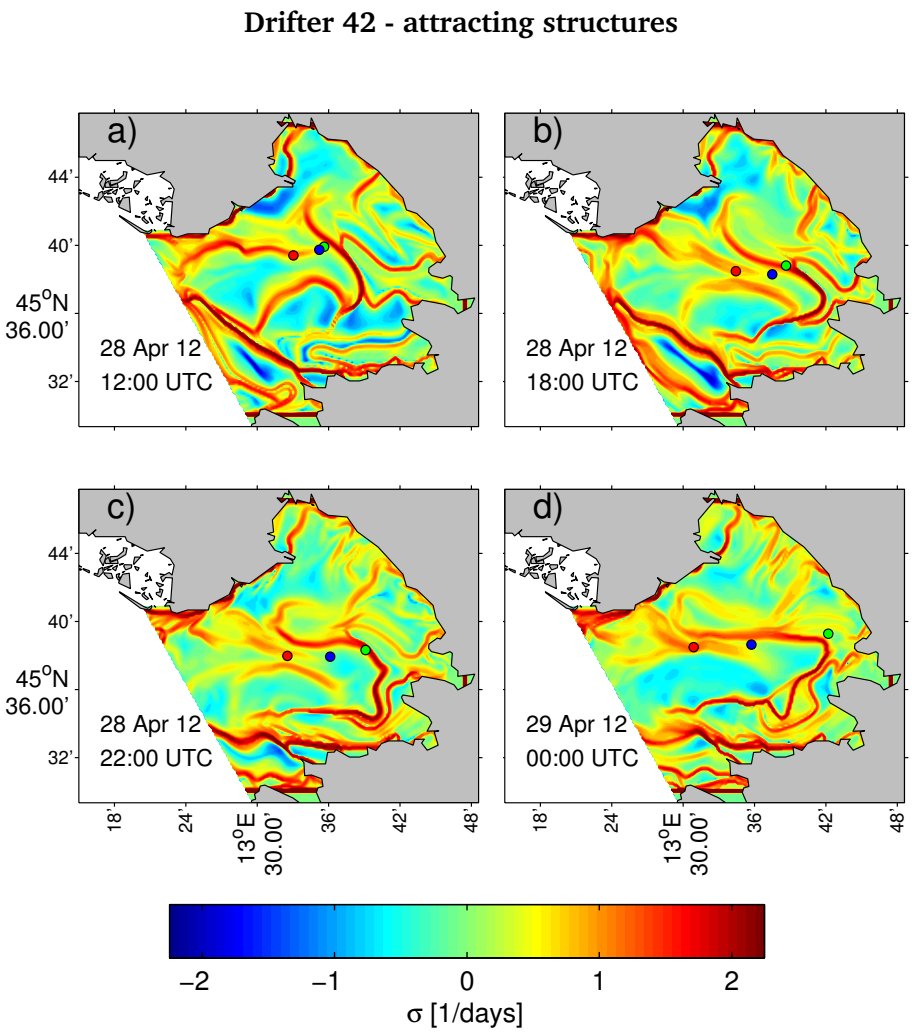

FIGURE 5.7: Drifter 42 and backward FTLE fields (attracting structures) for 28^{th} April 2012 12:00, 18:00 and 22:00 UTC, Panel a), b) and c), 29^{th} April 2012 00:00, 03:00 and 05:00 UTC, Panel d), e) and f), respectively. Green drifter: field surveyed during TOSCA campaign; red drifter: numerical simulated without reseeding; blue drifter: numerical simulated with reseeding every 24 hours.

It could be useful to illustrate the consequences of the above considerations through an idealized example. Imagine to carry out a SaR operation in the sea having at your disposal the position where the accident occurred and velocity fields provided by measurements or validated numerical models. Detection of Lagrangian structures could contribute to the established methods based on trajectory computations (Jordi et al., 2006; Breivik and Allen, 2008). Lagrangian structures could highlight preferred directions along which search operations should be carried out. Several Authors, see among others Ullman et al., 2006, Molcard et al., 2009 and Bellomo et al., 2015, suggest the use of single particle trajectories, based on radar velocities, as the simplest

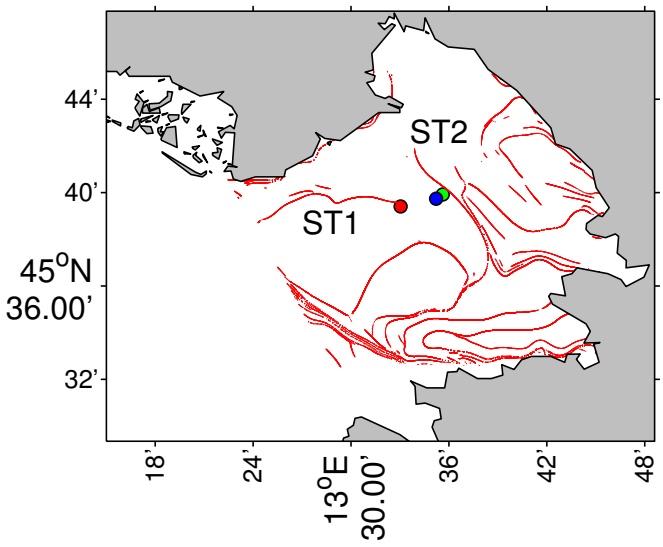

FIGURE 5.8: Drifter 42 and backward FTLE ridges (attracting structures) for 28^{th} April 2012 12:00 UTC. Green drifter: field surveyed during TOSCA campaign; red drifter: numerical simulated without reseeding; blue drifter: numerical simulated with reseeding every 24 hours.

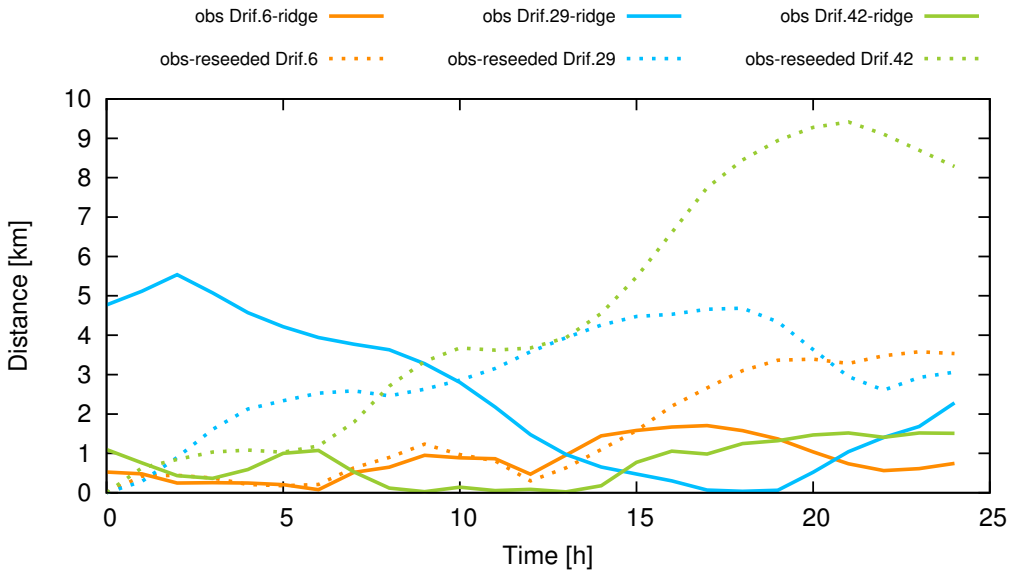

FIGURE 5.9: Distances of real and reseeded drifters from backward FTLE ridges and between themselves.

predictive strategy for operational application such as SaR. It is intend to compare the accuracy of the above method against the employment of the LCSs instead of the single particle computation. Indeed, Molcard et al., 2009 carried out an extensive comparison between real drifters trajectories and reseeded drifters and their applicability for operational purposes. In order to quantify the reliability of drifter trajectory predictions, they evaluated the mean separation distance $d(t)$ and the mean displacement $D(t)$. They associated $D(t)$ to the prediction error assuming the drifter stays

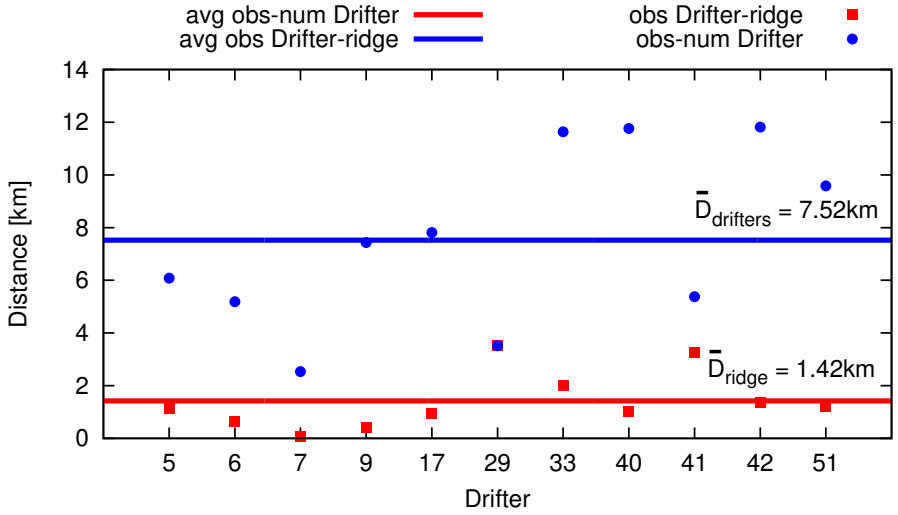

FIGURE 5.10: Summary of the computed differences bewteen the simulated drifters and the corresponding observed position (blue dots), the differences between the observed drifters positions and the attracting LCSs (red dots) and, finally, the corresponding averaged values.

where it is deployed, which is the case where no information is available ("no information strategy"), while $d(t)$ indicates the error of the prediction based on the radar velocity field. These quantities were already presented in Section 4.4.3 and are here recalled in order to carry out a comparison with LCS. The ratio d/D or its inverse defined in Bellomo et al., 2015 as search range reduction factor (SRRF), provides an estimate of the reduction of the error committed in the "no information strategy" due to the radar measurements. Estimates of the above ratio for integration intervals of 24 hours are presented in Ullman et al., 2006 and Molcard et al., 2009 and the resulting values are of the order of $1/2$ or greater. Moreover, Bellomo et al., 2015 evaluated these quantities for different sites interested by the TOSCA project obtaining a ratio always smaller than the unity over time windows of 12 or 24 hours. In particular, for the Gulf of Trieste, they computed the SRRF for a time interval of 12 hours obtaining a value of about 1.6, which implies a value of the ratio d/D close to 0.6. Moving to the results obtained from the analysis of the LCSs and their distance to the observed drifters positions, see Figure 5.10, it is possible to compute the ratio $d(t)/D(t)$ or its inverse, i.e. the SRRF factor, substituting the distance $d(t)$ obtained from single particle trajectories with the distance to the heuristic LCSs after a time interval of 24 hours. The values obtained for $d(t)/D(t)$ ranges from a minimum of 0.03 to a maximum of 0.51 with an averaged value of 0.17. The corresponding values of the SRRF factor as defined by Bellomo et al., 2015 are 1.96, 36 and 10.5, respectively. The value computed by Bellomo et al., 2015 and reported in the paper is much less and, furthermore, evaluated on a time interval of 12 hours. Note also that in several cases, the employment of the single particle strategy leads to values of the ratio $d(t)/D(t)$ bigger than unity, implying that this prediction is not helpful during a SaR operation, while in the case of heuristic LCSs for all tested drifters values much smaller than one

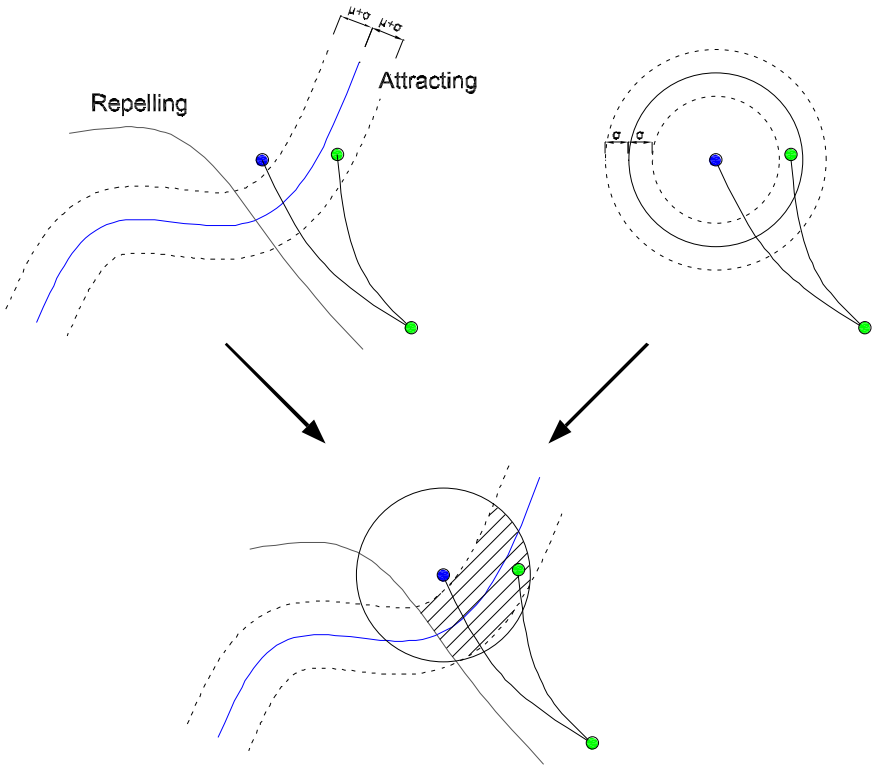

FIGURE 5.11: Sketch of LCSs and observed drifter mutual positions, on the left, and of single-particle simulation, on the right. μ represents the average distance while σ the standard deviation. If a single-particle simulation is carried out, the observed drifter and the reseeded drifter tend to have divergent trajectories as time elapses. Therefore, a search operation based on such a simulation should be carried on concentric circles centred on the reseeded drifter, while LCSs give preferential direction along which the search operation can be carried out. Joining these two approaches leads to the evaluation of the area over which SaR operations should be carried out. This area (shaded in the sketch) is the result of the superposition of the circle and of the surrounding strip around attracting LCSs.

are obtained.

Finally, the results suggest that these two approaches should be carried out jointly in order to better assess the approximated position of the target of SaR operations. Figure 5.11 represents a simple sketch of the searching strategy that is possible to adopt. By locating repelling and attracting structures, it is possible to focus SaR operations along a narrow strip surrounding the attracting heuristic LCS. However, in order to define how elongated this area should be it is possible to join the heuristic LCS analysis to the single-particle tracking procedure. If a single-particle predictive strategy is carried out, the search for the passive object should extend on circles whose maximum radius has an order of magnitude of the average distance plus the standard deviation. By joining these two approaches, the area where the SaR operations are to be carried out is the shaded area represented at the bottom of Figure 5.11 consisting in the superposition of the elongated strip around the heuristic LCS and the circle. In the next Section this idea is applied considering LCS evaluated from Cauchy-Green tensorlines.

5.3 Detection of Lagrangian Coherent Structures

Motivated by the good agreement between drifters and heuristic LCSs reported in the previous Section, an analysis based on rigorous LCSs is carried out. The same procedure described by Olascoaga et al., 2013 is adopted. Tensorlines of the Cauchy-Green tensor, i.e. curves tangent to its eigenvectors, are evaluated. Let $\boldsymbol{e_1}$ and $\boldsymbol{e_2}$ be the eigenvectors of the Cauchy-Green tensor associated with the minimum and maximum eigeinvalues ($0 < \lambda_1 \leq \lambda_2$), respectively, and $\boldsymbol{e_1} \perp \boldsymbol{e_2}$. The Cauchy-Green tensor is evaluated on the fixed time interval $[t_0, t_0 + T]$ with a forward integration. Shrinklines (or squeezlines) at time t_0 are identified as trajectories of

$$\boldsymbol{r'} = \boldsymbol{e_1} \tag{5.3}$$

Stretchlines at time t_0 are identified as trajectories of

$$\boldsymbol{r'} = \boldsymbol{e_2} \tag{5.4}$$

In order to locate the most repelling and attracting LCSs at the time t_0, the ones that exhibit the highest repulsion and attraction, respectively, are retained. The normal growth to a material line of a unit normal vector is given by the repulsion rate $\rho_{t_0}^{t_0+T}$ (Haller, 2011). Squeezlines and stretchlines present a repulsion rate $\rho_{t_0}^{t_0+T} = \sqrt{\lambda_2(x)}$ and $\rho_{t_0}^{t_0+T} = \sqrt{\lambda_1(x)}$, respectively. The most prominent attracting and repelling LCSs are chosen as those that on average show the maximum repulsion and attraction along their length. Let the curve γ be a LCS, the average is computed as (Haller and Beron-Vera, 2012; Farazmand and Haller, 2013)

$$\langle \rho_{t_0}^{t_0+T} \rangle = \frac{\int_\gamma \rho_{t_0}^{t_0+T} |r'(s)| ds}{\int_\gamma |r'(s)| ds} \tag{5.5}$$

In order to locate repelling and attracting LCSs at any time $t \in [t_0, t_0 + T]$ in forward time, the LCSs detected at time t_0 are advected.

Comparison of LCSs with Drifter 42 is illuminating. In the neighbour of the deployment location of Drifter 42 the most repelling and attracting LCSs are sought and the latter is advected in forward time. The procedure is repeated for every reseeding time-window. Besides, the operational procedure depicted in Figure 5.11 is applied. These results are plotted in Figure 5.12 (cf. with Figure 5.7) where four snapshots of the evolution of the drifter trajectories (observed and simulated) alongside with LCSs are shown. In particular, a circle of radius 7.52km (the average distance between observed and reseeded drifter after 24h, cf. Figure 5.10) is centred at the reseeded drifter position and represents the searching area due to a single-particle approach. Panel a) of Figure 5.12 shows blue and black curves representing attracting and repelling LCSs, respectively. The black point represent the intersection between LCSs, i.e. a hyperbolic point. The black dashed curves represent the searching areas alongside the attracting LCSs in analogy to Figure 5.11. The scalar field underneath is

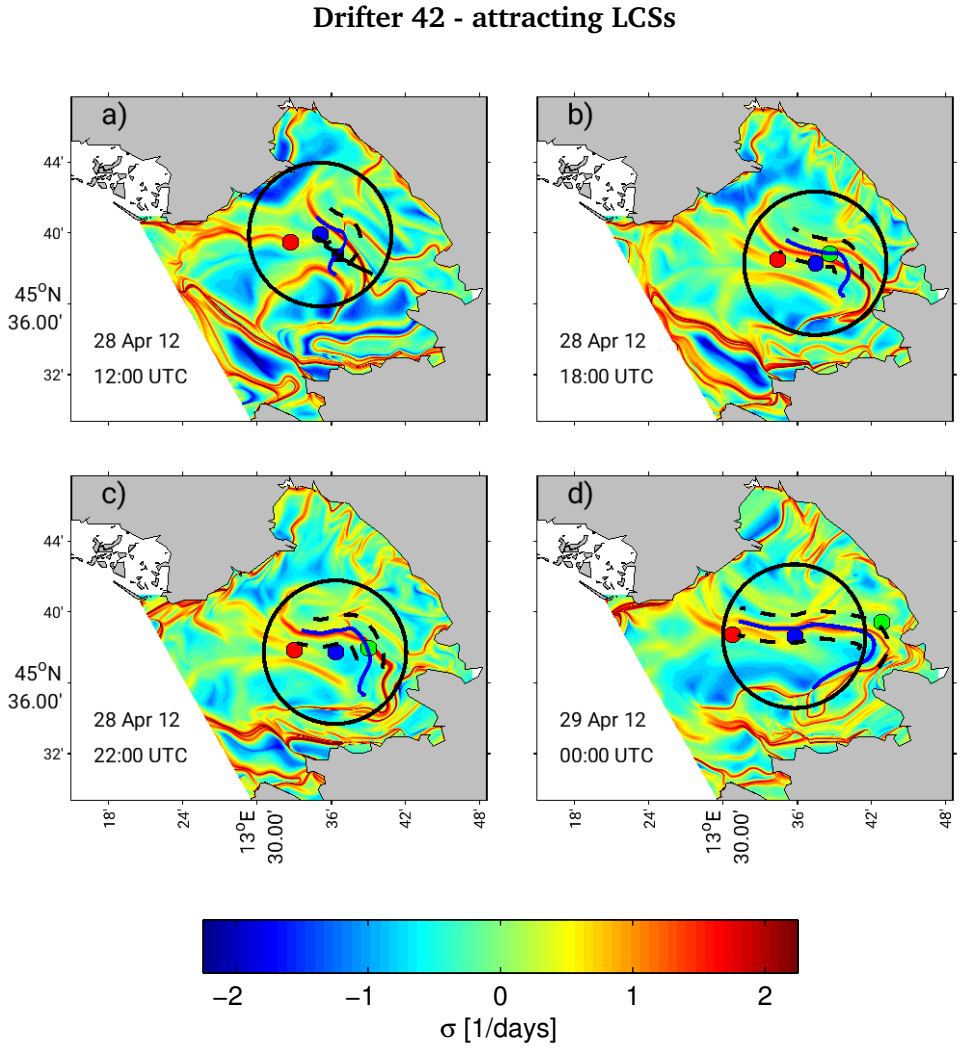

FIGURE 5.12: Application of the conceptual sketch of Figure 5.11. Attracting LCS in blue and repelling LCS in black. The black dot is the intersection between attracting and repelling LCS. Green, blue and red dots are observed and simulted drifters with and without reseeding, respectively. The scalar field underneath is the backward FTLE field. The black circle represents the searching area due to a single-particle tracking. The dashed curves are the searching areas alongside the attracting LCS. By combining these two appraches a better prediction can be obtained. The four panels represent the same time instances of Figure 5.7.

the forward FTLE field. It is evident that the searching area is greatly reduced by adopting such a combined approach. Since the dashed curves and the dark circle represent averaged values, the observed drifter (depicted in green) can take a position outside of such a region. This occurs in panel d) of Figure 5.12. Since shrinklines represent unstable lines they cannot be advected in forward time. Therefore, panels b), c) and d) show only attracting LCS. Notably, the evolution of the attracting LCSs follows the same pattern of attracting heuristic LCSs depicted in Figure 5.7 leading to a prevailing east to west elongation.

5.4 Concluding remarks of the Chapter

In the framework of the TOSCA campaign drifters were deployed in the sea and therefore the reliability of these results is assessed via analyses based on real trajectories. Transport can be studied through the concurrent use of finite-time and finite-size Lyapunov exponents (FTLEs and FSLEs) and Lagrangian Coherent Structures (LCSs). A direct comparison of FTLEs and FSLEs by evaluating their correlation is carried out showing the agreement between them. Only Boffetta et al., 2001 and Peikert et al., 2014 carried out a direct comparison between FTLEs and FSLEs. However, their analyses were only based on numerical cases. The present results show that both FTLEs and FSLEs fields are able to locate in real geophysical flows characterized by large Reynolds numbers the same pattern of Lagrangian structures, as commonly defined in literature. Indeed, the idea introduced by Peikert et al., 2014 that with an adequate choice of the main controlling parameters for FTLE and FSLE identification, i.e. the integration time T and the final separation δ_f, the two measures lead to comparable results is herein confirmed and strengthened.

Moreover, the analyses based on Lyapunov-exponent scalar fields is beneficial with respect to the ones based uniquely on the drifter-tracking. Lyapunov-exponents prove to be a valuable tool in order to evaluate the main directions along which transport phenomena are likely to occur. Despite Lyapunov-exponent diagnostics have not been employed yet as a forecasting method, this analysis shows the usefulness in nowcasting applications (Lekien et al., 2005; Shadden et al., 2009; Tang, Pak Wai, and Haller, 2011; Peacock and Haller, 2013), i.e. the accurate description of the present state of a system. It is possible to imagine that thanks to a real-time data acquisition system of velocity fields, the possible directions passive tracers could spread towards are highlighted by means of Lagrangian structures detected in real time. Therefore, if inaccurate velocity information and subgrid dynamics could decrease the reliability of single-particle tracking of passive tracers, an analysis carried out jointly with Lyapunov-exponents could shed some light on such uncertainties and give significant insight about the preferred direction of occurring transport phenomena. Heuristic LCSs have proven to be more robust against possible inaccuracy of the starting velocity fields than more standard Lagrangian approaches based on single numerical trajectories. The averaged difference between drifters and LCSs is estimated to be of the order of 1.5 km instead of about 7 km of the trajectory approach. Besides, LCSs computed following Olascoaga et al., 2013 could be directly applied in nowcasting application. However, it must be kept in mind that the better result obtained with LCSs is inherent with their elongated nature compared to the trajectory approach based on a point-to-point distances.

At the end of their seminal work Molcard et al., 2009 wondered *"whether or not dynamical system methods such as FSLE and FTLE can be applied to small coastal areas"*. The present work answers positively the question and goes beyond by computing LCSs as most attracting and repelling Cauchy-Green tensorlines in a Mediterranean

coastal environment. The development of nowcasting application, for instance directed to SaR operations, should rely on the joint use of LCSs and single-particle tracking as suggested by the present results.

Chapter 6

Shear and Shearless Lagrangian Structures

Natural rivers and, quite often, artificial channels are characterized by cross-sections composed by a deeper main channel and shallower floodplains. For this reason they are usually referred as “compound channels”. Flows of these streams are defined as predominantly horizontal since their horizontal dimensions greatly exceed the vertical one (Jirka, 2001b).

The analysis of mixing processes in natural streams is not a simple task as flow dynamics is strongly affected by channel irregularities. Flow velocity in the floodplains is lower than the one of the main channel, due to the water shallowness and to bed roughness typically higher than the main channel. As a result of the velocity gradient, shear occurs at the interface between the main channel and the floodplains. The presence of various Eulerian flow patterns most of which are characterized by large-scale vortical structures with vertical axes, i.e. macro-vortices, is well-known (Socolofksy and Jirka, 2004; Stocchino and Brocchini, 2010; Stocchino et al., 2011). The generation of these vortical structures can be described by two main approaches (Rowiński and Radecki-Pawlik, 2015): either as a shear instability at the junction of two streams (Prooijen, Battjes, and Uijttewaal, 2005) or as an outcome of differential energy dissipation of shallow-water currents interacting with submerged obstacles (Soldini et al., 2004). The former approach casts an analogy between the transitional region of the compound channel and a free mixing layer. The latter identifies the driving mechanism for the generation and sustainment of the Eulerian macro-vortices in the vorticity generation owing to the depth jump across the cross-section. Stocchino and Brocchini, 2010 showed that the shear layer thickness remains constant in compound channels. Such a condition is a peculiar consequence of the topographic forcing, i.e. the depth jump, generating the Eulerian macro-vortices. On the contrary, the shear

layer generated by the junction of two streams on an even bottom tends to grow linearly. In order to clarify strengths and shortcomings of both, a detailed comparison between the approaches pursued by van Prooijen, Battjes, and Uijttewaal, 2005 and Soldini et al., 2004 should be carried out and the outcome of the numerical simulations compared. However, the issues raised by these two different approaches are not considered in the present work. Indeed, the aim consist in analysing experimental surface velocity fields under a Lagrangian perspective disregarding the Eulerian approach. Note that it is well-known that Eulerian and Lagrangian patterns do not always correspond (Haller, 2015).

An experimental investigation on the mixing processes, in terms of Lagrangian statistics of single and multiple particles, was presented by Stocchino et al., 2011. However, the role of flow inhomogeneity was disregarded in that study. This aspect is the main subject of the present work, where the aim is to detect coherent patterns from Lagrangian measures in order to seek structures that characterise the compound channel. Key structures are located at the transition from the main channel to the lateral channels (floodplains) and approximately along the axis of the main channel. Therefore, the main focus is on Lagrangian structures that shape trajectory patterns.

The present analysis mainly relies on the computations of the Finite Time Lyapunov Exponents (FTLE) fields along with related trenches (Beron-Vera et al., 2010) and ridges (Shadden, Lekien, and Marsden, 2005), as a first diagnostic tool. However, FTLE trenches and ridges are not always a signature of the presence of material lines. Despite such a shortcoming, they are still a valuable tool to understand the dynamics of the flow. In particular, ridges are able to reveal the regions of motion that are kinematically the most active (Allshouse and Peacock, 2015a). Then, two types of heuristic structures are isolated that are mostly disregarded in previous studies: Jet-Cores (JC), i.e. shearless structures, and Shear Lagrangian Structures (SLS), respectively. JC were studied by Beron-Vera et al., 2010 and Farazmand, Blazevski, and Haller, 2014. In the present work the objective is to apply the methodology detailed in the former study based on FTLE trenches. Besides, the aim is to characterize the behaviour of heuristic JC resulting from FTLE trenches by applying the methodology described by Allshouse and Peacock, 2015b. The same method is also applied to ridges of FTLE fields that mark heuristic SLS. Such a conclusion is proven by testing heuristic SLS against their shear properties.

A further characterization of shear is carried out upon the rigorous definitions of Lagrangian Coherent Structures (LCS) (Haller, 2011; Haller and Beron-Vera, 2012). Among the general family of LCS, SLS are features dominated by a bulk shear typical of parallel flows. Herein, SLS are detected in order to mark the fundamental geometry of shear patterns. Note that SLS and JC are usually defined and studied on the basis of analytical velocity fields, whereas the main goal of the present study is to deeply investigate realistic flow conditions in a laboratory model of a typical river configuration. Heuristic SLS calculated as FTLE ridges and rigorous SLS calculated from the geodesic theory of transport barriers are compared and a nice agreement is

found.

Summing up, experimental data of time-dependent, two-dimensional Eulerian velocity fields (Stocchino and Brocchini, 2010; Stocchino et al., 2011) are employed to calculate numerical trajectories upon which JC and SLS are estimated against their shear properties. Rigorous SLS are also calculated as shearlines that minimize their geodesic deviation.

6.1 LCS detection

FTLE and tensorlines were already introduced in Chapter 2. Here, some notions preparatory to investigate compound channel flows are presented. In particular, the eigenvectors of $\boldsymbol{C}$ define directions of initial separations for which neighbouring particles are converging or diverging. Since the interest is laid on the most active regions of the fluid flow from a kinematic point of view, the FTLE in equation (3.8) is defined as a function of the maximum eigenvalue. Panel a) of Figure 6.1 shows the deformation in the neighboured of a point under the action of the flow map. Computation of FTLE can be carried out in forward time, i.e. from t_0 to $t_0 + T$, or in backward time, i.e. from $t_0 + T$ to t_0. Identification and classification of the main features of these scalar fields is the subject of the next paragraphs.

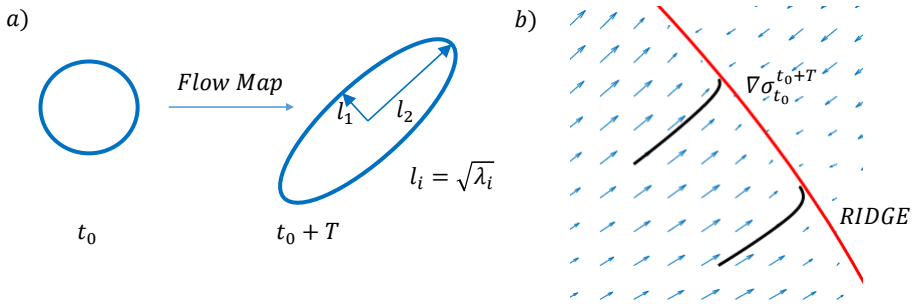

FIGURE 6.1: Panel a) shows the deformation in the neighboured of a point under the flow map $\boldsymbol{\Phi}$. A circle of unit radius is deformed as depicted. Panel b) shows the vector field $\nabla\sigma_{t_0}^{t_1}$, a ridge, in red, and two solutions of equation 6.1, in black.

6.1.1 Detection and classification of the FTLE features: ridges and trenches

Lagrangian Coherent Structures have been broadly recognised as the main features that characterise transport in fluid flows. FTLE scalar fields have been largely adopted in order to seek for heuristic Lagrangian Coherent Structures. In particular, ridges have been associated with the concept of stable and unstable manifolds: ridges calculated in forward time are considered as a signature of repelling structures whereas ridges calculated in backward time as attracting structures (Shadden, Lekien, and

Marsden, 2005). However, such a representation is undermined by some known issues (Haller and Yuan, 2000). In particular, ridges of FTLE fields can mark heuristic SLS. This applies to the present case: the transition region between the main channel and the floodplains is marked by such features, as discussed in the following.

JC can be detected at the center of the main channel. They mark absence of shear and inhibit cross-channel transport: such shearless barriers were found to strongly separate the fluid environment preventing exchange between the regions divided by them (Samelson, 1992; Rypina et al., 2007). Such structures were classified as invariant-tori-like LCS that are often present in geophysical flows Beron-Vera et al., 2010. Since infinite-time Lyapunov exponents of invariant-tori are zero and invariant-tori computed in forward time coincide with invariant-tori computed in backward time, the heuristic identification of JC relies on trenches of FTLE fields that coincide in forward and backward time.

Evaluation of the most influential structures in FTLE fields, i.e. ridges and trenches, is pursued considering the dynamical properties of these features (Mathur et al., 2007; Green, Rowley, and Haller, 2007). This technique was already pursued in Chapter 5. However, it will be further exploited here. Ridges behave as attractors of trajectories solution of the dynamical system

$$\frac{d\boldsymbol{x}}{ds} = \nabla \sigma_{t_0}^{t_0 \pm T}(\boldsymbol{x}) \tag{6.1}$$

where s is the arclength along the gradient lines of $\sigma_{t_0}^{t_0 \pm T}(\boldsymbol{x})$ and the right-hand side represents the spatial gradient of FTLE scalar fields. This property is at the base of the extraction algorithm proposed by Mathur et al., 2007 and here adopted. The reliability of such a procedure was strengthen by Peikert, Günther, and Weinkauf, 2013. Panel b) of Figure 6.1 shows the behaviour of ridges as attractors of trajectories solution of equation 6.1. The detection of trenches is analogue: the computations are carried out considering $\frac{d\boldsymbol{x}}{ds} = -\nabla \sigma_{t_0}^{t_0 \pm T}(\boldsymbol{x})$. Since the methodology is the same, in the following reference is only to ridges.

Once the ridges are detected, a hermite interpolation is adopted (Rovenski, 2010) in order to locate (first attempt) ridges made of points equally spaced between them. The advantage of Hermite cubic interpolation is twofold. Tangent vectors of the points that form the curve can be chosen and monotony property of the function (curve) that is interpolated is generally preserved. Given points P_1 and P_2 and nonzero tangent vectors Q_1 and Q_2 the cubic Hermite curve $r(s)$ is defined as

$$r(s) = (1 - 3s^2 + 2s^3)P_1 + s^2(3 - 2s)P_2 + s(s-1)^2 Q_1 + s^2(s-1)Q_2 \tag{6.2}$$

where $0 \leq s \leq 1$. However, the precision of the computed ridges is insufficient to allow for an accurate advection of these structures. Therefore, the procedure described by Allshouse and Peacock, 2015b is applied in order to refine the ridges. Following the cited approach, points belonging to a ridge are detected with a relative precision of order 10^{-7} and their advection can be reliably computed. The refinement process

is schematically depicted in Figure 6.2 and can be summurized as follows. An initial ridge (depicted in red in Figure 6.2, i.e. the curve interpolated with the Hermite polynomial) is better approximated placing a number of test points at incremental distances δ at either sides of the ridge along the normal direction. FTLE values for all these points normal to the initial ridge are then evaluated and the point with the maximum FTLE value is taken as the refined position of the ridge (green points in Figure 6.2). In case of trenches, the revised position is chosen as the corresponding minimum FTLE value.

This process is carried out recursively until a prescribed accuracy is reached. Once the final (refined) ridge is calculated, it is possible to define a tangential unit vector $\boldsymbol{\tau_0}$ to the ridge at time t_0 and a normal unit vector $\boldsymbol{n_0}$, evaluated with Frenet-Serret formulas. By applying the flow map gradient, the advected tangential vector $\nabla\boldsymbol{\Phi}\boldsymbol{\tau_0}$ and the advected normal vector $\nabla\boldsymbol{\Phi}\boldsymbol{n_0}$ are evaluated.

In order to characterize the behaviour of ridges it is possible to evaluate the quantities described by Allshouse and Peacock, 2015b. The magnitudes of the advected normal and tangential vectors, n_l and e_l, show stretching and contraction that occur to particles initially aligned along the ridge and initially perpendicular to the ridge, respectively, and can be written as:

$$n_l = \log|\nabla\boldsymbol{\Phi}\boldsymbol{n_0}| \tag{6.3}$$

$$e_l = \log|\nabla\boldsymbol{\Phi}\boldsymbol{\tau_0}| \tag{6.4}$$

Similarly, it is possible to compute the hyperbolic repulsion ρ_l and the Lagrangian shear σ_l in order to characterize how the unit normal vector $\boldsymbol{n_0}$ deforms, as:

$$\rho_l = \log|\,[\boldsymbol{n_t}\cdot(\nabla\boldsymbol{\Phi}\boldsymbol{n_0})]\,| \tag{6.5}$$

$$\sigma_l = \log|\,[\boldsymbol{\tau_t}\cdot(\nabla\boldsymbol{\Phi}\boldsymbol{n_0})]\,| \tag{6.6}$$

where $\boldsymbol{n_t}$ and $\boldsymbol{\tau_t}$ are unit normal and tangential vectors to the advected ridge. Figures 6.3 shows a pictorial representation of such quantities. Equations (6.3)-(6.6) adopt a logarithmic scaling in order emphasize stretching. A precise detection of the ridges is mandatory for a reliable computation of the quantities expressed by equations (6.3)-(6.6), in particular when the flow map gradient is applied to $\boldsymbol{\tau_0}$. Trenches of FTLE fields are characterized adopting the same measures. The predominant shear character of ridges is confirmed if σ_l is greater than ρ_l along the majority of their length. On the contrary, JC must present very small σ_l and vanishing ρ_l along the majority of their length.

6.1.2 Shear Lagrangian Coherent Structures

Recent developments in the field of Lagrangian Structures cleared that not all FTLE ridges from subsequent time intervals are material lines. Haller and Beron-Vera, 2012 developed a consistent theory in order do detect material lines that act as transport

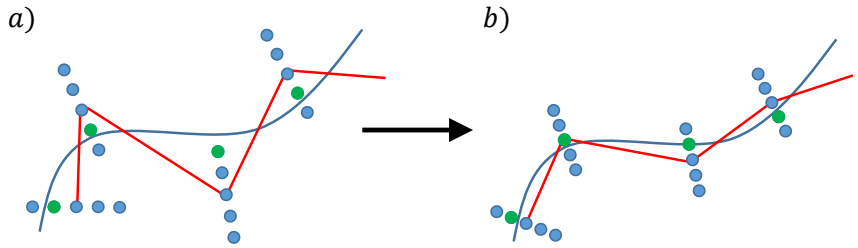

FIGURE 6.2: The refinement process adopted from Allshouse and Peacock, 2015b. The true ridge is depicted in blue. Initial guess ridge is depicted in red on the left. New maximum FTLE positions are circled in green. After recursively applying the refinement process, as shown on the right, the ridge is better approximated.

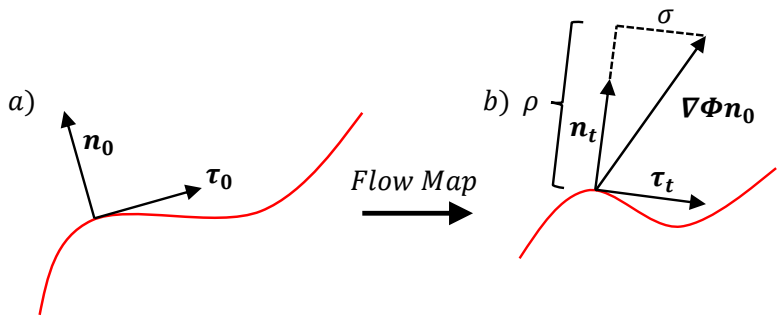

FIGURE 6.3: Pictorial representation of unit normal and tangential vectors and of hyperbolic repulsion and Lagrangian shear. Note that logarithmic scaling is not applied to this picture.

barriers. Of particular interest are material lines that attract or repel nearby fluid over a finite time interval. The normal repulsion rate introduced in the previous Section evaluates such a condition (logarithmic scaling is not essential in the definition). Necessary and sufficient criteria for the existence of repelling and attracting LCS over a finite time interval are described in terms of eigenvalues and eigenvectors of the Cauchy-Green tensor. Adopting a variational argument, Haller and Beron-Vera, 2012 showed that a curve is a hyperbolic transport barrier when it is a trajectory of the autonomous differential equation:

$$\boldsymbol{r}' = \boldsymbol{e}_1 \tag{6.7}$$

Such trajectories are defined strainlines after Haller and Beron-Vera, 2012. Considering a generic point P, the least-stretching geodesic at P under the Cauchy-Green tensor is the geodesic starting from P with a unit tangent vector expressed by equation (6.7).

In the framework of this work, the predominant features of the flow are characterised by shear. The material lines, shear LCS, that maximize Lagrangian shear $\sigma = \boldsymbol{\tau_t} \cdot (\nabla \boldsymbol{\Phi} \boldsymbol{n_0})$ are curves everywhere tangent to the shear vector field $\boldsymbol{\eta}_{\pm}$ (Haller

and Beron-Vera, 2012; Hadjighasem, Farazmand, and Haller, 2013) defined as:

$$\boldsymbol{\eta}_{\pm} = \sqrt{\frac{\sqrt{\lambda_2}}{\sqrt{\lambda_1}+\sqrt{\lambda_2}}}\boldsymbol{e}_1 \pm \sqrt{\frac{\sqrt{\lambda_1}}{\sqrt{\lambda_1}+\sqrt{\lambda_2}}}\boldsymbol{e}_2 \tag{6.8}$$

Open curves tangent to the shear vector field of equation (6.8) are shear LCS, i.e. a shear transport barrier is a trajectory of the autonomous differential equation:

$$\boldsymbol{r}' = \boldsymbol{\eta}_{\pm} \tag{6.9}$$

Such trajectories are defined shearlines after Haller and Beron-Vera, 2012. Positive Lagrangian shear signals clockwise deformation while negative Lagrangian shear signals counterclowise deformation in the local coordinate frame $(\boldsymbol{e}_1, \boldsymbol{e}_2)$. The most prominent shear LCS are shearlines that minimize the geodesic shear deviation (Hadjighasem, Farazmand, and Haller, 2013; Haller and Beron-Vera, 2012) along their length. The pointwise closeness of shear LCS to least-stretching geodesics can be computed in terms of invariants of the Cauchy-Green tensor. The geodesic deviation evaluates the difference of tangents plus the difference of curvatures of a shear LCS from the least-stretching geodesic of the Cauchy-Green tensor. Haller and Beron-Vera, 2012 provide an explicit formula in order to evaluate the geodesic deviation, which reads:

$$\begin{aligned} d_g^{\eta\pm} =& \frac{\sqrt{1+\lambda_2}-\sqrt{\lambda_2}}{\sqrt{1+\lambda_2}} + \frac{\nabla\lambda_2\cdot\boldsymbol{e}_1}{2\lambda_2\sqrt{1+\lambda_2}} \\ &\mp \frac{\langle\nabla\lambda_2,\boldsymbol{e}_2\rangle\left(\sqrt{1+\lambda_2}^3-\sqrt{\lambda_2}^5\right)}{2\lambda_2^3\sqrt{1+\lambda_2}^3} \\ &\mp \frac{\kappa_1\left[\sqrt{\lambda_2}^5+\left(1-\lambda_2^2\right)\sqrt{1+\lambda_2}\right]}{\lambda_2^2\sqrt{1+\lambda_2}} + \frac{\kappa_2}{\sqrt{1+\lambda_2}} \end{aligned} \tag{6.10}$$

with $\boldsymbol{e}_2$ denoting the eigenvector associated with λ_2, κ_1 the curvature of the strainline and κ_2 the curvature of $\boldsymbol{e}_2$ vector field. The predominant shear LCS is chosen as the shearline whose average geodesic deviation

$$\text{avg}(d_g^{\eta\pm}) = \frac{\int d_g^{\eta\pm}|\boldsymbol{r}'|ds}{\int|\boldsymbol{r}'|ds} \tag{6.11}$$

is the least among all. Computations of FTLE fields and shear LCS are carried out following Onu, Huhn, and Haller, 2015 and Farazmand and Haller, 2012. A MATLAB toolbox was made publicly available by these Authors and it has been here exploited.

6.2 Experimental flow field

The present analysis is based on the experimental measurements of the free-surface Eulerian velocity fields described in Stocchino and Brocchini, 2010 and Stocchino et al., 2011. Herein, the main characteristics of the apparatus and of the measuring

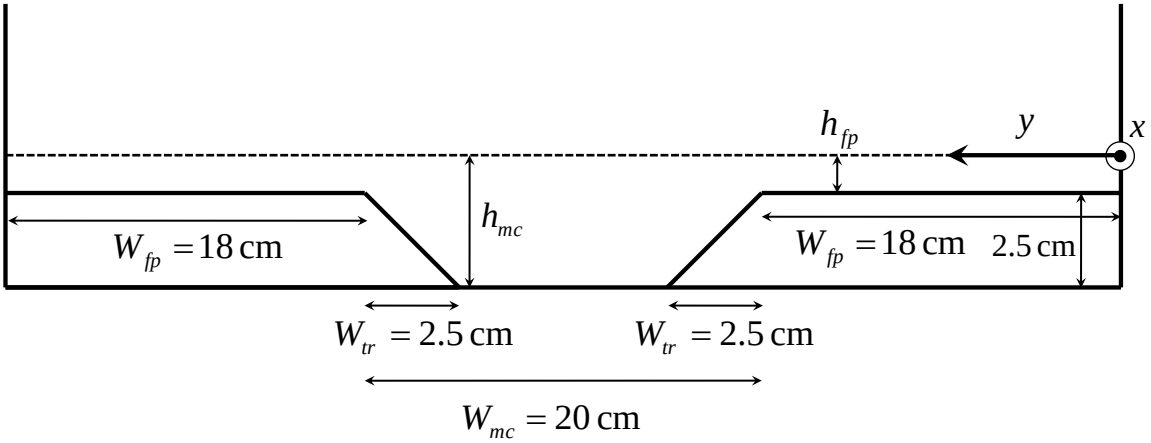

FIGURE 6.4: Sketch of the cross section of the flume.

Exp.	r_h (-)	Fr (-)	S (-)	$Re \times 10^4$ (-)
201	4.16	0.60	0.0032	20.1
207	2.26	0.73	0.0032	51.8
105	2.15	1.05	0.0064	84.9
213	1.68	0.82	0.0032	130.1

TABLE 6.1: Main experimental parameters.

system is recalled. The flume was 20 m long, 60 cm wide and the trapezoidal cross-section was composed by a central main channel ($W_{mc} = 20$ cm), two lateral flat floodplains ($W_{fp} = 18$ cm) and a transition region ($W_{tr} = 2.5$ cm). Figure 6.4 shows the cross section of the flume.

Velocity measurements have been performed by means of a two-dimensional Particle Image Velocimetry system on a field of view of (1.2×0.6)m^2. The acquisition rate was between 100 Hz and 250 Hz, depending on the flow velocity. Each acquisition was made of a number of frames between 2000 and 4000. Several series of experiments have been carried out spanning a large range of values of the main physical parameters. In table 6.1 the experimental conditions are summarized, providing the values of the ratio between the main channel water depth (h_{mc}) and that of the floodplains (h_{fp}), $r_h = h_{mc}/h_{fp}$, and the Froude number, $Fr = U_m/\sqrt{gR}$, where R is the hydraulic radius, g is gravity and U_m is the peak velocity in the main channel. Moreover, S represents the longitudinal bed slope.

The same distribution of the flow regimes is kept depending on r_h introduced in Nezu, Onitsuka, and Iketani, 1999 and used in Stocchino et al., 2011. As pointed out by Nezu, Onitsuka, and Iketani, 1999 three different flow regimes can be identified depending on the value of r_h. For $r_h > 3$ the flow is defined as “Shallow”. In this case, intense velocity gradients occur at the transition between the main channel and the floodplains, leading to a strong shearing and a generation of vorticity associated

with the flow depth jump Soldini et al., 2004. For values of $r_h < 2$, the flow is defined as "Deep", characterized by a weaker shear in the transition region. The flow depth jump, in this case, is unable to greatly influence the free-surface flow. Finally, "Intermediate flows" are defined when $2 < r_h < 3$. In the framework of their analysis Stocchino et al., 2011 evaluated single and multiple particles statistics. Since a constant mean velocity causes the absolute dispersion to increase quadratically in time, and thus the diffusivity to increase linearly in time, their analysis was carried out removing a constant mean from the velocity field. In the case of compound channel flows, a mean motion does exist in the stream-wise direction and it is non-homogeneous over the cross-section. The mean stream-wise velocity assumes a bell-like distribution as shown in Stocchino and Brocchini, 2010 and its shape depends strongly on the flow depth ratio r_h. As a result, for a 2D flow evolving in the plane the residual velocity reads as

$$\boldsymbol{u}'(x,y,t) = \boldsymbol{u}(x,y,t) - \boldsymbol{U}(x,y) \tag{6.12}$$

where $\boldsymbol{U}(x,y)$ indicates the velocity averaged over the duration of the single realization. This method is adequate to handle flows that are inhomogeneous, like in the present case or in oceanographic applications, while the classical results of Taylor were obtained assuming $\boldsymbol{U}(x,y) = 0$, i.e. for homogeneous flows. The analysis is then carried out upon such velocity field in agreement with Stocchino et al., 2011.

SLS and JC are discussed in detail for one run of each class, showing the recurrent features of every corresponding class.

6.2.1 Assessment of two-dimensionality

In the framework of the present work, the fluid flow is considered two-dimensional. Indeed, the measurements presented in Stocchino and Brocchini, 2010 and Stocchino et al., 2011 were taken on the free surface assuming that the flow is mainly two dimensional. This experimental approach based on the free surface velocity measurement is often used in many experimental works with primary focus on quasi-2D vortical structures see Nikora et al., 2007; Socolofksy and Jirka, 2004; Jirka, 2001b, among others. This approach is valid as long as the secondary flows can be considered negligible in the formation of the quasi-2D vortical structures with vertical axis of rotation and confined in a layer close to the bottom. However, in order to verify this hypothesis the Lagrangian divergence is here evaluated. In particular, Mathur et al., 2007 define Lagrangian divergence as:

$$L(\boldsymbol{x}) = \int_{t_0}^{t_1} \left[\nabla \cdot \boldsymbol{v}\right]_{\boldsymbol{\Phi}(t_0;t,\boldsymbol{\xi})} dt \tag{6.13}$$

where $\boldsymbol{v} = \boldsymbol{u}'$ in the present case. The Lagrangian divergence is computed along particle paths and should be zero for purely 2D flows. It represents the factor by which infinitesimal areas are magnified. Figure 6.5 shows a typical snapshot of $L(\boldsymbol{x})$ for a

shallow flow case. The Lagrangian divergence presents a quite flat distribution with the only exception of few peaks located at the transition region. The overall values are well below unity and much smaller than the ones found by Mathur et al., 2007 in a rotating water tank where the flow is considered manly two-dimensional. This measure is also employed by Wilson, Tutkun, and Cal, 2013 in a turbulent boundary layer in order to quantify its two-dimensionality. They found a mean value of $\exp(L)$ close to 1.2 over their entire domain, arguing that stretching along one direction is balanced by convergence in another direction. Further considerations led them to accept the flow as two-dimensional.

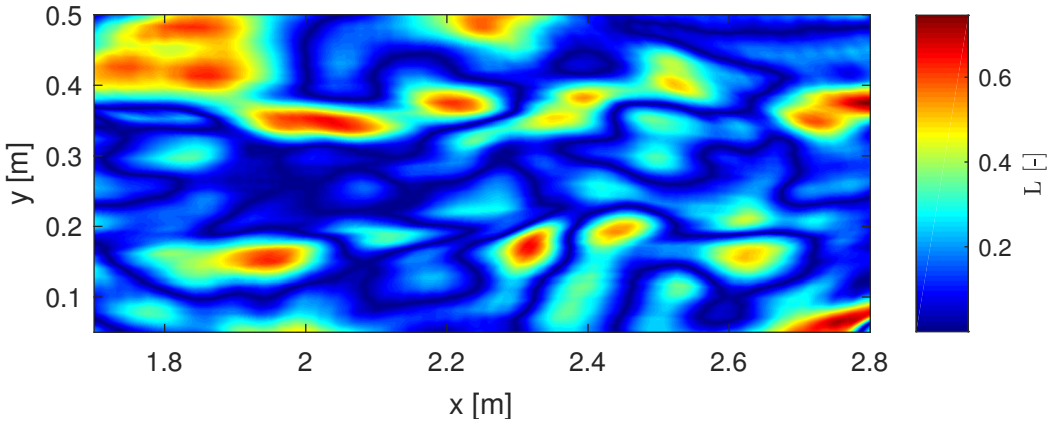

FIGURE 6.5: Lagrangian divergence evaluated on a time interval of 1s for EXP 201.

Besides, divergence-free flows have FTLE fields non-negative (Arnol'd, 1992; Lipinski and Mohseni, 2010). Therefore, an indirect proof of the low three-dimensionality of the flow can be obtained inspecting FTLE fields. As showed in the following Sections negative FTLE values are very few. Therefore, the assumption of two-dimensionality can be fully accepted.

6.3 Results

Four experimental cases are reported in detail as prototypical examples of the respective flow conditions: shallow flows, intermediate flows and deep flows. In the case of intermediate flows, two regimes have been further investigated, namely flow in subcritical and supercritical conditions. The integration time is set to one second in order to let particle stay inside the computational domain. Furthermore, such an integration time has the same order of magnitude of the Lagrangian decorrelation time evaluated by Stocchino et al., 2011 on the same dataset.

It is worthy to recall the theoretical analysis reported in Haller and Beron-Vera, 2012, where the Authors studied a parallel shear flow as a benchmark case. In particular, the velocity field of the shear flow investigated takes the form

$$\dot{x} = u(y,t) \tag{6.14}$$

$$\dot{y} = v(y) \tag{6.15}$$

on a planar domain with non-vanishing and non-linear time-averaged shear ($a(y) = \int_{t_0}^{t} u(y,\tau)d\tau \neq 0$ and $^{da(y)}/_{dy} \neq 0$). One of the main conclusions of the work by Haller and Beron-Vera, 2012 was that, in such a framework, any horizontal line is a shear LCS. Despite several important differences, it is possible to cast an analogy between the above flow and the compound channel flows here discussed. Indeed, although both velocity components are time dependent in the case of compound channels, the shear pattern heuristically conforms to the parallel shear flow described by equations (6.14) and (6.15), since shear LCS do develop in the stream-wise direction and are advected in the same direction.

In particular, the expected pattern must be symmetric with respect to the axis of the channel because the residual velocity, equation (6.12), upon which equation (1.1) is solved determines a flow direction of the main channel reversed with respect to the floodplains. Figure 6.6 shows a pictorial representation of shear LCS marking positive and negative shear, which can be detected in compound channels at the transition between the main channel and the floodplains. Indeed, the bottom region of the Figure shows positive shear whereas the top region negative shear, defined in agreement with the convention adopted for equation (6.9).

A shearless structure is present along the axis of the main channel marking a JC. The main channel is characterized by low values of FTLE fields and trenches can be detected. This is the typical configuration resulting from a bell-shaped velocity profile.

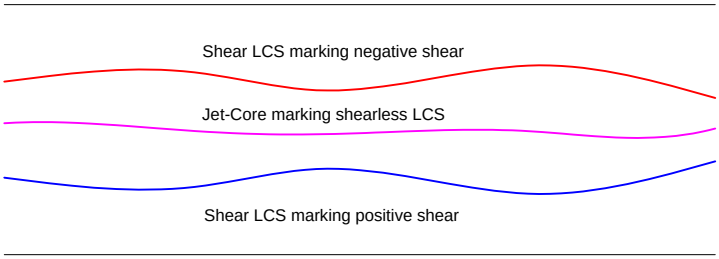

FIGURE 6.6: Pictorial representation of the shear LCS of the compound channel, in red and blue. At the center of the main channel a JC is present, in magenta.

In the following, the main results obtained starting from a general description of the behaviour of the FTLE fields are presented and then go forward with a detailed description of the Lagrangian structures depending on the flow regime.

6.3.1 General behavior of FTLE fields

Coherent patterns are firstly detected through FTLE fields and they are found to behave in agreement with equations (3.14) and (3.15). By choosing 12 different initial conditions and evaluating FTLE fields with integration times varying from 0.1 to 5.7 s, it is possible to obtain the results plotted in Figure 6.7. This Figure shows two bundles of 12 curves representing the average and the standard deviation of the values of FTLE fields as a function of the integration time. Note that the different curves are so closed to each other that can be hardly identified separately. The trends of both

quantities, average and standard deviation, are in agreement with the expected theoretical results for ergodic systems, showing a monotonic decay in time as predicted by Abraham and Bowen, 2002.

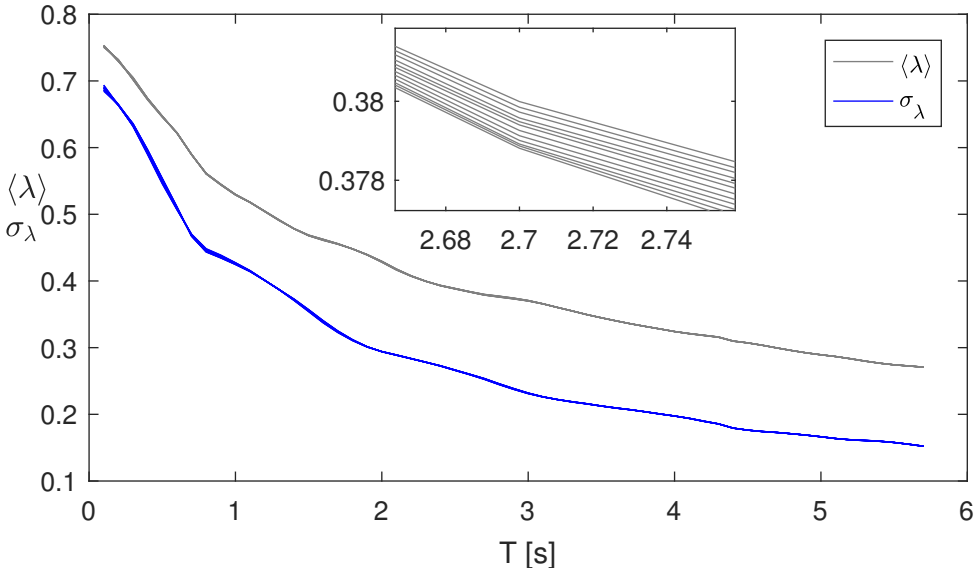

FIGURE 6.7: FTLE average and standard deviation as a function of integration time for 12 different initial conditions. The close up helps in identifying the different curves.

Moreover, the probability density function (pdf) of the FTLE are expected to behave accordingly. In particular, as the the integration time increases the pdf tends to a Dirac delta centered at the limit FTLE value, see Figure 6.8. Owing to the two-dimensionality of the flow at hand, it is reasonable to expect that FTLE values are mainly positive, leading to positively skewed pdfs.

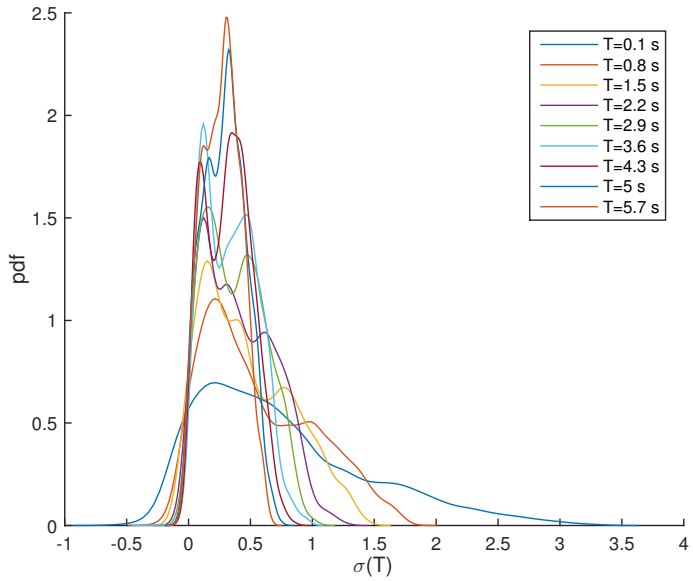

FIGURE 6.8: Probability density function for FTLE fields.

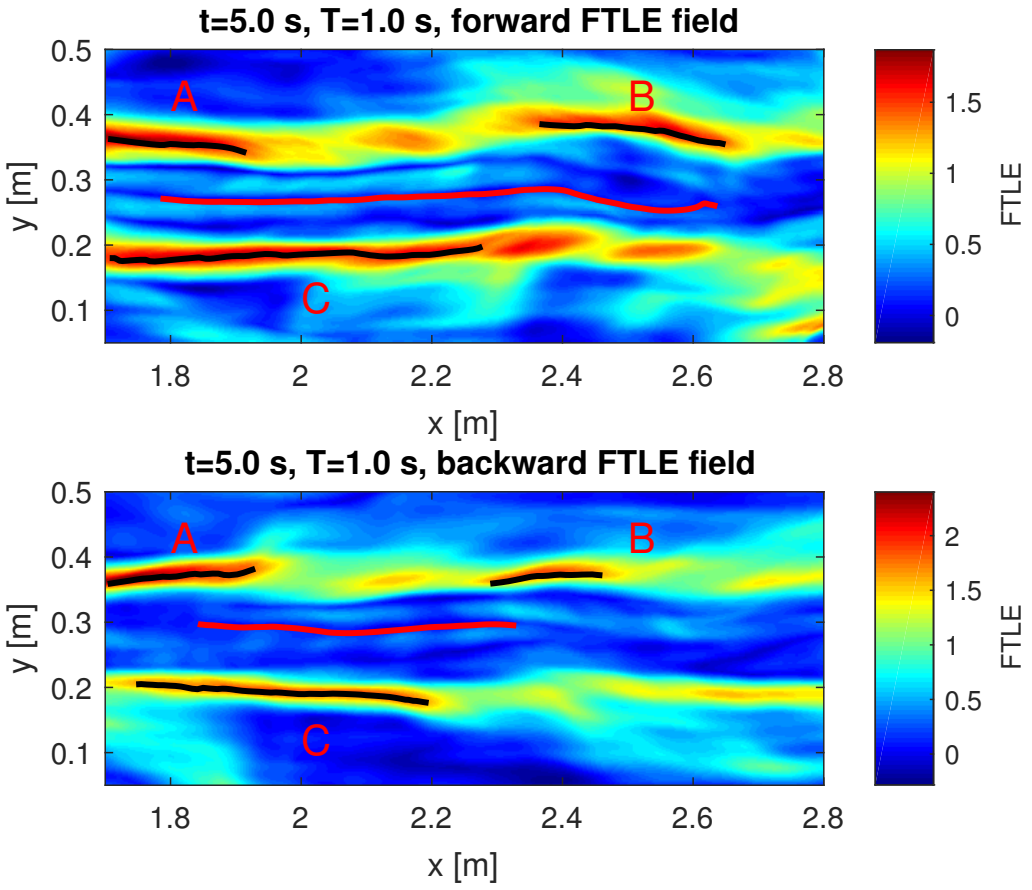

FIGURE 6.9: Forward and backward FTLE ridges for EXP 201, shallow flow conditions. Letters identify predominant FTLE ridges. Trenches are marked in red.

6.3.2 Shear and Shearless structures in shallow conditions

Experiment 201 is considered as a prototypical case of shallow conditions since it was carried out with a ratio $r_h = 4.16$. Note that the flow for this case is in subcritical regime ($F_r = 0.60$). Figure 6.9 shows typical Lagrangian patterns of shallow flow conditions. Panel a) and b) depict a snapshot of the forward and backward FTLE fields evaluated at t=5.0s, respectively. Both forward and backward fields show structures at the transition from the main channel to the lateral floodplains. Upon each field, three main structures depicted in black are identified and their ridges isolated. At the center of the main channel trenches are identified and depicted in red. In order to prove the predominant shear character of ridges, the magnitude of the advected unit normal and tangential vectors are computed taking advantage of equations (6.3) and (6.4). Besides, repulsion and Lagrangian shear are evaluated applying equations (6.5) and (6.6). Figures 6.10 and 6.11 show such quantities as a function of the curvilinear coordinated s along forward and backward ridges, respectively.

In all cases the growth of the normal vectors is greater than the growth of the tangential vectors, i.e. n_l is greater then e_l. The growth of the normal vector $\boldsymbol{n_0}$ is predominantly due to Lagrangian shear, since σ_l is greater than ρ_l along each ridge for almost their entire length. Ridge C belonging to the forward field of Figure 6.9,

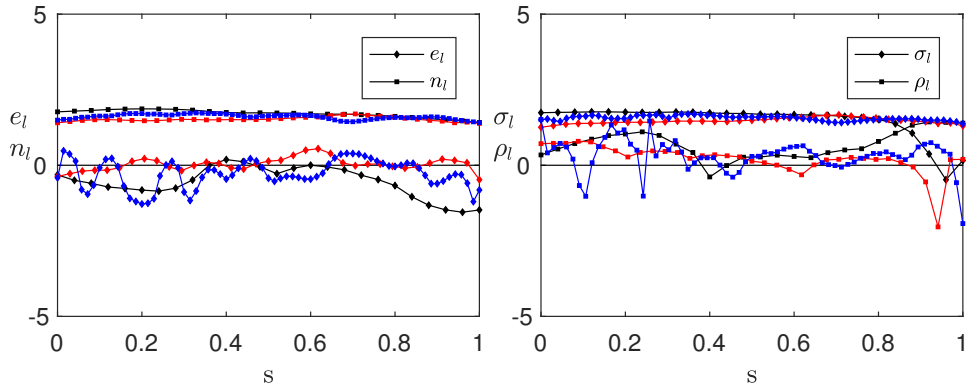

FIGURE 6.10: Forward FTLE ridges normal and tangential advected unit vector magnitudes, e_l and n_l on the left, and hyperbolic repulsion and Lagrangian shear, σ_l and ρ_l on the right. Black, red and blue colors refer to ridges A, B and C of Panel a) of Figure 6.9, respectively.

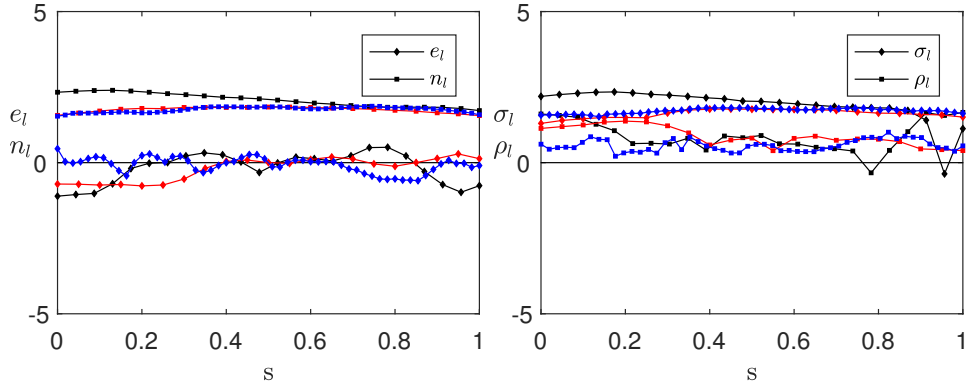

FIGURE 6.11: Backward FTLE ridges normal and tangential advected unit vector magnitudes, e_l and n_l on the left, and hyperbolic repulsion and Lagrangian shear, σ_l and ρ_l on the right. Black, red and blue colors refer to ridges A, B and C of Panel b) of Figure 6.9, respectively.

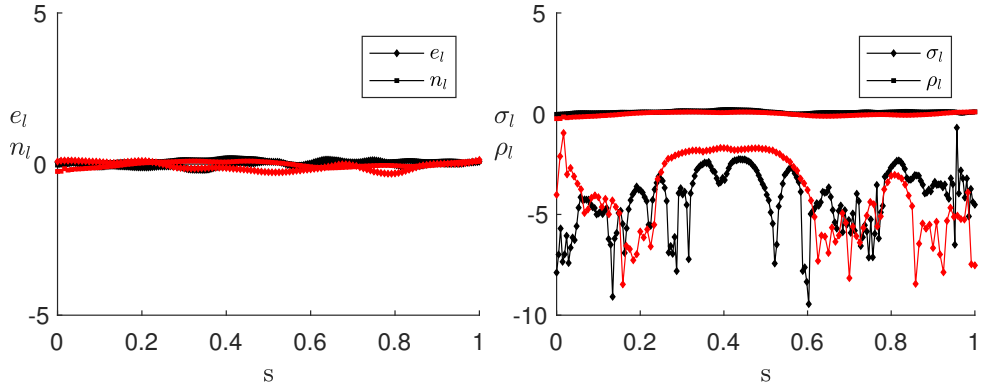

FIGURE 6.12: Quantification of repelling and shear properties of JC. Panel a) shows n_l and e_l for forward and backward trenches of Figure 6.9, in red and black respectively. Panel b) shows ρ_l and σ_l with the same color coding.

panel a), shows some noisy signal in the hyperbolic repulsion, depicted in Figure 6.10. This behavior is all but surprising since it is encountered even from dataset

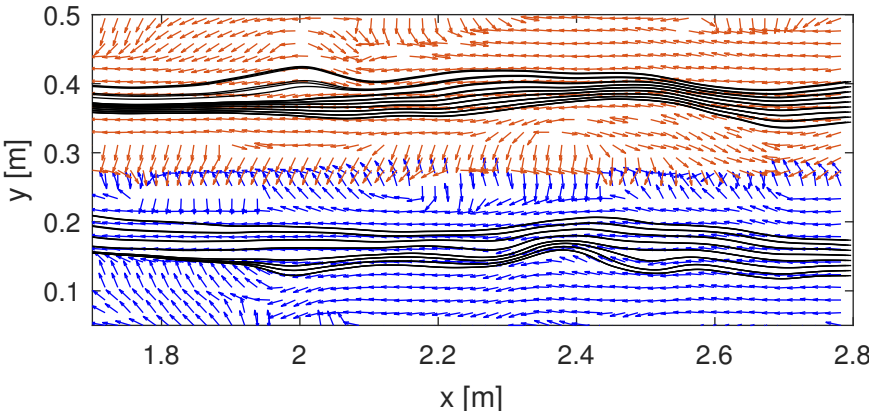

FIGURE 6.13: Positive, in blue, and negative shear vector field, in red. Positive and negative shear LCS are superimposed on the respective fields.

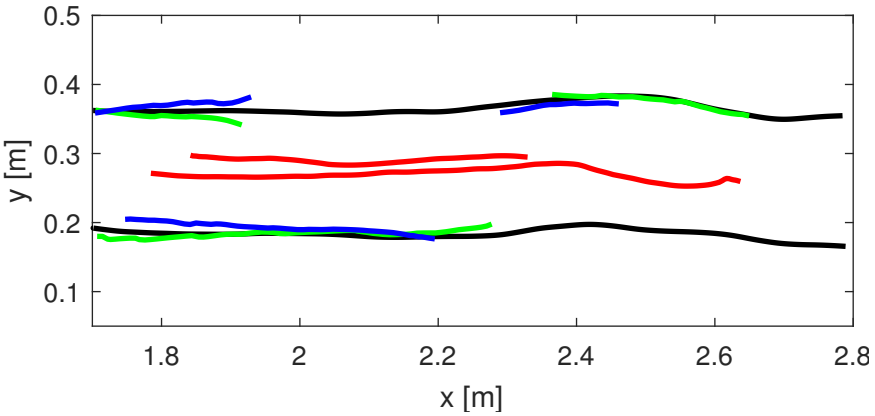

FIGURE 6.14: Predominant positive and negative shearlines, in black, superimposed on forward FTLE field, EXP 201. Forward FTLE ridges, in green, and backward in blue. JC resulting from forward and backward FTLE fields are depicted in red.

resulting from numerical simulations (Allshouse and Peacock, 2015b). These quantitative results suggest that material elements initially aligned along FTLE ridges will tend to move consistently without significant elongations. On the contrary, material elements initially perpendicular to the ridges will stretch because of shear.

Trenches of FTLE fields are identified at the center of the main channel where low FTLE values appear. These trenches behave as JC showing absence of shear. Panel a) of Figure 6.12 shows that n_l and e_l are almost zero along the entire length of both JC evaluated from forward and backward fields. This means that along JC unit normal and tangential vectors are not significantly deformed. Panel b) show that ρ_l is almost zero whereas σ_l is very small. This reflects the fact that unit normal vectors do not deform and their projection along the tangential direction to the ridge is negligible.

FTLE ridges are nicely in agreement with shearlines. Figure 6.13 shows positive shear vector field (in the lower part of the domain, in blue) and negative shear vector field (in the upper part of the domain, in red). The corresponding positive and negative shearlines are superimposed on the corresponding areas. This particular pattern is due to the symmetry of the problem. Clockwise shear in the lower part

of the domain is reflected in counterclockwise shear in the upper part of the domain (see for comparison Figure 6.6). Figure 6.14 shows the predominant shear LCS (in black) that minimize the geodesic deviation. Forward ridges of Figure 6.9 are plotted in green and backward ridges in blue. They are not perfectly aligned with shear LCS since the eigenvectors associated with maximum eigenvalues differ from the shear vector field. However, their alignment is remarkable. JC are depicted in red and are located at the center of the main channel. They do not perfectly superimpose. Increasing the integration time should lead to a better superposition. However, this leads to an accumulation of particles to the boundaries resulting in a splintering of the ridges. As a result, the integration time is kept to one second.

6.3.3 Shear and Shearless structures in intermediate conditions - subcritical case

Experiment 207 was carried out with a ratio $r_h = 2.26$ and it belongs to intermediate and subcritical conditions ($Fr = 0.73$). It is analyzed as a reference configuration for this type of flows. FTLE fields show in general a pattern comparable to shallow conditions even if high FTLE regions protrude towards lateral channels. Figure 6.15 shows the FTLE field and represents the general configuration of interest for forward and backward fields. Seven predominant ridges are identified in forward time and two in backward time. Their behavior is characterized with the same procedure followed in the previous Section. Analogously to the shallow case, Lagrangian shear is predominant to repulsion, as depicted in Figure 6.16 and 6.17, classifying these ridges as SLS. Compared to the shallow case, higher values of FTLE are obtained in the floodplains. Such values could reach peaks comparable to those of the transition region, see panel a) of Figure 6.15. At the center of the main channel trenches of FTLE fields are identified. Figure 6.18 quantifies shear properties of such trenches and qualifies them as JC, showing results analogue to those of Exp. 201. However, the extension of the region where low FTLE values are present contracts.

Figure 6.19 shows positive shear vector field (in the lower part of the domain, in blue) and negative shear vector field (in the upper part of the domain, in red) with a pattern analogous to the previous case. Figure 6.20 shows the shear LCS that minimize the geodesic deviation alongside ridges and trenches. Shear LCS do align along longitudinal FTLE ridges. JC identified in both forward and backward fields superimpose much better than in the case of Exp. 201.

6.3.4 Shear and Shearless structures in intermediate conditions - supercritical case

Experiment 105 was carried out with a ratio $r_h = 2.15$ belonging to intermediate and supercritical conditions ($Fr = 1.05$). FTLE fields show in general a pattern comparable to intermediate and subcritical conditions. Figure 6.21 shows the FTLE

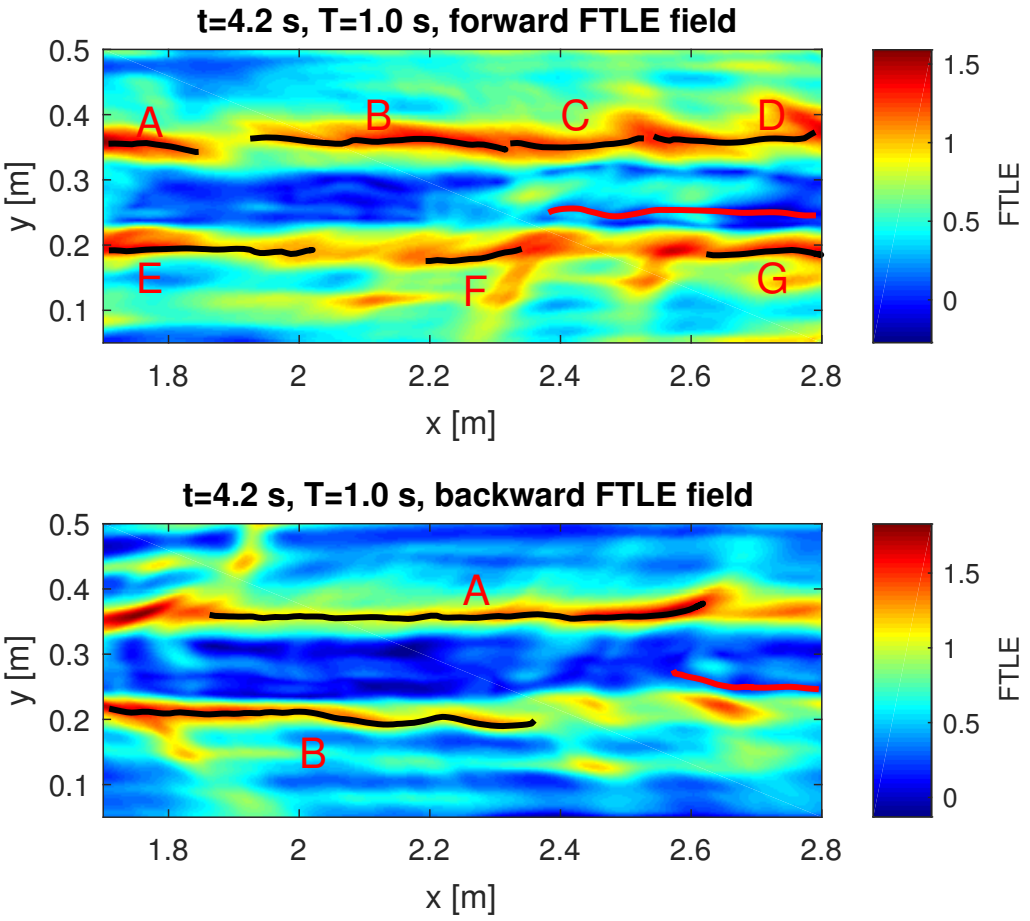

FIGURE 6.15: Forward and backward FTLE ridges for EXP 207, intermediate flow conditions, subcritical case. Letters identify predominant FTLE ridges. Trenches are marked in red.

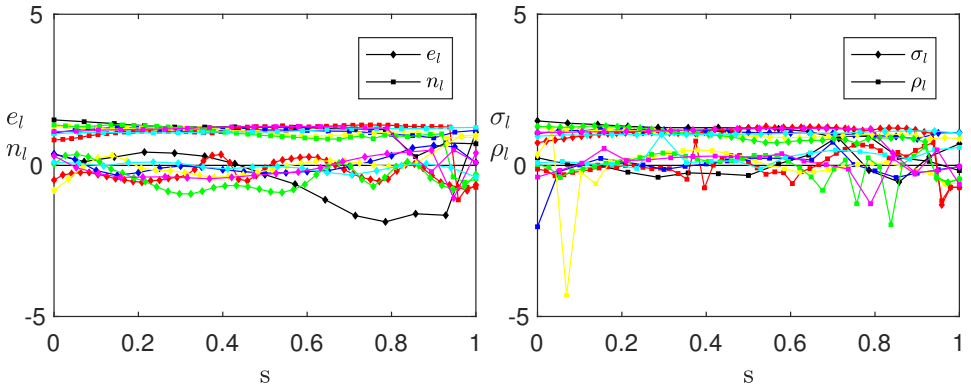

FIGURE 6.16: Forward FTLE ridges normal and tangential advected unit vector magnitudes, e_l and n_l on the left, and hyperbolic repulsion and Lagrangian shear, σ_l and ρ_l on the right. Black, red, blue, yellow, green, cyan and magenta colors refer to ridges A, B, C, D, E and G of Panel a) of Figure 6.15, respectively.

field representing the general configuration of interest for forward and backward fields.

Four predominant ridges are identified in forward time and two in backward time.

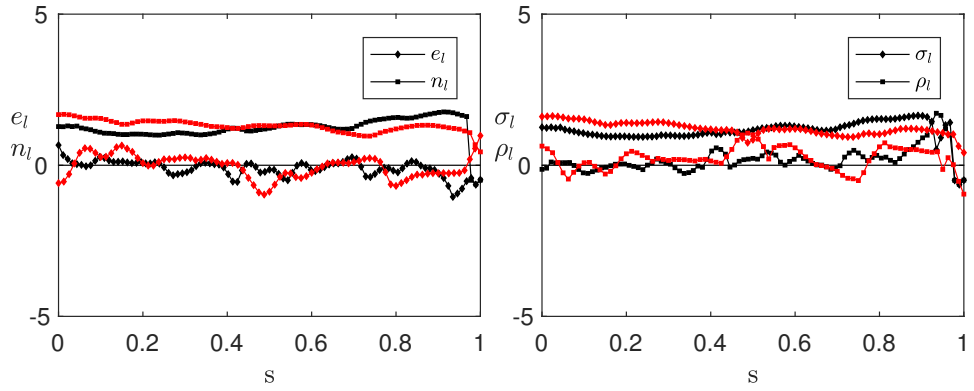

FIGURE 6.17: Backward FTLE ridges normal and tangential advected unit vector magnitudes, e_l and n_l on the left, and hyperbolic repulsion and Lagrangian shear, σ_l and ρ_l on the right. Black and red colors refer to ridges A and B of Panel b) of Figure 6.15, respectively.

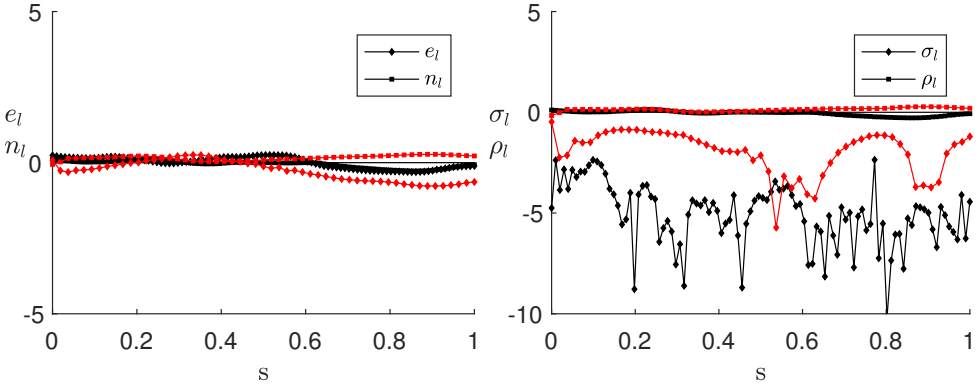

FIGURE 6.18: Quantification of repelling and shear properties of JC. Panel a) shows n_l and e_l for forward and backward trenches of Figure 6.15, in red and black respectively. Panel b) shows ρ_l and σ_l with the same color coding.

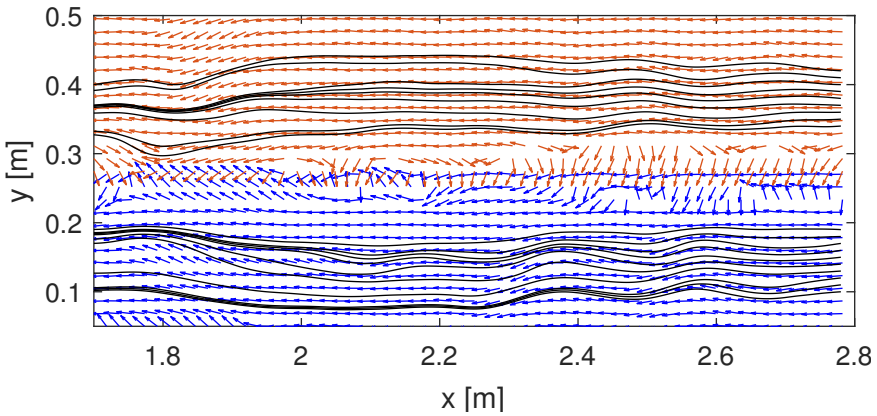

FIGURE 6.19: Positive, in blue, and negative shear vector field, in red. Positive and negative shear LCS are superimposed on the respective fields.

Higher FTLE values are located at the transition region. However, some ridges do not completly align along the stream-wise direction. In particular ridges C of panel a) and B of panel b) of Figure 6.21 tend to align diagonally with respect to the stream-wise direction. As a result, for these specific ridges, Lagrangian shear is not

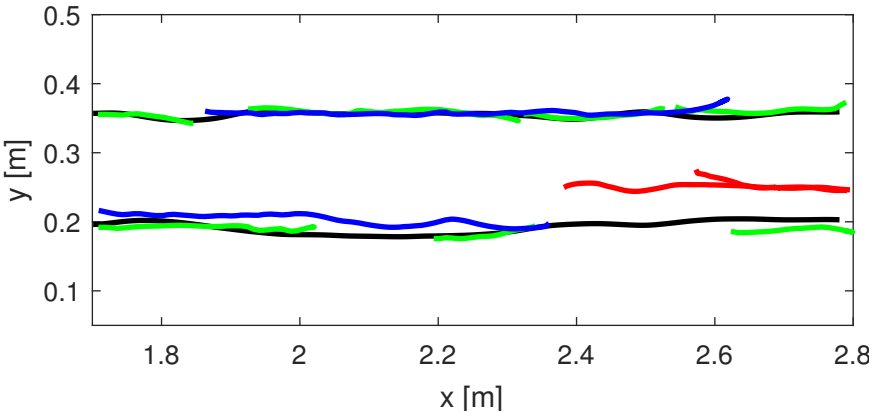

FIGURE 6.20: Predominant positive and negative shearlines, in black, superimposed alongside with forward FTLE ridges, in green, and backward in blue. JC are depicted in red.

always predominant over hyperbolic repulsion. Figures 6.22 and 6.23 show that the magnitude of the advected normal is always greater than the magnitude of the advected tangential vector for all the ridges. Such predominance is due to Lagrangian shear except for the ridges with diagonal alignment. Therefore, these ridges are not classified as SLS since they show for a non-negligible length a hyperbolic behaviour. Very well defined trenches are detected at the center of the main channel. Figure 6.24 shows the shear properties of these trenches that qualify as JC with negligible shear.

Figure 6.25 shows positive shear vector field (in the lower part of the domain, in blue) and negative shear vector field (in the upper part of the domain, in red) with a pattern analogous to the previous case. Figure 6.26 shows the shear LCS that minimize the geodesic deviation. These shear LCS align with ridges of FTLE fields except for ridges C of panel a) and B of panel b) of Figure 6.21. This explains why hyperbolic repulsion is predominant over Lagrangian shear along some portions of these ridges. On the contrary, JC are very well superimposed.

6.3.5 Shear and Shearless structures in deep conditions

Experiment 213 was carried out with a ratio $r_h = 1.68$ and in subcritical conditions ($Fr = 0.82$). It is analysed as a reference configuration for deep flow conditions. FTLE fields show in general a pattern with the absence of persistent structures. Figure 6.27 shows the FTLE field representing the general configuration of interest for forward and backward fields. In deep conditions the FTLE field is less readable and regions with high FTLE values protrude towards the inner of the main channel. Four predominant ridges are identified in forward time and two in backward time. Their behaviour is characterized with the same procedure followed in the previous Sections. Analogously to the previous cases, Lagrangian shear is predominant to repulsion, as depicted in Figure 6.28, for ridges that are mainly longitudinal, i.e A and C of the

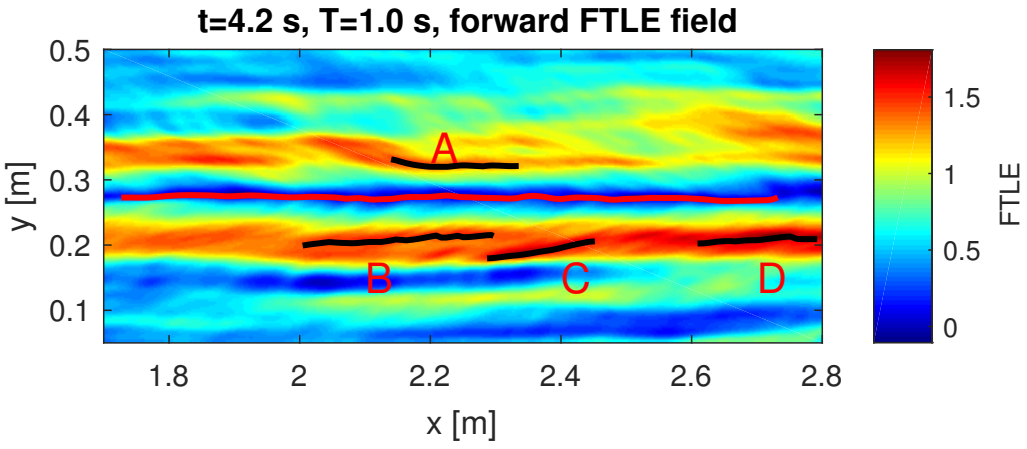

a)

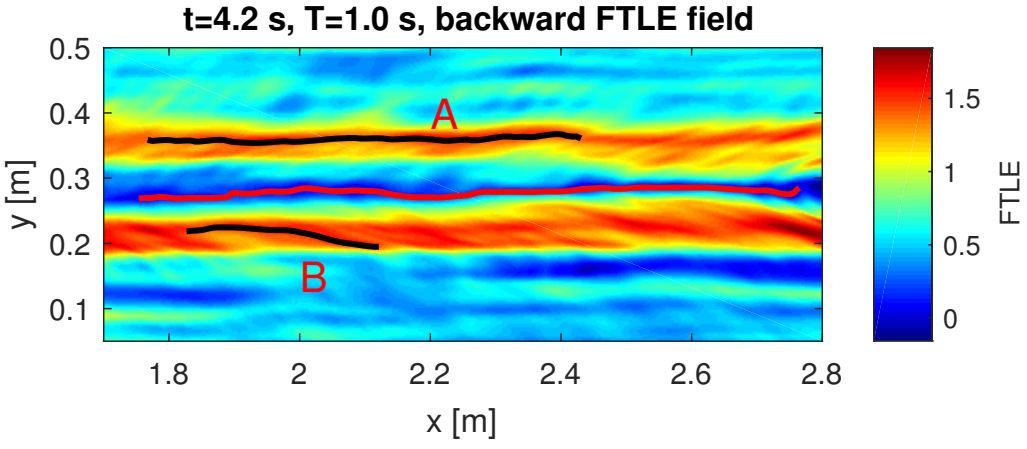

b)

FIGURE 6.21: Forward and backward FTLE ridges for EXP 105, intermediate flow conditions, supercritical case. Letters identify predominant FTLE ridges. Trenches are marked in red.

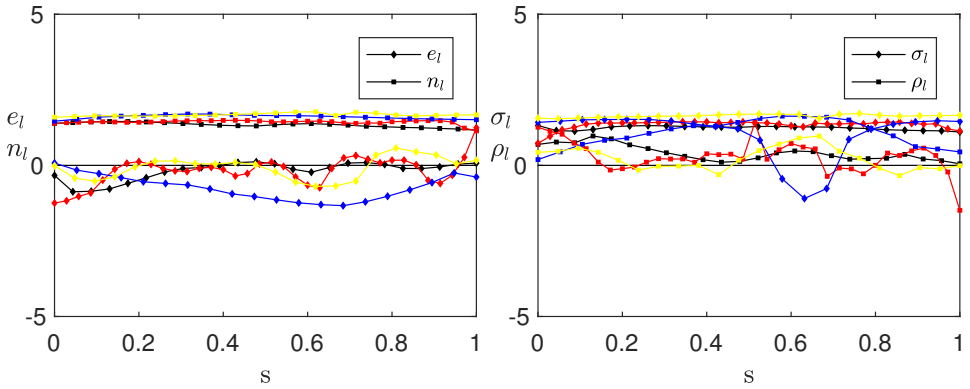

FIGURE 6.22: Forward FTLE ridges normal and tangential advected unit vector magnitudes, e_l and n_l on the left, and hyperbolic repulsion and Lagrangian shear, σ_l and ρ_l on the right. Black, red, blue and yellow colors refer to ridges A, B, C and D of Panel a) of Figure 6.21, respectively. Hyperbolic repulsion of ridge C is comparable and even predominant over Lagrangian shear.

forward field (panel a) of Figure 6.27). Transverse ridges, B and D, show, on the contrary, comparable Lagrangian shear and repulsion strength and, consequently, cannot be classified as a SLS. Such a behaviour, showed in Figure 6.29, characterizes even

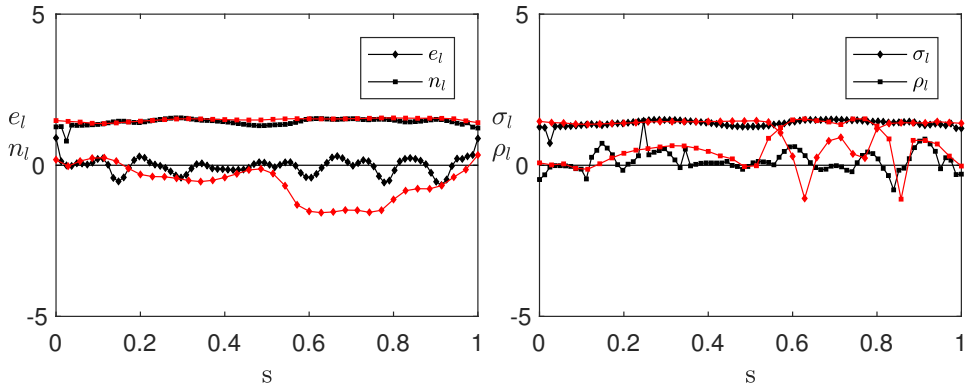

FIGURE 6.23: Backward FTLE ridges normal and tangential advected unit vector magnitudes, e_l and n_l on the left, and hyperbolic repulsion and Lagrangian shear, σ_l and ρ_l on the right. Black and red colors refer to ridges A and B of Panel b) of Figure 6.21, respectively. Hyperbolic repulsion of ridge B is predominant over Lagrangian shear along a significant portion of its length.

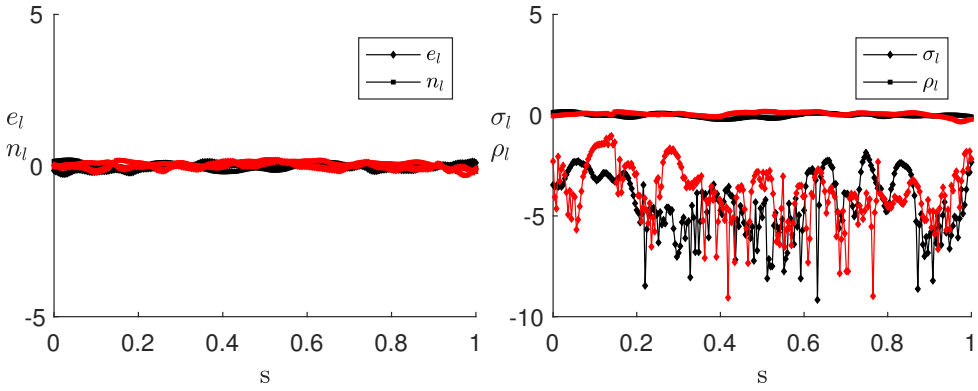

FIGURE 6.24: Quantification of repelling and shear properties of JC. Panel a) shows n_l and e_l for forward and backward trenches of Figure 6.21, in red and black respectively. Panel b) shows ρ_l and σ_l with the same color coding.

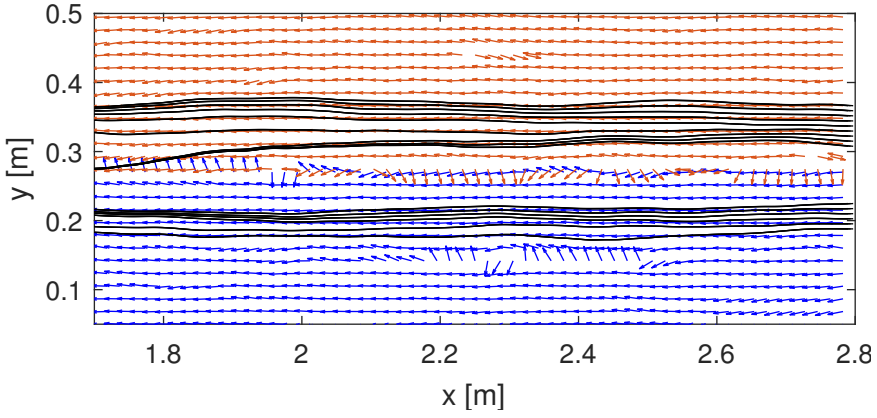

FIGURE 6.25: Positive, in blue, and negative shear vector field, in red. Positive and negative shear LCS are superimposed on the respective fields.

ridge B belonging to the backward field (panel b) of Figure 6.27). Trenches are located at the center of the main channel. However, the width of the low FTLE region has shrunk significantly compared to the previous cases. As a result, trenches tend to be interrupted by higher values of FTLE. Figure 6.30 quantifies the shear properties

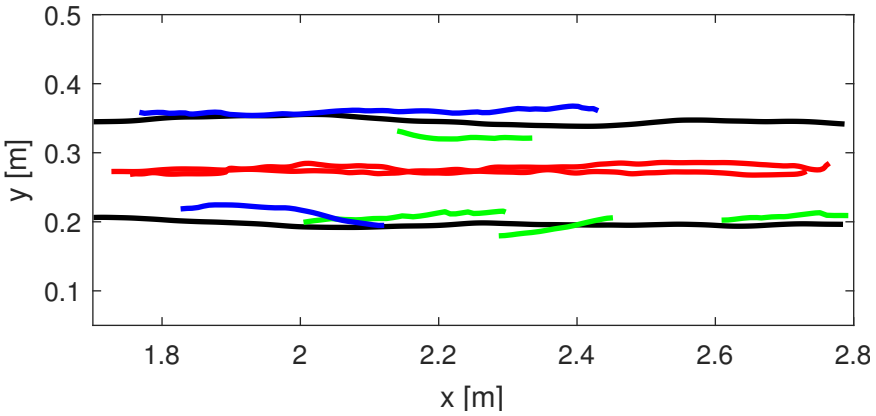

FIGURE 6.26: Predominant positive and negative shearlines, forward FTLE ridges in green, backward in blue and JC in red.

of these trenches that can be consequently classified as JC.

Figure 6.31 shows positive shear vector field (in the lower part of the domain, in blue) and negative shear vector field (in the upper part of the domain, in red) with a pattern analogous to the previous case. Figure 6.32 shows the shear LCS that minimize the geodesic deviation. These shear LCS do align along longitudinal FTLE ridges. JC do superimpose as expected.

As a general comment of such a flow condition it is possible to argue a strong independence of the surface flow from the depth jump. Indeed, transition region from the main channel to the floodplains is not clearly marked by high FTLE regions as in the previous cases. Furthermore, the presence of JC is not continuous along the stream-wise direction.

6.4 Concluding remarks of the Chapter

This Chapter aims to detect Shear and Shearless Lagrangian Coherent Structures in compound channels. Finite-Time Lyapunov Exponent fields are calculated on the basis of Eulerian velocity fields measured via PIV (Stocchino et al., 2011; Stocchino and Brocchini, 2010) and they unveil the most active regions of the fluid flow from a kinematic point of view. From a methodological perspective, ridges and trenches of FTLE fields are obtained combining the best methods found in literature: algorithm proposed by Mathur et al., 2007, Hermite interpolation by Haller, 2011 (recovered in a simplified version from Rovenski, 2010 owing to a predominant linearity of ridges and trenches along the stream-wise direction), refinement process proposed by Allshouse and Peacock, 2015b. Note that the Eulerian velocity fields were collected during an experimental campaign whereas most applications concern analytical or numerical models. This reinforce the idea that this Lagrangian measure is a robust tool that can be applied to realistic and complex flow fields.

The main parameters controlling the flow under investigation are the depth ratio

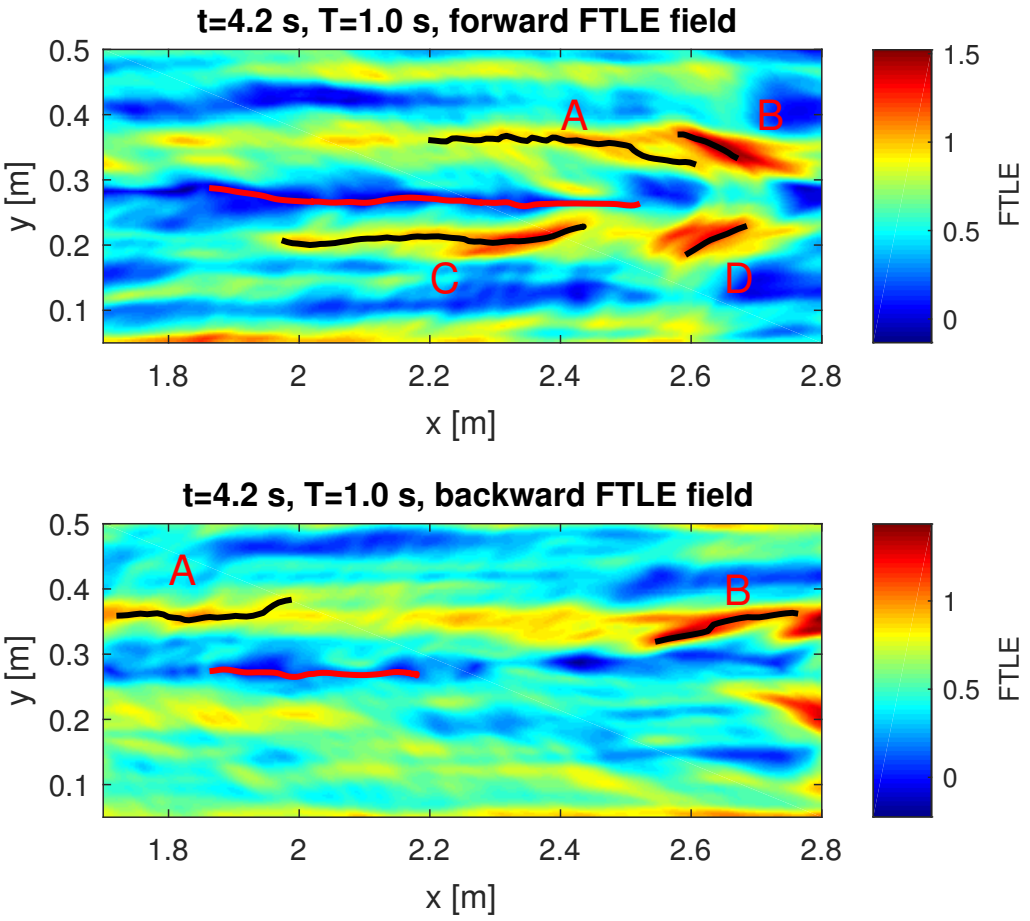

FIGURE 6.27: Forward and backward FTLE ridges for EXP 213, deep flow conditions. Letters identify predominant FTLE ridges. Trenches are marked in red.

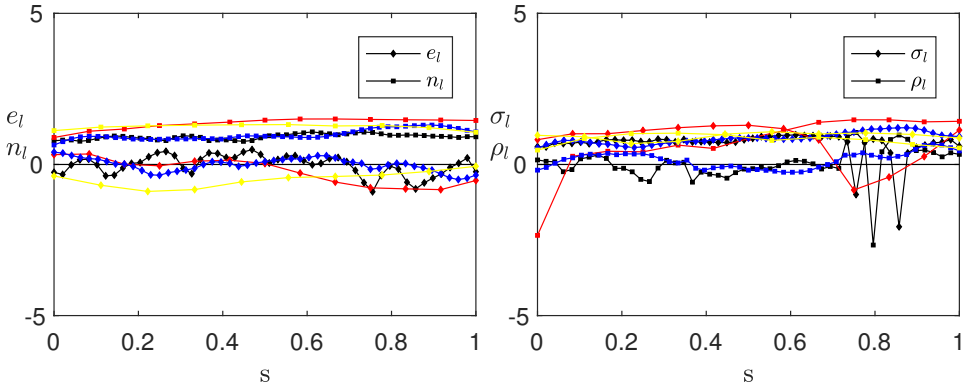

FIGURE 6.28: Forward FTLE ridges normal and tangential advected unit vector magnitudes, e_l and n_l on the left, and hyperbolic repulsion and Lagrangian shear, σ_l and ρ_l on the right. Black, red, blue and yellow colors refer to ridges A, B, C and D of Panel a) of Figure 6.27, respectively. Ridges B and D show hyperobolic repusion and Lagrangian shear of comparable strength.

r_h, i.e. the ratio between the depth of the main channel and the depth of the floodplains, and the Froude number. The first parameter defines the shallowness of the flow whereas the second the critical conditions.

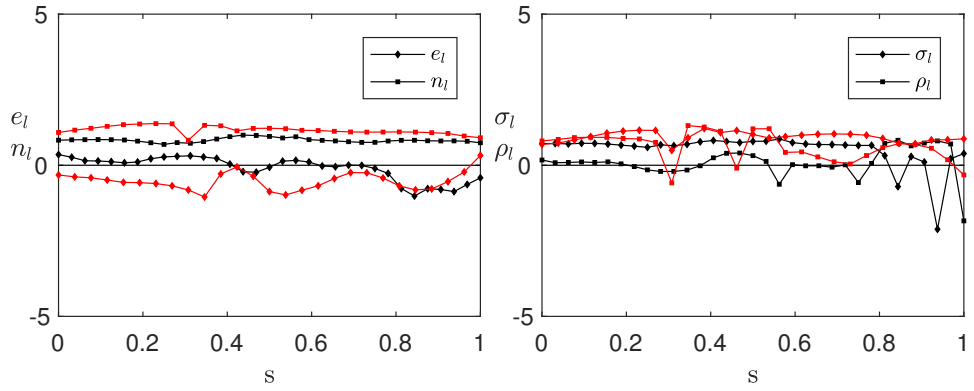

FIGURE 6.29: Backward FTLE ridges normal and tangential advected unit vector magnitudes, e_l and n_l on the left, and hyperbolic repulsion and Lagrangian shear, σ_l and ρ_l on the right. Black and red colors refer to ridges A and B of Panel b) of Figure 6.27, respectively. Ridge B shows hypebolic repulsion and Lagrangian shear of comparable strength.

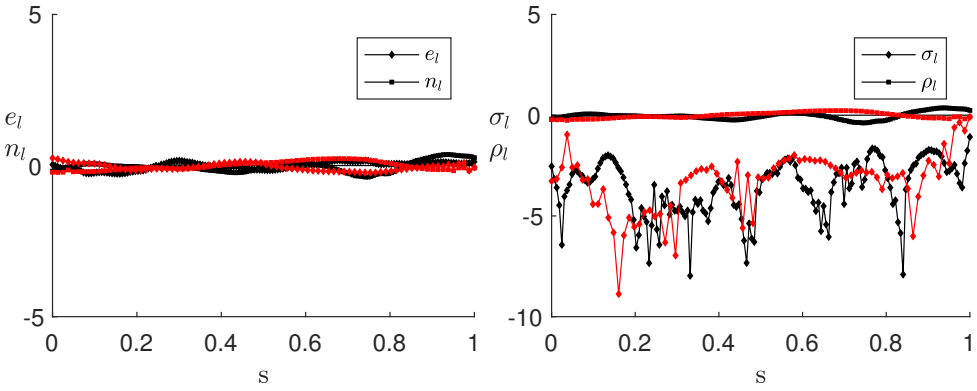

FIGURE 6.30: Quantification of repelling and shear properties of JC. Panel a) shows n_l and e_l for forward and backward trenches of Figure 6.27, in red and black respectively. Panel b) shows ρ_l and σ_l with the same color coding.

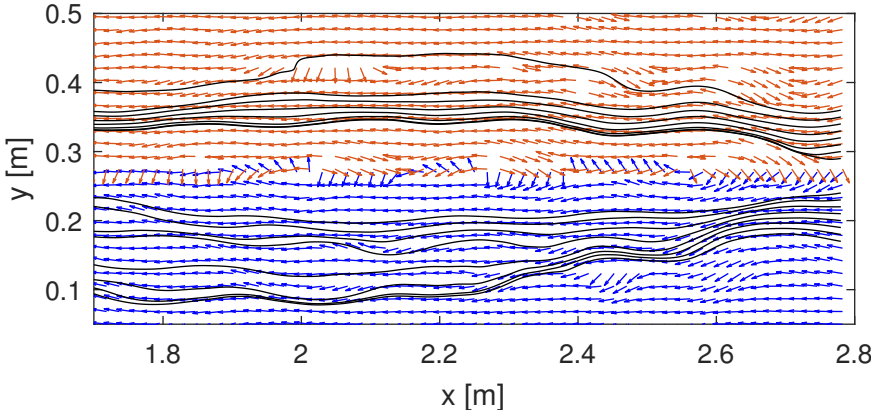

FIGURE 6.31: Positive, in blue, and negative shear vector field, in red. Positive and negative shear LCS are superimposed on the respective fields.

The results suggest a strong influence of the depth ratio on the establishment of persistent Lagrangian patterns, whereas the Froude number do not seem to be an important controlling parameter. However, this dataset does not present supercritical

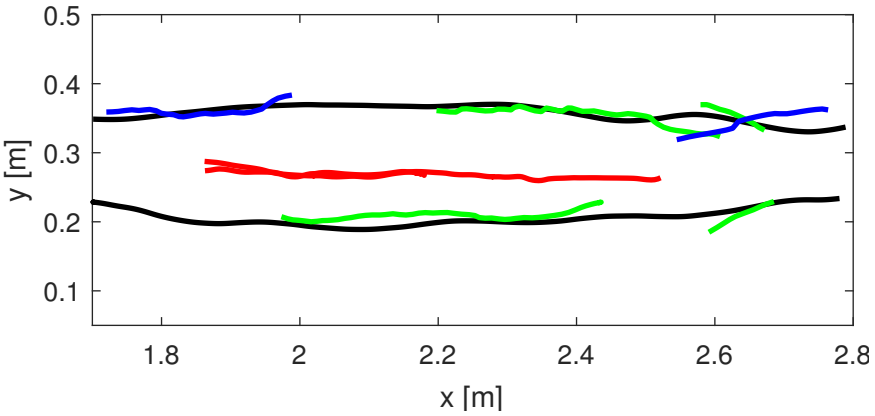

FIGURE 6.32: Predominant positive and negative shearlines, in black, superimposed on forward FTLE field, EXP 213. Forward FTLE ridges in green, backward in blue and JC in red.

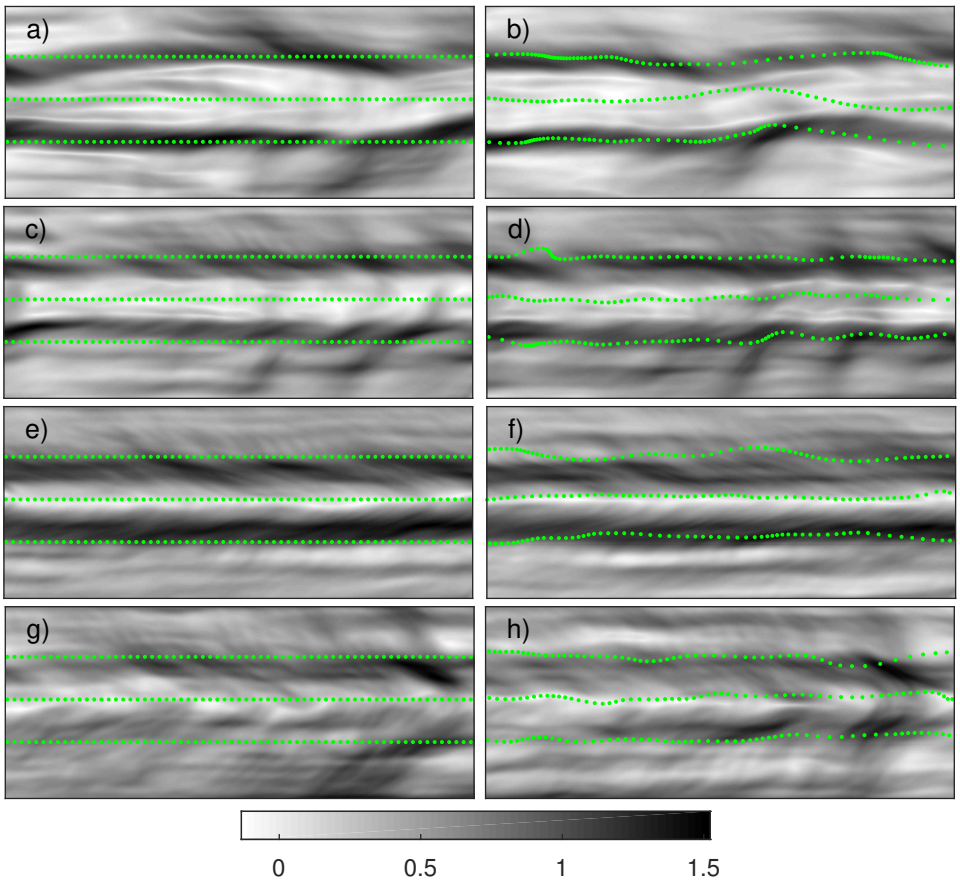

FIGURE 6.33: Advection of particles (green dots) superimposed on corresponding forward FTLE fields. Left panels show initial conditions, right panels final conditions. Panel a) and b) refer to shallow conditions (EXP. 201). Panels c)-f) to intermediate conditions (EXP. 207 and EXP. 105, respectively). Panels g) and h) refer to deep conditions (EXP. 213).

flows for the shallow conditions and the highest Froude number is 1.07 for the intermediate conditions. Therefore, the relevance of these results mainly concerns the influence of the depth ratio.

In shallow flow conditions, FTLE fields show active regions at the transition from

the main channel to the lateral floodplains marked by high FTLE values. Regions of small FTLE values at the center of the main channel are also present. The former are associated with ridges whereas the latter with trenches. Ridges mark Shear Lagrangian Structures that maximize Lagrangian shear and trenches Shearless Lagrangian Structures that behave as Jet-Cores.

Such a configuration is kept even in intermediate conditions. However, it is possible to observe that FTLE ridges protrude more in the floodplains. The analysis performed on the resulting ridges in order to assess whether hyperbolic repulsion or Lagrangian shear are predominant suggests that ridges aligned along the stream-wise direction show predominance of Lagrangian shear over hyperbolic repulsion. On the contrary, ridges that are aligned diagonally with respect to the stream-wise direction show portions of their length where hyperbolic repulsion is predominant over Lagrangian shear.

The clear separation between the main channel and the floodplains shades by decreasing the flow depth ratio and reaching deep flow conditions. As a result, the presence of Shear and Shearless Lagrangian Structures detected from FTLE fields is less readable. It is still possible to recover some features but their persistence is less evident.

The peculiar pattern of shallow and intermediate conditions strongly influences transport as Figure 6.33 exemplifies. Green dots represent tracers advected by the flow. Panels a), c), e) and g) represent initial conditions of particles superimposed on forward FTLE fields. Panels b), d), f) and h) represent final conditions resulting from the advection process superimposed on corresponding forward FTLE fields. Note that, forward FTLE fields are usually associated with repelling structures. However, no repulsion is evident for ridges aligned along the stream-wise direction. Panels a) to f) refer to shallow and intermediate conditions. These clearly show the shear character of ridges at the transition region due to the fact that the initial distance between particles is not kept constant by the advection process. By decreasing r_h the shear character persist but with less strength. Jet-Cores at the centre of the main channel preserve the initial spacing between the particles. Panels g) and h) refer to deep conditions and they show that the shear strength tends to be lost.

This analysis gives an integrated point of view over a finite time interval of the previous work carried out by Stocchino and Brocchini, 2010 and Stocchino et al., 2011. The influence of the Eulerian macrovortices that develop mainly in shallow conditions (cf. Figure 4 of Stocchino et al., 2011) can be directly observed in the meandering pattern that particles show in such a flow (see panel b) of Figure 6.33). However, Eulerian and Lagrangian diagnostics are conceptually different (Haller, 2015) since the former refer to an instantaneous time instance whereas the latter to a finite time interval. Therefore, a direct matching is impossible to reach.

Ridges of FTLE fields marking heuristic SLS conform to rigorous SLS calculated adopting the geodesic theory of transport barriers (Haller and Beron-Vera, 2012).

Such SLS are aligned along the stream-wise direction with a symmetric pattern. Positive SLS are located in the bottom part of the domain and negative SLS are located in the upper part of the domain. However, SLS are always aligned along the stream-wise direction.

Decreasing r_h down to a value typical of deep flow conditions, SLS conform to shallow and intermediate conditions. However, the results should be considered jointly with the fact that FTLE fields are less significant and do not show strong persistent patterns. This fact reflects the different velocity profiles that are recovered in the different depth flow conditions along a cross-section. Figure 2 of Stocchino and Brocchini, 2010 shows that peak velocities in the main channel and in the floodplains are comparable at deep flow conditions.

Therefore, FTLE fields prove to be once again a valuable tool in order to assess the behaviour of a fluid flow giving an immediate understanding of the strength of the mixing pattern and the most active regions of the domain. However, these active areas need to be well characterized by the evaluation of the Lagrangian shear and the hyperbolic repulsion. To further understand the dynamics, SLS are detected in order to depict the shear pattern. The joint analysis of FTLE fields and SLS manage to unveil the mixing pattern thoroughly since the shortcomings of one measure are balanced by strengths of the other. Besides, the presence of JC at the center of the main channel impact on tracer advection. These results are of evident importance in riverine and estuarine analysis since these structures mark regions where particles undergo different fates. For example, evaluation of concentration distributions employed in the advection-diffusion equation must carefully take into account the inhomogeneity resulting from SLS and JC. As a result, turbulent diffusivity can vary on the spatial domain (Besio et al., 2012) especially across regions delimited by SLS and JC. Natural streams or estuaries usually show several regions that adapt to the framework of this work. The presence of analogue structures is quite likely. Therefore, LCS should mark the natural boundaries along which diffusivities could dramatically change their magnitude. Further research is needed to clearly connect the Eulerian properties of the flow with its intrinsic Lagrangian features. Indeed, the compound channel geometry leads to the generation of Eulerian vortical structures, the appearance of which is strongly dependent on the flow depth ratio. The present results suggest that a similar relationship is found when Lagrangian Coherent Structures are studied. A link between the two frameworks based on the spectral properties of Eulerian velocity fields and FTLE fields would then be desirable.

Chapter 7

Conclusions

Considerable efforts have been dedicated in recent years to advance the description of fluid flows adopting the Lagrangian point of view. This Thesis belongs to this field of research. It aims to seek order in what can be seen as chaotic at a first glance: particle trajectories. The objective is to study fluid flows borrowing the crucial concept of separatrices from dynamical system theory. In this way, what emerges from particle trajectories as a whole is structured chaos, i.e. Lagrangian Coherent Structures. LCS are intangible and immaterial but, at the same time, they are also real enough to be treated mathematically. As a result, the domain is divided into regions with different behaviours enhancing our understanding of transport. Usual Lagrangian statistics such as absolute and relative dispersion do not characterize flow inhomogeneity since they provide results that take into account an average behaviour. On the contrary, LCS manage to spatially characterize the inhomogeneity of the flow over finite-time intervals.

In this Thesis two datasets coming from a field campaign and laboratory experiments are taken into account. The former deals with surface velocity fields of the Gulf of Trieste, Italy, measured by coastal radars and drifter trajectories deployed inside the Gulf itself. The latter deals with surface velocity fields of compound channels measured via PIV instrumentation. The main focus of the analysis is on mixing, i.e. dispersion of passive tracers. The privileged point of view is the Lagrangian one because particles are followed during their path. This type of framework carries as a natural consequence the evaluation of the cited Lagrangian statistics. A spatial characterization is indeed needed in order to detect directions along which transport is likely to develop. As a result, the role of flow inhomogeneity must not be disregarded. This Thesis considers this role and shows how important it is to define the behaviour of transport phenomena adopting this perspective. In particular, Chapter 4 takes into account usual Lagrangian statistics in the Gulf of Trieste. Besides, a comparison between Eulerian and Lagrangian velocities is carried out. Spatial inhomogeneity in

the same semi-enclosed basin is considered in Chapter 5 where LCS are calculated and compared with drifter trajectories. Chapter 6 is devoted to the analysis of LCS in compound channels. The main results of this work are summarized in the following:

- Lagrangian statistics are evaluated in the Gulf of Trieste over surface velocity fields recorded by coastal radars. Absolute and relative statistics are evaluated and compared with theoretical trends in order to characterize the average behaviour of the Gulf during the finite-time interval covered by the available dataset;
- reliability of velocity fields measured by coastal radars is assessed carrying out a comparison between Eulerian velocities of the measured field and Lagrangian velocities of drifters. Besides, separations between observed and simulated drifter trajectories are computed and the results are comprised within the range usually accepted in literature;
- heuristic LCS are evaluated in the Gulf of Trieste both as finite-time and finite-size Lyapunov exponents and their resemblance is characterized by the correlation coefficient;
- observed and simulated trajectories of drifters are compared with LCS strengthening the idea that LCS characterize transport;
- LCS are evaluated as tensorlines of the Cauchy-Green tensor and a search strategy joining the traditional approach based on particle trajectories and LCS is proposed;
- LCS are detected over surface velocity fields of compound channels. In particular, two types of structures are detected. Shear and shearless structures are evaluated as ridges and trenches of FTLE fields, respectively. Besides, Shear Lagrangian Structures are detected as shearlines that minimize their geodesic deviation. All these structures characterize compound channel flows and are for the first time detected on the basis of experimental velocity fields.

This work was presented in several national and international conferences. Besides, two manuscripts describing the results achieved are currently under review in international journals. These contributions are listed in the following.

- Peer-reviewed journals:
  - Enrile F., Besio G., Stocchino A., Magaldi M., Mantovani C., Cosoli S., Gerin R., Poulain P.M., Surface Lagrangian barriers in the Gulf of Trieste, submitted to Continental Shelf Research and under review.
  - Enrile F., Besio G., Stocchino A., Shear and Shearless Lagrangian Structures in compound channels, submitted to Advances in Water Resources and accepted.

- International Conferences:
  - Enrile F., Besio G., Magaldi M., Mantovani C., Cosoli S., Gerin R., Poulain P.M., Lagrangian Coherent Structures deduced from HF-radar measurements, OCEANS 2015 - Genova, Italy, 18-21 May 2015
  - Besio G., Enrile F., Magaldi M., Mantovani C., Cosoli S., Gerin R., Poulain P.M., Reliability of LCS detection depending on HF- radar velocity dataset, Ocean Science Meeting 2014, Honolulu, Hawaii, USA, 23-28 February 2014.
  - Besio G., Enrile F., Magaldi M., Mantovani C., Cosoli S., Gerin R., Poulain P.M., Lagrangian Coherent Structures in the Trieste Gulf, Abstract OS21C-06, 1 pp., AGU Fall Meeting 2013, San Francisco, California, 9-13 December 2013.
- National Conferences:
  - Enrile F., Boi S., Lagomarsino Oneto D., Besio G., Magaldi M.G., Mazzino A., Stocchino A., Lagrangian simulations of drifter trajectories adopting a new explicit expression for eddy diffusivities, XXXV Convegno Nazionale di Idraulica e Costruzioni Idrauliche, 15-16 September 2016, Bologna, Italy.
  - Enrile F., Besio G., Magaldi M., Mantovani C., Cosoli S., Gerin R. Poulain P.M., Barriere Lagrangiane superficiali nel Golfo di Trieste (Surface Lagrangian barriers in the Trieste Gulf), Abstract 0262, XXXIV Convegno Nazionale di Idraulica e Costruzioni Idrauliche, 8-10 September 2014, Bari, Italy.

Appendix A

Derivation of vector fields

This Appendix is devoted to the derivation of squeezelines, strechlines and shearlines tangents field. This derivation was laid by the seminal works of Haller (2011) and Haller and Beron-Vera (2013). A comprehensive review and a detailed account of sensitivity of hyperbolic repulsion and Lagrangian shear can be found in Allshouse (2013).

A.1 Squeezlines and strechlines

Let the unit tangent vector to a material line be a generic combination of the orthogonal eigenvectors of the Cauchy-Green tensor.

$$\boldsymbol{\tau_0} = \alpha \boldsymbol{e_1} + \beta \boldsymbol{e_2} \tag{A.1}$$

where

$$\alpha^2 + \beta^2 = 1 \tag{A.2}$$

Therefore the normal vector is

$$\boldsymbol{n_0} = \boldsymbol{\Omega \tau_0} = \alpha \boldsymbol{e_2} - \beta \boldsymbol{e_1} \tag{A.3}$$

where

$$\boldsymbol{\Omega} = \begin{bmatrix} 0 & -1 \\ 1 & 0 \end{bmatrix} \tag{A.4}$$

A generic point $\boldsymbol{x_0}$ on the material line is advected to the point $\boldsymbol{x_t} = \boldsymbol{\Phi}(t; t_0, \boldsymbol{x_0})$. For this new point the tangential and normal vectors are $\boldsymbol{\tau_t}$ and $\boldsymbol{n_t}$, respectively.

Despite a probable change in length, $\nabla \boldsymbol{\Phi \tau_0}$ is still tangent to the material line advected at time t. It is thus possible to represent the tangent vector at time t in

terms of the initial tangent vector as:

$$\boldsymbol{\tau_t} = \frac{\nabla \boldsymbol{\Phi} \boldsymbol{\tau_0}}{|\nabla \boldsymbol{\Phi} \boldsymbol{\tau_0}|} \tag{A.5}$$

Therefore, it is also possible to express even the unit normal vector at time t as

$$\boldsymbol{n_t} = \boldsymbol{\Omega} \frac{\nabla \boldsymbol{\Phi} \boldsymbol{\tau_0}}{|\nabla \boldsymbol{\Phi} \boldsymbol{\tau_0}|} \tag{A.6}$$

The hyperbolic repulsion, largely evaluated in Chapter 5 for compound channels, can be written as

$$\rho = [\boldsymbol{n_t} \cdot (\nabla \boldsymbol{\Phi} \boldsymbol{n_0})] = \frac{1}{\sqrt{[\boldsymbol{\Omega \tau_0} \cdot (\boldsymbol{C}^{-1} \boldsymbol{\Omega \tau_0})]}} \tag{A.7}$$

It is possible to evaluate $\boldsymbol{C}^{-1} \boldsymbol{\Omega \tau_0}$ using the singular value decomposition of $\boldsymbol{C}^{-1}$, recalling that $\boldsymbol{C}^{-1} \boldsymbol{C} = \boldsymbol{I}$. As a result

$$\boldsymbol{C}^{-1} = \boldsymbol{V} \Sigma^{-1} \boldsymbol{V}^T = \begin{bmatrix} \boldsymbol{e_1} \boldsymbol{e_2} \end{bmatrix} \begin{bmatrix} \lambda_1^{-1} & 0 \\ 0 & \lambda_2^{-1} \end{bmatrix} \begin{bmatrix} \boldsymbol{e_1}^T \\ \boldsymbol{e_2}^T \end{bmatrix} \tag{A.8}$$

The right-hand side of the inner product in equation A.7 can be written as

$$\begin{aligned} \boldsymbol{C}^{-1} \boldsymbol{n_0} &= \begin{bmatrix} \boldsymbol{e_1} \boldsymbol{e_2} \end{bmatrix} \begin{bmatrix} \lambda_1^{-1} & 0 \\ 0 & \lambda_2^{-1} \end{bmatrix} \begin{bmatrix} \boldsymbol{e_1}^T \\ \boldsymbol{e_2}^T \end{bmatrix} (\alpha \boldsymbol{e_2} - \beta \boldsymbol{e_1}) = \\ &= \begin{bmatrix} \boldsymbol{e_1} \boldsymbol{e_2} \end{bmatrix} \begin{bmatrix} \lambda_1^{-1} & 0 \\ 0 & \lambda_2^{-1} \end{bmatrix} \begin{bmatrix} -\beta \\ \alpha \end{bmatrix} = \\ &= \begin{bmatrix} \boldsymbol{e_1} \boldsymbol{e_2} \end{bmatrix} \begin{bmatrix} -\beta \lambda_1^{-1} & 0 \\ 0 & \alpha \lambda_2^{-1} \end{bmatrix} = \\ &= -\frac{\beta}{\lambda_1} \boldsymbol{e_1} + \frac{\alpha}{\lambda_2} \boldsymbol{e_2} \end{aligned} \tag{A.9}$$

Therefore, the inner product of equation A.7 can be recast to obtain

$$\boldsymbol{\Omega \tau_0} \cdot (\boldsymbol{C}^{-1} \boldsymbol{\Omega \tau_0}) = (\alpha \boldsymbol{e_2} - \beta \boldsymbol{e_1}) \cdot (-\frac{\beta}{\lambda_1} \boldsymbol{e_1} + \frac{\alpha}{\lambda_2} \boldsymbol{e_2}) = \frac{\alpha^2}{\lambda_2} + \frac{\beta^2}{\lambda_1} \tag{A.10}$$

which leads to

$$\rho = \left[\frac{\alpha^2}{\lambda_2} + \frac{\beta^2}{\lambda_1} \right]^{-1/2} \tag{A.11}$$

Recalling equation A.2

$$\rho = \left[\alpha^2 \left(\frac{1}{\lambda_2} - \frac{1}{\lambda_1} \right) + \frac{1}{\lambda_1} \right]^{-1/2} = \left[\beta^2 \left(\frac{1}{\lambda_1} - \frac{1}{\lambda_2} \right) + \frac{1}{\lambda_2} \right]^{-1/2} \tag{A.12}$$

To find the components (α, β) which maximize ρ, we take the derivatives of the hyperbolic repulsion with respect to α and β.

$$\begin{aligned}\frac{d\rho}{d\alpha} &= \frac{\alpha(\lambda_2^{-1} - \lambda_1^{-1})}{\alpha(\lambda_2^{-1} - \lambda_1^{-1}) + \lambda_1^{-1}} \\ \frac{d\rho}{d\beta} &= \frac{\beta(\lambda_1^{-1} - \lambda_2^{-1})}{\alpha(\lambda_1^{-1} - \lambda_2^{-1}) + \lambda_2^{-1}}\end{aligned} \tag{A.13}$$

The local extrema are obtained for the combinations $(\alpha, \beta) = (1, 0)$ and $(0, 1)$. Substitution into the expression for ρ leads to $\rho = \frac{1}{\lambda_2}$ and $\rho = \frac{1}{\lambda_1}$, respectively. Since $\lambda_1 < \lambda_2$, ρ is maximized when $\boldsymbol{\tau_0} = \boldsymbol{e_1}$ which is the definition for squeezelines (Olascoaga et al., 2013). Besides, it is possible to note that ρ is minimized when $\boldsymbol{\tau_0} = \boldsymbol{e_2}$ which is the definition of stretchlines.

A.2 Shearlines

The derivation is analogue to the previous one. The Lagrangian shear can be written as

$$\begin{aligned}\sigma = [\boldsymbol{\tau_t} \cdot (\nabla \boldsymbol{\Phi} \boldsymbol{n_0})] &= \frac{\nabla \boldsymbol{\Phi} \boldsymbol{\tau_0}}{|\nabla \boldsymbol{\Phi} \boldsymbol{\tau_0}|} \cdot \nabla \boldsymbol{\Phi} \boldsymbol{n_0} = \\ &= \frac{1}{|\nabla \boldsymbol{\Phi} \boldsymbol{\tau_0}|} (\nabla \boldsymbol{\Phi} \boldsymbol{\tau_0} \cdot \nabla \boldsymbol{\Phi} \boldsymbol{n_0}) = \\ &= \frac{1}{|\nabla \boldsymbol{\Phi} \boldsymbol{\tau_0}|} (\boldsymbol{\tau_0} \cdot \boldsymbol{C} \boldsymbol{n_0}) = \\ &= \frac{1}{|\nabla \boldsymbol{\Phi} \boldsymbol{\tau_0}|} (\boldsymbol{\Omega} \boldsymbol{\tau_0} \cdot \boldsymbol{C} \boldsymbol{\tau_0})\end{aligned} \tag{A.14}$$

The denominator can be recast as

$$\begin{aligned}|\nabla \boldsymbol{\Phi} \boldsymbol{\tau_0}| &= \sqrt{\nabla \boldsymbol{\Phi} \boldsymbol{\tau_0} \cdot \nabla \boldsymbol{\Phi} \boldsymbol{\tau_0}} \\ &= \sqrt{\boldsymbol{\tau_0} \cdot \boldsymbol{C} \boldsymbol{\tau_0}}\end{aligned} \tag{A.15}$$

As a result the Lagrangian shear can be written as

$$\sigma = \frac{\boldsymbol{\Omega} \boldsymbol{\tau_0} \cdot \boldsymbol{C} \boldsymbol{\tau_0}}{\sqrt{\boldsymbol{\tau_0} \cdot \boldsymbol{C} \boldsymbol{\tau_0}}} = \frac{\alpha\beta(\lambda_2 - \lambda_1)}{\sqrt{\alpha^2 \lambda_1 + \beta^2 \lambda_2}} \tag{A.16}$$

Partial derivation of σ with respect to α and β leads to:

$$\begin{aligned}\frac{\partial \sigma}{\partial \alpha} &= \frac{\beta^3 \lambda_2 (\lambda_2 - \lambda_1)}{(\alpha^2 \lambda_1 + \beta^2 \lambda_2)^{3/2}} \\ \frac{\partial \sigma}{\partial \beta} &= \frac{\alpha^3 \lambda_1 (\lambda_1 - \lambda_2)}{(\alpha^2 \lambda_1 + \beta^2 \lambda_2)^{3/2}}\end{aligned} \tag{A.17}$$

The objective is to find the values of α and β that maximize σ given the constraint of equation A.2. The solution can be found applying the method of Lagrangian multipliers. Given the base equation

$$\Lambda(x, y, \lambda) = f(x, y) + \lambda(g(x, y) - c) \tag{A.18}$$

where λ is the multipliers, the values that maximize $f(x, y)$ while satisfying the constraint $g(x, y) = c$ must solve

$$\nabla_{x,y,\lambda}\Lambda(x, y, \lambda) = 0 \tag{A.19}$$

In this case

$$\begin{aligned} \frac{\partial\Lambda}{\partial\alpha} &= \frac{\partial\sigma}{\partial\alpha} + 2\lambda\alpha = 0 \\ \frac{\partial\Lambda}{\partial\beta} &= \frac{\partial\sigma}{\partial\beta} + 2\lambda\beta = 0 \end{aligned} \tag{A.20}$$

Therefore

$$-\lambda = \frac{1}{2\alpha}\frac{\partial\sigma}{\partial\alpha} = \frac{1}{2\beta}\frac{\partial\sigma}{\partial\beta} \tag{A.21}$$

This leads to

$$\frac{\alpha}{\beta} = \frac{\frac{\partial\sigma}{\partial\alpha}}{\frac{\partial\sigma}{\partial\beta}} = \pm\left(\frac{\lambda_2}{\lambda_1}\right)^{1/4} \tag{A.22}$$

Substituting this result into equation A.2, it is possible to obtain:

$$\begin{aligned} \alpha^2 + \alpha^2\left(\frac{\lambda_2}{\lambda_1}\right)^{1/2} &= 1 \\ \beta^2\left(\frac{\lambda_2}{\lambda_1}\right)^{1/2} + \beta^2 &= 1 \end{aligned} \tag{A.23}$$

The tangent vector field is then

$$\boldsymbol{\eta}_{\pm} = \sqrt{\frac{\sqrt{\lambda_2}}{\sqrt{\lambda_1}+\sqrt{\lambda_2}}}\boldsymbol{e}_1 \pm \sqrt{\frac{\sqrt{\lambda_1}}{\sqrt{\lambda_1}+\sqrt{\lambda_2}}}\boldsymbol{e}_2 \tag{A.24}$$

where the convention is that $\boldsymbol{e_2} = \boldsymbol{\Omega e_1}$. $\boldsymbol{\eta}_+$ and $\boldsymbol{\eta}_-$ correspond to the local directions that maximize clockwise and counterclockwise Lagrangian shear in the local coordinate frame, respectively.

A.3 Geodesic LCS

Let's consider a material line γ_0 and advect it in forward time. The length of this line at the end of the advection can be written as:

$$l_{t_0}^{t_+T}(\gamma_0) = \int_{\gamma_t} |d\boldsymbol{x}| = \int_{\gamma_0} \sqrt{\boldsymbol{r'}\cdot\boldsymbol{C}\boldsymbol{r'}} \tag{A.25}$$

where $\boldsymbol{r'}$ is the tangent to the curve γ_0 at $\boldsymbol{r}$ and γ_t is the adveted line. This equation reveals the Riemannian metric:

$$\boldsymbol{L}(\boldsymbol{r}, \boldsymbol{r'}) = \frac{1}{2}\boldsymbol{r'} \cdot \boldsymbol{C}\boldsymbol{r'} \tag{A.26}$$

A geodesic is the shortest path between two points in a given space. Transport barriers are defined by Haller and Beron-Vera, 2013 as geodesics of the space deformed by the mapping $\boldsymbol{\Phi}_{t_0}^{t_0+T}$. In Euclidean space the geodesics are straight lines. As a result, the inverse mapping $\boldsymbol{\Phi}_{t_0+T}^{t_0}$ of any straight line connecting two points at time $t_0 + T$ is a geodesic connecting those points under the Cauchy-Green metric. Therefore, there is the need to identify geodesics with particular characteristics. Unlike in classic calculus of variations endpoints are a priori unknown. Haller and Beron-Vera (2013) solve the problem by considering as boundary conditions tangents at the endpoints. By adopting a variational argument, they prove that tensorlines and $\boldsymbol{\eta}_{\pm}$ curves are geodesics under the Cauchy-Green metric.

Appendix B

Comparison Lagrangian - Eulerian velocities

This Appendix contains all the comparisons between Lagrangian velocities of CODE drifters and Eulerian velocities of the measured field, interpolated upon necessity. Such comparisons are here depicted in order to let the Thesis be more fluent and readable. Such comparisons are exploited in Chapter 3 where a detailed summary is present in Figure 4.19.

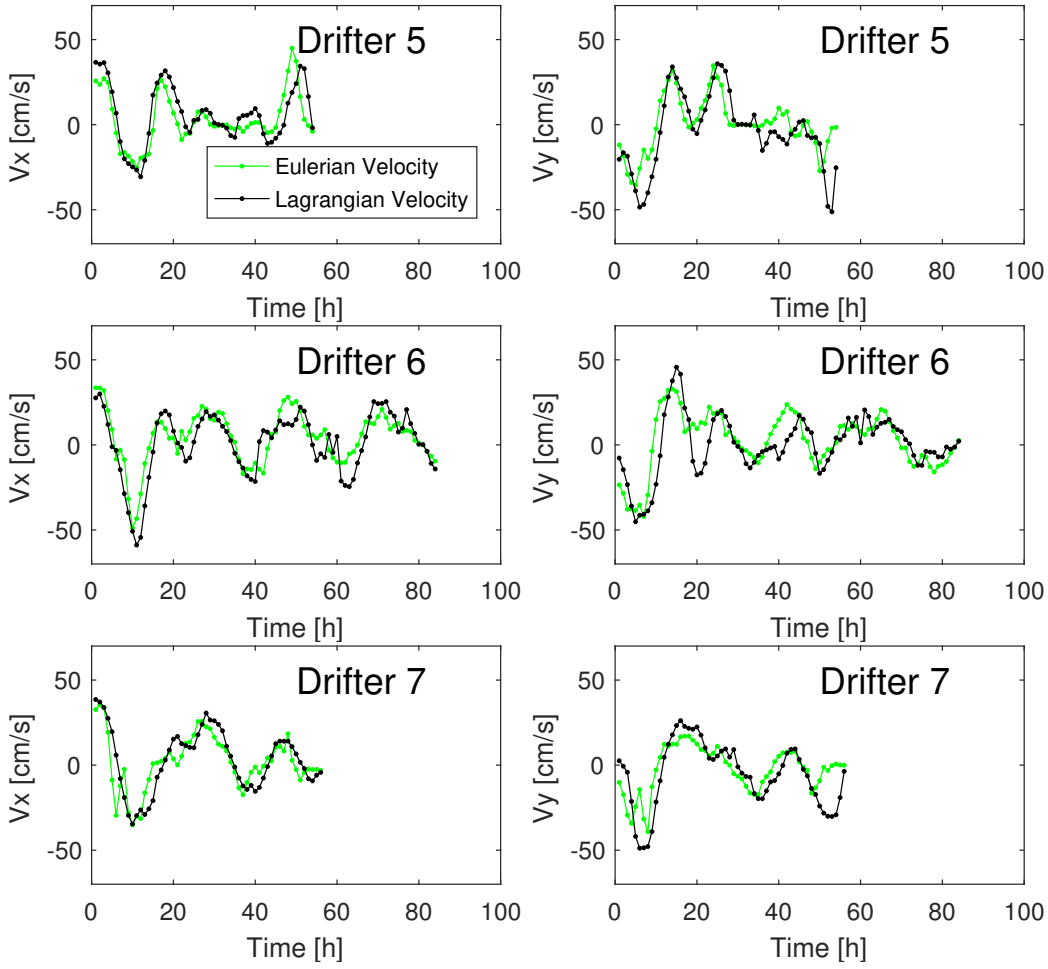

FIGURE B.1: Lagrangian and Eulerian velocity comparisons.

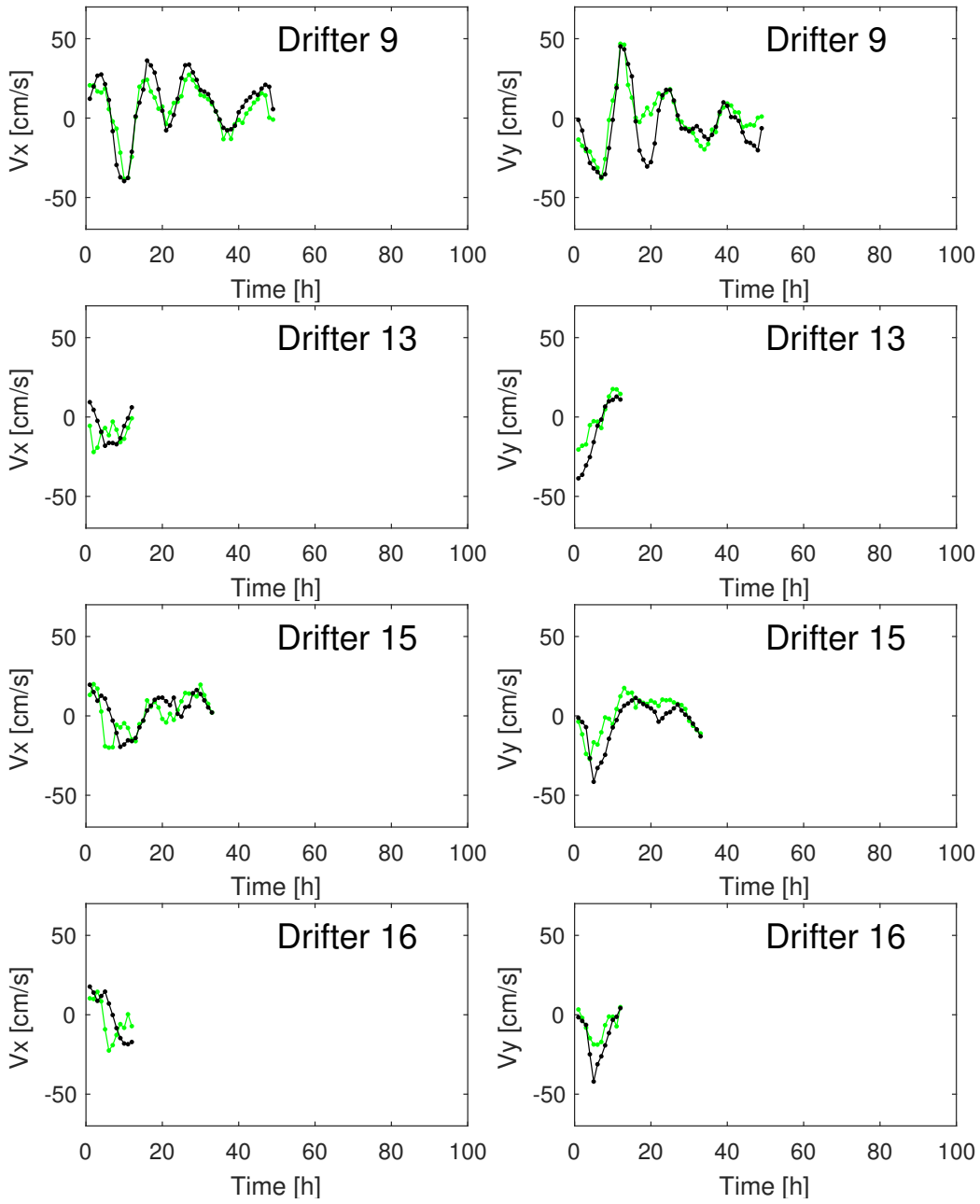

FIGURE B.1: Lagrangian and Eulerian velocity comparisons.

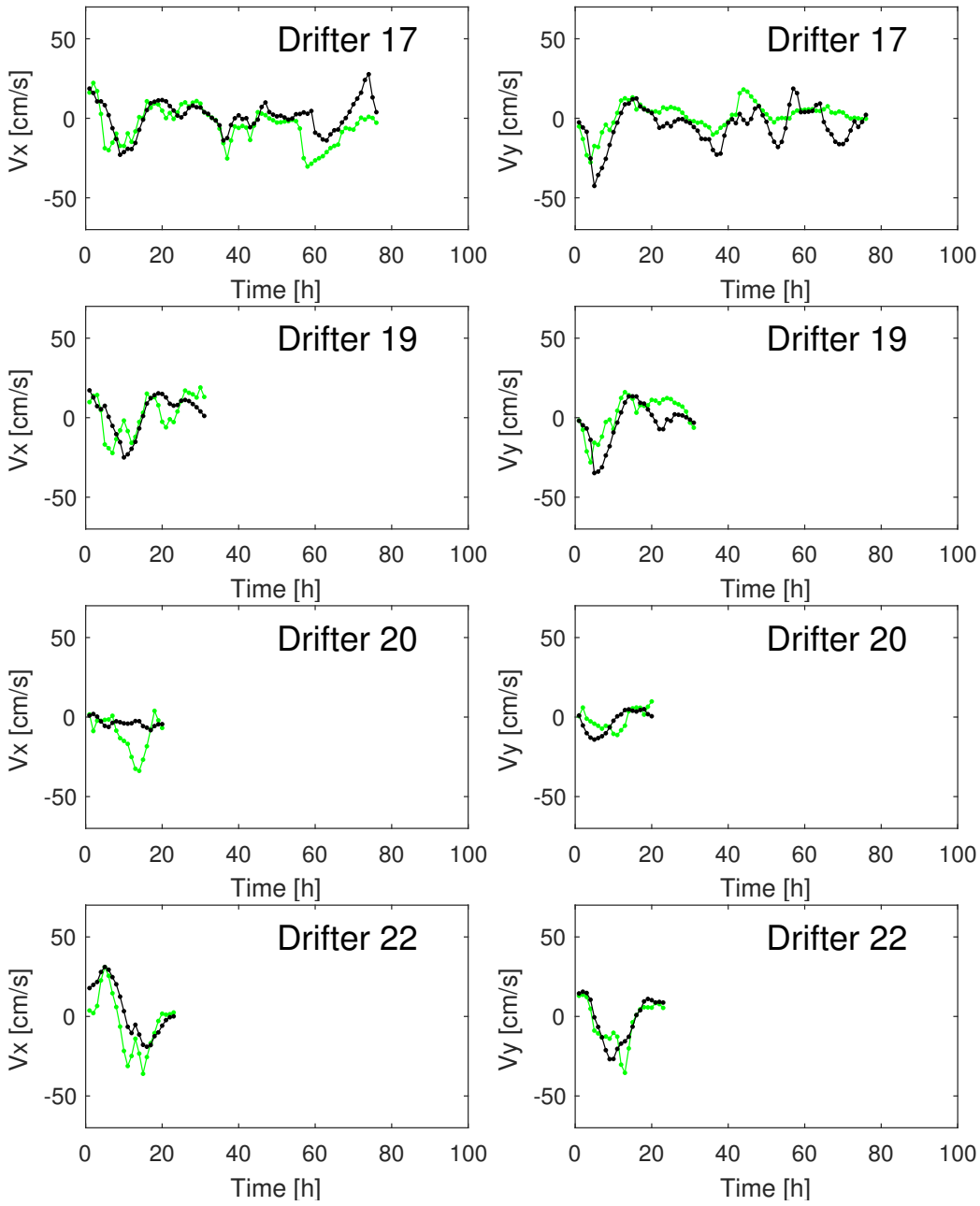

FIGURE B.1: Lagrangian and Eulerian velocity comparisons.

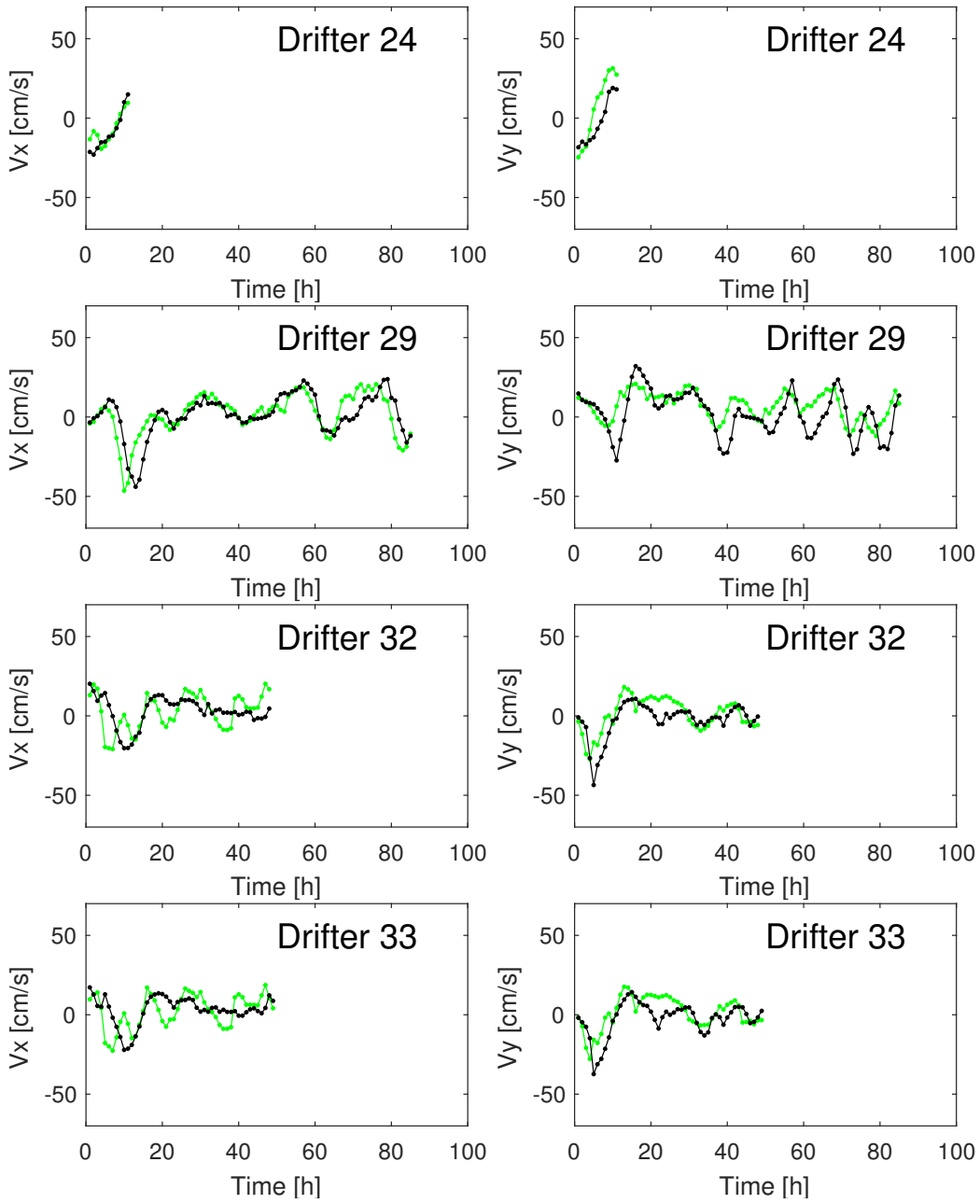

FIGURE B.1: Lagrangian and Eulerian velocity comparisons.

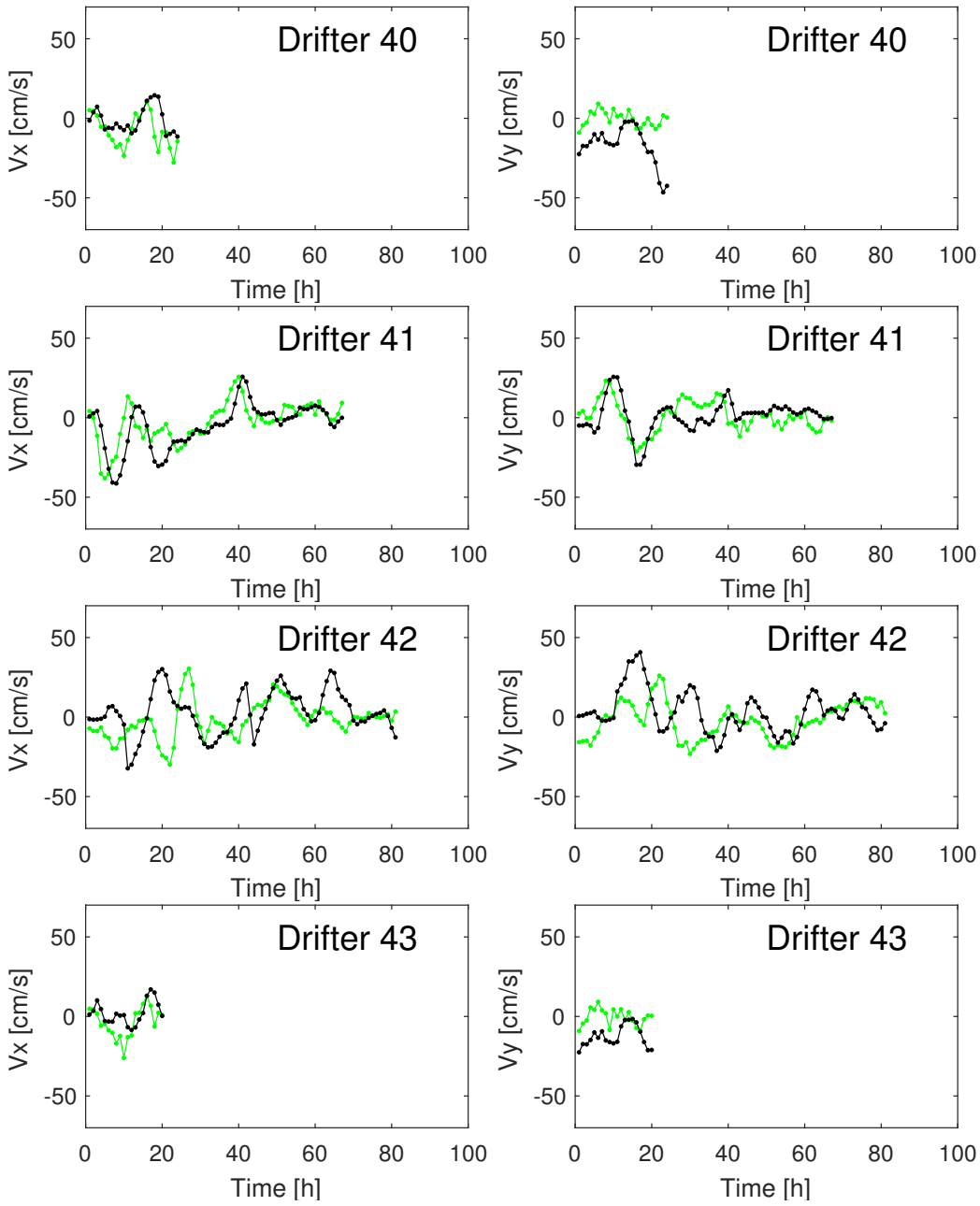

FIGURE B.1: Lagrangian and Eulerian velocity comparisons.

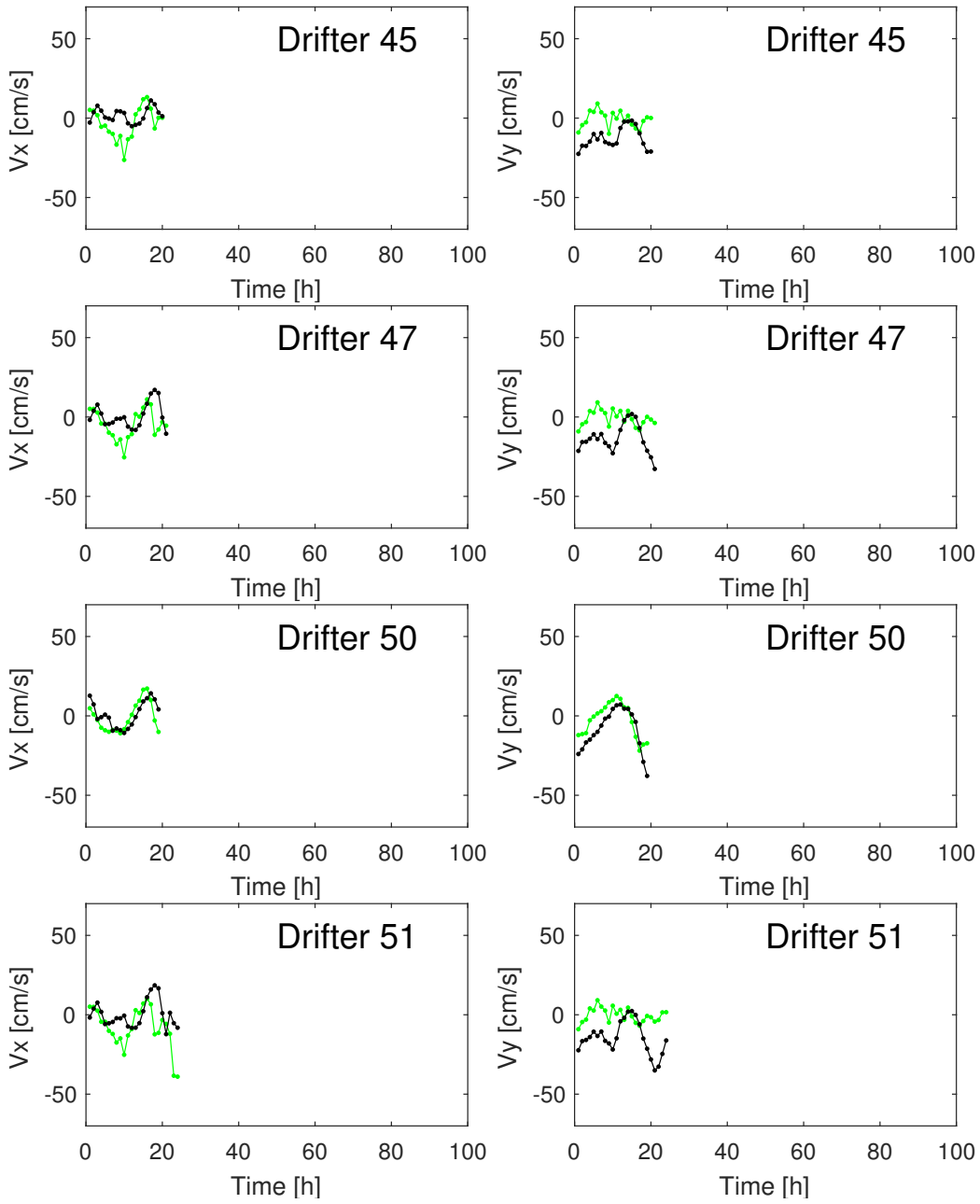

FIGURE B.1: Lagrangian and Eulerian velocity comparisons.

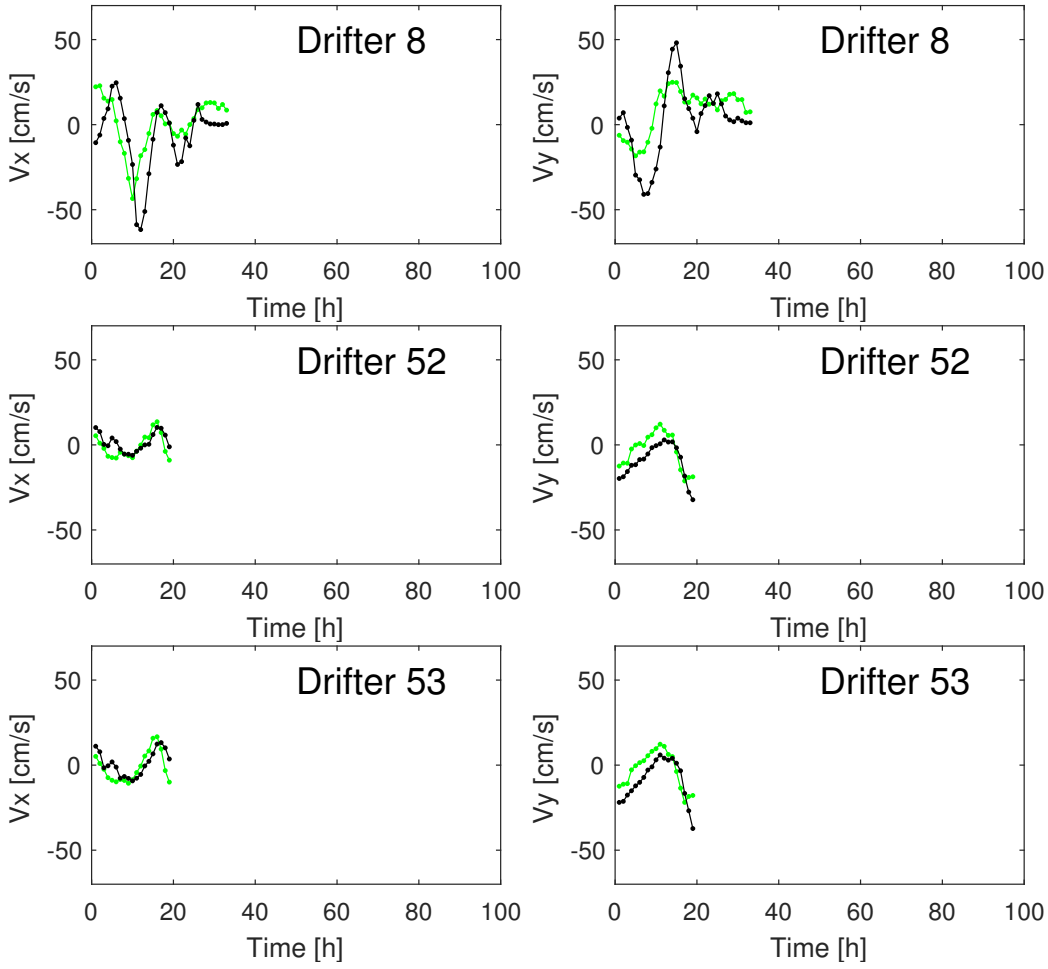

FIGURE B.1: Lagrangian and Eulerian velocity comparisons.

Bibliography

Abraham, Edward R. and Melissa M. Bowen (2002). “Chaotic stirring by a mesoscale surface ocean-flow”. In: *Chaos* 12.2, pp. 373–381.

Adrian, R.J., K.T. Christensen, and Z.C. Liu (2000). “Analysis and interpretation of istantaneous turbulent velocity fields”. In: *Exp. in Fluids* 29, pp. 275–290.

Allshouse, M. R. and T. Peacock (2015a). “Lagrangian based methods for coherent structures detection”. In: *Chaos* 25.9.

Allshouse, Michael R. (2013). “Detectiong and Analyzing Coherent Structures in Two-Dimensional Dynamical Systems”. PhD thesis. Massachusetts Institute of Technology.

Allshouse, Michael R. and Thomas Peacock (2015b). “Refining finite-time Lyapunov exponent ridges and the challenges of classifying them”. In: *Chaos* 25.8, 087410.

Alvera-Azcárate, A. et al. (2009). “Enhancing temporal correlations in EOF expansionsfor the reconstruction of missing data using DINEOF”. In: *Ocean Science* 5, pp. 5 –11.

Alvera-Azcárate, A. et al. (2011). “Data Interpolating Empirical Orthogonal Functions (DINEOF): a tool for geophysical data analysis”. In: *Mediterranean Marine Science* 12.

Aris, Rutherford (1962). *Vectors, Tensors, and the Basic Equations of Fluid Mechanics*. Englewood Cliffs, New Jersey: Prentice-Hall.

Arnol’d, Vladimir Igorevich (1992). *Ordinary differential equations*. Springer.

Artale, V. et al. (1997). “Dispersion of passive tracers in close basins: beyond the diffusion coefficient”. In: *Physics of Fluids* 9.11, pp. 3162–3171.

Bae, Jae Seok, Sung Bum Yoon, and Junwoo Choi (2013). “Boussinesq modelling of a rip current at Haeundae Beach in South Korea”. In: *Journal of Coastal Research*, pp. 654–659.

Banerjee, Santo and Lamberto Rondoni (2015). *Applications of Chaos and Nonlinear Dynamics in Science and Engineering-Vol. 4*. Springer.

Barrick, D. E. and B.J. Lipa (1986). “An evaluation of least-squares and closed-form dual-angle methods for CODAR surface-current applications”. In: *IEEE Journal of Oceanic Engineering* 11, pp. 322 –326.

Bauer, S., M.S. Swenson, and A. Griffa (2002). "Eddy mean flow decomposition and eddy diffusivity estimates in the tropical Pacific Ocean: 2. Results". In: *Journal of Geophisical Research Oceans* 107, p. C103154.

Bellomo, L. et al. (2015). "Toward an integrated HF radar network in the Mediterranean Sea to improve search and rescue and oil spill response: the TOSCA project experience". In: *Journal of Operational Oceanography* 8.2, pp. 95–107. DOI: 10.1080/1755876X.2015.1087184.

Beron-Vera, Francisco J et al. (2010). "Invariant-tori-like Lagrangian coherent structures in geophysical flows". In: *Chaos: An Interdisciplinary Journal of Nonlinear Science* 20.1, p. 017514.

Berta, M. et al. (2014). "Surface transport in the Northeastern Adriatic Sea from FSLE analysis of HF-Radar measurements". In: *Continental Shelf Research* 77, pp. 14–23.

Besio, G. et al. (2012). "Transversal and longitudinal mixing in compound channels". In: *Water Resources Research* 48.12, n/a–n/a. ISSN: 1944-7973. DOI: 10.1029/2012WR012316.

Boffetta, G. et al. (2001). "Detecting barriers to transport: a review of different techniques". In: *Physica D* 159, pp. 58–70.

Boozer, A. H. (1992). "Dissipation of magnetic energy in the solar corona". In: *Astrophysical Journal* 394.1, pp. 357–362.

Breivik, Øyvind and Arthur A. Allen (2008). "An operational search and rescue model for the Norwegian Sea and the North Sea". In: *Journal of Marine Systems* 69.1–2, pp. 99 –113.

Brown, Garry L. and Anatol Roshko (1974). "On density effects and large structure in turbulent mixing layers". In: *Journal of Fluid Mechanics* 64.4, pp. 775–816. DOI: 10.1017/S002211207400190X.

Chapman, R. D. et al. (1997). "On the accuracy of HF radar surface current measurements: Intercomparisons with ship-based sensors". In: *Journal of Geophysical Research: Oceans* 102.C8, pp. 18737–18748. ISSN: 2156-2202.

Chrisohoides, Antonis, Fotis Sotiropoulos, and Terry W Sturm (2003). "Coherent structures in flat-bed abutment flow: Computational fluid dynamics simulations and experiments". In: *Journal of Hydraulic Engineering* 129.3, pp. 177–186.

Cosoli, Simone et al. (2013). "Surface circulation in the Gulf of Trieste (northern Adriatic Sea) from radar, model, and ADCP comparisons". In: *Journal of Geophysical Research: Oceans* 118.11, pp. 6183–6200.

Crombie, D.D. (1955). "Doppler spectrum of sea echo at 13.56 Mc/s." In: *Nature* 175, pp. 681–682.

Davis, R.E. (1985). "Drifter Observations of Coastal Surface Currents During CODE: The Method and Descriptive View". In: *Journal of Geophysical Research* 90, pp. 4741 –4755.

Deltares (2014). *Delft3D Flow User Manual*.

Dracos, T., M. Giger, and G. H. Jirka (1992). "Plane turbulent jets in a bounded fluid layer". In: *Journal of Fluid Mechanics* 241, pp. 587–614.

Eckmann, J. P. and D. Ruelle (1985). "Ergodic theory of chaos and strange attractors". In: *Rev. Mod. Phys.* 57 (3), pp. 617–656.

Falco, P. et al. (2000). "Transport Properties in the Adriatic Sea as Deduced from Drifter Data". In: *Journal of Physical Oceanography* 30, pp. 2055–2017.

Farazmand, Mohammad, Daniel Blazevski, and George Haller (2014). "Shearless transport barriers in unsteady two-dimensional flows and maps". In: *Physica D: Nonlinear Phenomena* 278, pp. 44–57.

Farazmand, Mohammad and George Haller (2012). "Computing Lagrangian coherent structures from their variational theory". In: *Chaos: An Interdisciplinary Journal of Nonlinear Science* 22.1, p. 013128.

— (2013). "Attracting and repelling Lagrangian coherent structures from a single computation". In: *Chaos: An Interdisciplinary Journal of Nonlinear Science* 23.2, p. 023101.

Fischer, H.B. et al. (1979). *Mixing in inland and coastal waters*. Ed. by Academic Press. Academic Press. ISBN: 9780122581502.

Fyrillas, Marios M and Keiko K Nomura (2007). "Diffusion and Brownian motion in Lagrangian coordinates". In: *The Journal of chemical physics* 126.16, p. 164510.

Green, M. A., C. W. Rowley, and G. Haller (2007). "Detection of Lagrangian Coherent Structures in Three-Dimensional Turbulence". In: *Journal of Fluid Mechanics* 572.-1, pp. 111–120. DOI: 10.1017/S0022112006003648.

Griffies, Stephen M. et al. (2000). "Developments in ocean climate modelling". In: *Ocean Modelling* 2.3–4, pp. 123 –192.

Guala, M. et al. (2007). "An experimental investigation on Lagrangian correlations of small-scale turbulence at low Reynolds number". In: *Journal of Fluid Mechanics* 574, pp. 405–427.

Gurgel, K-W et al. (1999). "Wellen Radar (WERA): a new ground-wave HF-radar for ocean remote sensing". In: *Coastal Engineering* 37.3, pp. 219–234.

Hadjighasem, Alireza, Mohammad Farazmand, and George Haller (2013). "Detecting invariant manifolds, attractors, and generalized KAM tori in aperiodically forced mechanical systems". In: *Nonlinear Dynamics* 73.1, pp. 689–704.

Haller, G. (2002). "Lagrangian coherent structures from approximate velocity data". In: *Physics of Fluids* 14, pp. 1851–1861.

— (2011). "A variational theory of hyperbolic Lagrangian Coherent Structures". In: *Physica D* 240, pp. 574–598. DOI: 10.1016/j.physd.2010.11.010.

Haller, G. and F. J. Beron-Vera (2013). "Coherent Lagrangian vortices: the black holes of turbulence". In: *Journal of Fluid Mechanics* 731.

Haller, G. and G. Yuan (2000). "Lagrangian coherent structures and mixing in two-dimensional turbulence". In: *Physica D: Nonlinear Phenomena* 147.3, pp. 352 – 370. ISSN: 0167-2789.

Haller, George (2001). “Lagrangian structures and the rate of strain in a partition of two-dimensional turbulence”. In: *Physics of Fluids* 13.11, pp. 3365–3385.

— (2015). “Lagrangian Coherent Structures”. In: *Annual Review of Fluid Mechanics* 47, pp. 137–162.

Haller, George and Francisco J. Beron-Vera (2012). “Geodesic theory of transport barriers in two-dimensional flows”. In: *Physica D: Nonlinear Phenomena* 241.20, pp. 1680 –1702. ISSN: 0167-2789. DOI: http://dx.doi.org/10.1016/j.physd.2012.06.012.

Hansen, D.V. and P.M Poulain (1996). “Processing of WOCE/TOGA drifter data”. In: *Journal of Atmospheric and Ocean Technology* 13, pp. 900 –909.

Harlan, Jack et al. (2010). “The integrated ocean observing system high-frequency radar network: status and local, regional, and national applications”. In: *Marine Technology Society Journal* 44.6, pp. 122–132.

Harrison, Cheryl S. and Gary A. Glatzmaier (2012). “Lagrangian coherent structures in the California Current System – sensitivities and limitations”. In: *Geophysical and Astrophysical Fluid Dynamics* 106.1, pp. 22–44.

Hastings, Alan and Louis Gross (2012). *Encyclopedia of theoretical ecology*. 4. Univ of California Press.

Haza, AC et al. (2007). “Model-based directed drifter launches in the Adriatic Sea: results from the DART experiment”. In: *Geophysical Research Letters* 34.10.

Haza, Angelique C et al. (2008). “Relative dispersion from a high-resolution coastal model of the Adriatic Sea”. In: *Ocean Modelling* 22.1, pp. 48–65.

Haza, Angelique C. et al. (2010). “Transport properties in small-scale coastal flows: relative dispersion from VHF radar measurements in the Gulf of La Spezia”. In: *Ocean Dynamics* 60, pp. 861–882.

Hernández-Carrasco, Ismael et al. (2011). “How reliable are finite-size Lyapunov exponents for the assessment of ocean dynamics?” In: *Ocean Modelling* 36.3, pp. 208–218.

Huhn, F. et al. (2012). “Horizontal Lagrangian transport in a tidal-driven estuary. Transport barriers attached to prominent coastal boundaries”. In: *Continental Shelf Research* 39-40, pp. 1–13.

Hussain, A. K. M. F. (1983). “Coherent structures—reality and myth”. In: *The Physics of Fluids* 26.10, pp. 2816–2850. DOI: 10.1063/1.864048.

Ivonin, D.V. et al. (2004). “Validation of HF radar probing of the vertical shear of surface currents by acoustic Doppler current profiler measurements”. In: *Journal of Geophysical Research: Ocean* 109.

Jirka, Gerhard H. (2001a). “Large scale flow structures and mixing processes in shallow flows”. In: *Journal of Hydraulic Research* 39.6, pp. 567–573.

Jirka, Gerhard H and Wim SJ Uijttewaal (2004). “Shallow flows: a definition”. In: *Shallow flows*, pp. 3–11.

Jirka, G.H. (2001b). “Large scale flow structures and mixing processes in shallow flows”. In: *J. Hydr. Res.* 39, pp. 567–573.

Jordi, A. et al. (2006). “Scientific management of Mediterranean coastal zone: A hybrid ocean forecasting system for oil spill and search and rescue operations”. In: *Marine Pollution Bulletin* 53.5–7, pp. 361 –368.

Karrasch, D. and G. Haller (2013). “Do Finite-Size Lyapunov Exponents detect coherent structures?” In: *Chaos* 23.043126, p. 11.

Khatibi, Rahman H, John JR Williams, and Peter R Wormleaton (2000). “Friction parameters for flows in nearly flat tidal channels”. In: *Journal of Hydraulic Engineering* 126.10, pp. 741–749.

Kraichnan, H. (1967). “Inertial ranges of two dimensional turbulence”. In: *Phys. Fluids* 10, pp. 1417–1423.

Kundu, Pijush K., Ira M. Cohen, and David R. Dowling, eds. (2012). *Chapter 13 - Geophysical Fluid Dynamics*. Fifth Edition. Boston: Academic Press, pp. 621 –690.

LaCasce, JH (2000). “Floats and f/H”. In: *Journal of Marine Research* 58.1, pp. 61–95.

LaCasce, J.H. (2008). “Statistics from Lagrangian observations”. In: *Progress in Oceanography* 77, 1Â–29.

LaCasce, JH and Carter Ohlmann (2003). “Relative dispersion at the surface of the Gulf of Mexico”. In: *Journal of Marine Research* 61.3, pp. 285–312.

Lapeyre, Guillaume (2002). “Characterization of finite-time Lyapunov exponents and vectors in two-dimensional turbulence”. In: *Chaos: An Interdisciplinary Journal of Nonlinear Science* 12.3, pp. 688–698.

Lekien, Francois and Chad Coulliette (2007). “Chaotic stirring in quasi-turbulent flows”. In: *Philosophical Transactions of the Royal Society of London A: Mathematical, Physical and Engineering Sciences* 365.1861, pp. 3061–3084.

Lekien, Francois et al. (2005). “Pollution release tied to invariant manifolds: a case study for the coast of Florida”. In: *Physica D: Nonlinear Phenomena* 210.1-2, pp. 1–20. ISSN: 0167-2789. DOI: 10.1016/j.physd.2005.06.023.

Lipa, B.J. and D. Barrick (1983). “Least-squares methods for the extraction of surface currents from CODAR crossed-loop data: application at ARSLOE”. In: *IEEE Journal of Oceanic Engineering* 8, pp. 226–253.

Lipinski, Doug and Kamran Mohseni (2010). “A ridge tracking algorithm and error estimate for efficient computation of Lagrangian coherent structures”. In: *Chaos: An Interdisciplinary Journal of Nonlinear Science* 20.1, p. 017504.

Lorenz, Edward N (1963). “Deterministic nonperiodic flow”. In: *Journal of the atmospheric sciences* 20.2, pp. 130–141.

Malačič, Vlado and B. Petelin (2001). “Regional Studies: Gulf of Trieste”. In: In: Cushman-Roisin, B., Gačič, M., Poulain, P.M., Artegiani, A. (Eds.). Physical Oceanography of the Adriatic Sea. Past, Present and Future. Kluwer Accademic Publishers, Dordrecht, Boston, London, pp. 167–181.

Malačič, Vlado and Boris Petelin (2009). “Climatic circulation in the Gulf of Trieste (Northern Adriatic)”. In: *Journal of Geophysical Research: Oceans (1978–2012)* 114.C7.

Mariano, Arthur et al. (2016). “Statistical properties of the surface velocity field in the northern Gulf of Mexico sampled by GLAD drifters”. In: 121.

Mathur, Manikandan et al. (2007). “Uncovering the Lagrangian Skeleton of Turbulence”. In: *Physical Review Letters* 98.14, p. 144502. DOI: 10.1103/PhysRevLett.98.144502.

Molcard, A. et al. (2009). “Comparison between VHF radar observations and data from drifter clusters in the Gulf of La Spezia”. In: *Journal of Marine Systems* 78.Supplement, S79 –S89.

Nezu, I., K. Onitsuka, and K. Iketani (1999). “Coherent horizontal vortices in compound open channel flows”. In: *Hydraulic Modeling*. Ed. by V. P. Singh, I. W. Seo, and J. H. Sonu. Water Resources Pub., Colorado, USA, pp. 17–32.

Nikora, V. et al. (2007). “Large-scale turbulent structure of uniform shallow free-surface flows”. In: *Environ Fluid Mech.* 7, pp. 159–172.

Ohlmann, Carter et al. (2007). “Interpretation of coastal HF-radar-derived surface currents with high-resolution drifter data”. In: *Journal of Atmospheric and Oceanic Technology* 24.4, pp. 666–680.

Okubo, A. (1970). “Horizontal dispersion of floatable particles in the vicinity of velocity singularities such as convergences”. In: *Depp-Sea Res.* 17, pp. 445–454.

Olascoaga, M. J. et al. (2013). “Drifter motion in the Gulf of Mexico constrained by altimetric Lagrangian coherent structures”. In: *Geophysical Research Letters* 40.23, pp. 6171–6175. ISSN: 1944-8007.

Onu, K, Florian Huhn, and George Haller (2015). “LCS Tool: A computational platform for Lagrangian coherent structures”. In: *Journal of Computational Science* 7, pp. 26–36.

Ottino, J. M. (1989). *The kinematics of mixing: stretching, chaos, and transport*. (Cambridge Texts in Applied Mathematics) Cambridge University Press.

Paduan, Jeffrey D. and Leslie K. Rosenfeld (1996). “Remotely sensed surface currents in Monterey Bay from shore-based HF radar (Coastal Ocean Dynamics Application Radar)”. In: *Journal of Geophysical Research: Oceans* 101.C9, pp. 20669–20686. ISSN: 2156-2202.

Paduan, Jeffrey D and Libe Washburn (2013). “High-frequency radar observations of ocean surface currents”. In: *Annual review of Marine Science* 5, pp. 115–136.

Peacock, T. and G. Haller (2013). “Lagrangian coherent structures: the hidden skeleton of fluid flows”. In: *Physics Today* 66, pp. 41–47.

Peikert, Ronald, David Günther, and Tino Weinkauf (2013). “Comment on “Second derivative ridges are straight lines and the implications for computing Lagrangian Coherent Structures, Physica D 2012.05.006””. In: *Physica D: Nonlinear Phenomena* 242.1, pp. 65 –66. ISSN: 0167-2789.

Peikert, Ronald et al. (2014). “A comparison of Finite-Time and Finite-Size Lyapunov Exponents”. In: *Topological Methods in Data Analysis and Visualization III. Springer*.

Peng, J. and J. O. Dabiri (2009). "Transport of Inertial Particles by Lagrangian Coherent Structures: application to Predator-prey Interaction in Jellyfish Feeding". In: *Journal of Fluid Mechanics* 623.-1, pp. 75–84. DOI: 10.1017/S0022112008005089.

Poje, Andrew C et al. (2010). "Resolution dependent relative dispersion statistics in a hierarchy of ocean models". In: *Ocean Modelling* 31.1, pp. 36–50.

Poulain, P.M. (1999). "Drifter observations of surface circulation in the Adriatic Sea between December 1994 and March 1996". In: *Journal of Marine System* 20, pp. 231 –253.

Poulain, P.M. et al. (2009). "Wind effects on drogued and undrogued drifters in the Eastern Mediterranean". In: *Journal of Atmospheric and Oceanic Technology* 26, pp. 1144 –1156.

Prants, S. V. (2015). "Backward-in-time methods to simulate large-scale transport and mixing in the ocean". In: *Physica Scripta* 90.7, p. 074054.

Prooijen, B.C. van, J.A. Battjes, and W.S.J. Uijttewaal (2005). "Momentum Exchange in Straight Uniform Compound Channel Flow". In: *J. Hydr. Engng* 131.3, pp. 175–183.

Provenzale, A. (1999). "Transport by coherent barotropic vortices". In: *Annual Review of Fluid Mechanics* 31, pp. 55–93.

Rohrs, J. et al. (2015). "Comparison of HF radar measurements with Eulerian and Lagrangian surface currents". In: *Ocean Dynamics* 65, pp. 679–690.

Rotta, J. (1956). "Experimenteller Beitrag zur Entstehung turbulenter Strömung im Rohr". In: *Ingenieur-Archiv* 24.4, pp. 258–281. ISSN: 1432-0681.

Rovenski, Vladimir (2010). *Modeling of Curves and Surfaces with MATLAB*. 1st. Springer Publishing Company, Incorporated. ISBN: 0387712771, 9780387712772.

Rowiński, Paweł and Artur Radecki-Pawlik (2015). *Rivers–Physical, Fluvial and Environmental Processes*. Springer.

Rypina, I. I. et al. (2007). "Robust Transport Barriers Resulting from Strong Kolmogorov-Arnold-Moser Stability". In: *Phys. Rev. Lett.* 98 (10), p. 104102.

Sadlo, Filip and Ronald Peikert (2007). "Efficient visualization of Lagrangian coherent structures by filtered AMR ridge extraction". In: *Visualization and Computer Graphics, IEEE Transactions on* 13.6, pp. 1456–1463.

Samelson, R. M. (1992). "Fluid Exchange across a Meandering Jet". In: *Journal of Physical Oceanography* 22.4, pp. 431–444.

Samelson, RM (2013). "Lagrangian motion, coherent structures, and lines of persistent material strain". In: *Annual review of marine science* 5, pp. 137–163.

Schmidt, R.O. (1986). "Multiple emitter location and signal parameter estimation". In: *IEEE Transactions on Antennas and Propagation* 34, pp. 276–280.

Schroeder, K et al. (2011). "Relative dispersion in the Liguro-Provencal basin: from sub-mesoscale to mesoscale". In: *Deep Sea Research Part I: Oceanographic Research Papers* 58.3, pp. 209–228.

Shadden, S. C., F. Lekien, and J. E. Marsden (2005). "Definition and properties of Lagrangian coherent structures from finite-time Lyapunov exponents in two-dimensional aperiodic flows". In: *Physica D* 212, pp. 271–304.

Shadden, Shawn C. et al. (2009). "The correlation between surface drifters and coherent structures based on high-frequency radar data in Monterey Bay". In: *Deep Sea Research Part II: Topical Studies in Oceanography* 56.3–5, pp. 161–172. ISSN: 0967-0645. DOI: http://dx.doi.org/10.1016/j.dsr2.2008.08.008.

Socolofksy, S.A. and G.H. Jirka (2004). "Large-Scale Flow Structures and stability in shallow flows". In: *J. Environ. Eng.Sci.* 3, pp. 451–462.

Soldini, L. et al. (2004). "Macrovortices-induced horizontal mixing in compound channels". In: *Ocean Dyn.* 54, pp. 333–339.

Stewart, R.H. and J.W. Joy (1974). "HF radio measurements of surface currents". In: *Deep Sea Research* 21, pp. 1039 –1049.

Stocchino, A. and M. Brocchini (2010). "Horizontal mixing of quasi-uniform, straight, compound channel flows". In: *Journal of Fluid Mechanics* 643, pp. 425–435.

Stocchino, A. et al. (2011). "Lagrangian mixing in straight compound channel". In: *Journal of Fluid Mechanics* 675, pp. 168–198. DOI: doi:10.1017/S0022112011000127.

Talke, Stefan A et al. (2013). "Turbulent kinetic energy and coherent structures in a tidal river". In: *Journal of Geophysical Research: Oceans* 118.12, pp. 6965–6981.

Tang, W., C. Pak Wai, and G. Haller (2011). "Lagrangian Coherent Structures Analysis of Terminal Winds Detected by Lidar. Part I: Turbulence Structures". In: *Journal of Applied Meteorology and Climatology* 50, pp. 325–338. DOI: http://dx.doi.org/10.1175/2010JAMC2508.1.

Tang, X.Z. and A.H. Boozer (1996). "Finite time Lyapunov exponent and advection-diffusion equation". In: *Physica D: Nonlinear Phenomena* 95.3, pp. 283 –305.

Taylor, G.I. (1921). "Diffusion by continuous movement". In: *Proc. Lond. Math. Soc.* 20, pp. 196–212.

Thiffeault, Jean-Luc and Allen H. Boozer (2001). "Geometrical constraints on finite-time Lyapunov exponents in two and three dimensions". In: *Chaos* 11.1, pp. 16–28.

Truesdell, C. and W. Noll (2004). *The Non-Linear Field Theories of Mechanics*. Springer.

Ullman, D.S. et al. (2006). "Trajectory prediction using HF radar surface curents: Monte Carlo simulations of prediction uncertainties". In: *Journal of Geophysical Research* 111, pp. 475 –485.

Van Prooijen, BC, R Booij, and WSJ Uijttewaal (2000). "Measurement and analysis methods of large scale horizontal coherent structures in a wide shallow channel". In: *10th International Symposium on Applications of Laser Techniques to Fluid Mechanics, Calouste Gulbenkian Foundation, Lisbon, Portugal*.

Városi, Frank, Thomas M. Antonsen Jr., and Edward Ott (1991). "The spectrum of fractal dimensions of passively convected scalar gradients in chaotic fluid flows". In: *Physics of Fluids A: Fluid Dynamics* 3.5, pp. 1017–1028.

Veneziani, Milena et al. (2004). “Oceanic Turbulence and Stochastic Models from Subsurface Lagrangian Data for the Northwest Atlantic Ocean”. In: *Journal of Physical Oceanography* 34.8, pp. 1884–1906.

Weitbrecht, V., G. Kühn, and G.H. Jirka (2002). “Large scale PIV-measurements at the surface of shallow water flows”. In: *Flow Measurement and Instrumentation* 13.5–6, pp. 237 –245. ISSN: 0955-5986.

Weitbrecht, Volker (2004). “Influence of Dead-Water-Zones on the Dispersive Mass Transport of Rivers”. In:

Wells, MG and GJF van Heijst (2004). “Dipole formation by tidal flow in a channel”. In:

Wilson, Z. D., M. Tutkun, and R. B. Cal (2013). “Identification of Lagrangian coherent structures in a turbulent boundary layer”. In: *Journal of Fluid Mechanics* 728, pp. 396–416. DOI: 10.1017/jfm.2013.214.

Zavala Sansón, L. (2015). “Surface dispersion in the Gulf of California”. In: *Progress in Oceanography* 137.Part A, pp. 24 –37. ISSN: 0079-6611.

Acknowledgements

I have to thank many people. This thesis would not exist without my Supervisor Prof. Giovanni Besio that helped me to solve many problems (in life and in academia) and the help of Dr. Marcello G. Magaldi. Much of the latest results were produced thanks to my Supervisor Prof. Alessandro Stocchino whose good mood helps solving difficult tasks. My life would be meaningless without the love of my Sister, Elisa Martina Enrile, and of my Parents, Camillo and Antonella Lasagni. We cannot always agree but I owe them a lot. I would like to thank all the people that shared nice moments with me during the PhD. They are a lot: Simone Boi, Krystyna Isakova, Francesco Ferrari, Simone Putzu, Gaetano Porcile, Francesco de Leo, Peyman Davvalo Khongar, Davide Medicina, Irene Nepita, Daniele Lagomarsino Oneto, Masha Dvoriashyna whose happiness is contagious, Sonia Angiolani, Mattia Stagnaro, Stefano Olivieri, Andrea Bonfiglio. I would also like to thank the students that I examined (I hope they do not hate me too much) and that I supervised during their thesis. I would like to mention among them Elisa Cozzani and Lorenzo Crocco.